Modelling Dissolution of Precipitate Phases During Homogenization of Aluminum Alloy B319

by

Ida Sadeghi

A thesis

presented to the University of Waterloo

in fulfilment of the

thesis requirement for the degree of

Master of Applied Science

in

Mechanical Engineering

Waterloo, Ontario, Canada, 2016

Author's Declaration

I hereby declare that I am the sole author of this thesis. This is a true copy of the thesis, including any required final revisions, as accepted by my examiners. I understand that my thesis may be made electronically available to the public.

Abstract

Increasing the knowledge about the heat treatment of Aluminum alloys as light metals can be useful since these alloys are used in automotive industry, and optimizing their heat treatment processes can be beneficial economically. Aluminum B319 which is of the type Al-Si-Cu-Mg was used in this study. The result of a theoretical study of diffusion-controlled dissolution of planar, cylindrical, spherical and elliptical θ-Al_2Cu precipitates are presented. Graphical relationships between the precipitate size and dissolution time were developed for a constant diffusion coefficient. The validity of various approximate solutions including: stationary interface, moving boundary using MATLAB and moving boundary using COMSOL software were considered. COMSOL was capable of two-dimensional and three-dimensional modelling. In addition, the dissolution of the Q-$Al_5Mg_8Si_6Cu_2$ precipitate which is a multi-component phase — that involves the diffusion of more than one component during the dissolution process — as well as the concurrent dissolution of θ-Al_2Cu and Q-$Al_5Mg_8Si_6Cu_2$ were modelled using MATLAB. Both two and three-dimensional models were developed using COMSOL. Numerical models were validated through a series of experimental measurements using a fluidized bath furnace. The results show that the model predictions are in good agreement with the experimental results and little variations are due to the simplifications made in the model. The effect of Secondary Dendrite Arm Spacing (SDAS) on dissolution time was also examined and it was shown that the model developed was able to accurately capture these effects as well on the time required for dissolution to of these phases to occur. The model can be used as a tool to identify potential optimisation strategies for industrial solution heat treatment processes.

Key words: Solution heat treatment; Homogenization; Al B319; θ phase; Q phase; Modelling; COMSOL; MATLAB; SDAS.

Acknowledgments

I would like to express my sincere gratitude to Professor Mary A. Wells for her immeasurable supports; whom without her supports, this project could not have been as a memorable learning experience as it has been. I would also like to thank Professor Shahrzad Esmaeili for co-supervising me and always giving me beneficial advice that helped me a great deal throughout the project. I would like to thank my two supervisors for not only being supportive professionally, but also spiritually during these years I have been working with them.

I would also like to thank all the people in the Mechanical and Mechatronics Engineering department who helped me during this project. Specifically, thanks is given to Yuquan Ding, SEM lab advisor, for helping me with scanning electron microscope and for always offering useful advice. I would also like to thank Richard Gordon for being one of the best people in the world who with his thoughtfulness always made the lab a more enjoyable place to be in. I would also like to thank the technicians at the student shop especially Phil Laycock for teaching me how to use the machinery.

Finally, I would like to acknowledge the financial assistance I received from Auto21 and University of Waterloo.

Table of Content

List of Figures

List of Tables

List of Abbreviations

PDAS	Single Component Fixed Mesh
SDAS	Secondary Dendrite Arm Spacing
SEM	Scanning Electron Microscope
SE	Secondary Electron
OM	Optical Microscope
EPMA	Electron Probe Micro Analysis
CF	Conventional Furnace
FB	Fluidized Bath
SCFM	Single Component Fixed Mesh
MCMM	Multi Component Moving Mesh
UDF	User Defined Function
1D	One Dimensional
2D	Two Dimensional
3D	Three Dimensional

List of Symbols

θ	Al_2Cu phase
Q	$Al_5Mg_8Si_6Cu_2$ phase
A	Area [m^2]
J	Diffusion flux [$mol/m^2.s$]
D	Diffusion coefficient [m^2/s]
D_0	Diffusivity factor [m^2/s]
k_i	Partition coefficient
K_{sol}	Solubility product [mol/L]
K_0	Pre-exponential factor for solubility [mol/L]
ΔH	Enthalpy of formation [kJ]
ΔS	Entropy of formation [J/K]
C_I	Solute concentration at the particle-matrix interface [wt%]
C_M	Solute concentration in the matrix [wt%]
C_P	Solute concentration within the particle [wt%]
c_i^{part}	Concentration of diffusing element in the particle[wt%]
c_i^{sol}	Concentration of element i at the particle-matrix interface[wt%]
C_{Alloy}	Concentration of the solute in the alloy[wt%]
C_M^{Cu}, C_M^{Si}, C_M^{Mg}	Concentration of Cu, Si and Mg in the matrix[wt%]
c_{Cu}^{Q}, c_{Si}^{Q}, c_{Mg}^{Q}	Concentration of Cu, Si and Mg within the Q phase[wt%]
r_{df}	Radius of the diffusion field [m]
r_0	Initial radius of the spherical particle [m]
f_v^p	Volume fraction of the particles
f_v^{Alloy}	Volume fraction of the alloy
f_v^{Matrix}	Volume fraction of the matrix

ρ^{Alloy}	Density of the alloy [g/cm^3]
ρ^{Q}	Density of the Q phase [g/cm^3]
ρ^{θ}	Density of the θ phase [g/cm^3]
f	Fraction of solid phase
ΔT	Temperature gradient [K]
λ_{den}	Dendrite arm spacing [m]
S	Segregation ratio

Chapter 1

1. Introduction

Aluminum is the most heavily consumed non-ferrous metal in the world, with current annual consumption at 24 million tons [1]. The demand for improved fuel efficiency in automobiles without impairing performance has led to an increased use of aluminum alloys in the production of a wide variety of castings such as engine blocks, cylinder heads and manifolds (Fig. 1.1). Aluminum casting offers the important advantage of being able to produce lightweight and highly complex functional shapes quickly and easily. Cost is reduced because numerous parts and complex construction and processing steps can be replaced by a single cast part [2].
Aluminum casting alloys such as the type Al-Si-Cu-Mg are hypoeutectic and are normally produced from scrap metal. Al B319 is a type of Al-Si-Cu-Mg alloy with 5.5-6.5 % Si, 3-4 % Cu and <0.5 % Mg. The microstructure expected in a casting made from this alloy will be a mixture of pre-eutectic aluminium dendrites surrounded by Al–Si eutectic, and various types of Cu phase precipitates. The presence of tramp elements from the scrap promotes the formation of various other phases. For example, iron promotes the formation of various intermetallic phases, the most common of which are Al_5FeSi and $Al_{15}(Mn,Fe)_3Si_2$. Mg, added to strengthen aluminium alloys by precipitation of Mg_2Si particles, should be limited to narrow margins in castings hardened by precipitation of Al_2Cu, as in the case of B319, as it tends to form a low melting point eutectic (Al-Si-$Al_5Mg_8Cu_2Si_6$) that solidifies at temperatures below 500°C [3-5].

The mechanical properties of a casting are controlled by its microstructure which, in turn, is influenced by the chemical composition of the alloy, i.e., by its Si, Mg, and Cu content, and by the presence of impurities such as iron, and casting defects (porosity, inclusions, etc.), as well as the solidification history (i.e., cooling rate) and subsequent heat treatment [2]. In the case of A319 alloys, this would imply the α-Al dendrite arm spacing (DAS), the morphology and size of the eutectic Si particles, and the amount of intermetallics and/or other second-phase constituents present in the microstructure; all play a role in final mechanical properties. Cooling rate controls

the fineness of the as-cast microstructure; by increasing the cooling rate, microstructure is characterized by finer eutectic Si particles, finer α-Al dendrites and other phase particles, and smaller dendrite arm spacing, while by increasing the solidification time the formation of a coarse Si particles is predominant [6].

Castings are inhomogeneous due to microsegregation and macrosegregation. Uniform distribution of the solute elements is very important as it plays a vital role in the subsequent thermomechanical processing of the alloy. Heat treatments such as solutionizing, quenching and aging are applied to homogenize microstructure and ameliorate its mechanical properties.

The production of aluminum engine component castings is in many cases a multi-step manufacturing process, where the casting will pass a heat treatment process after its solidification. Figure 1.2 schematically describes the most important manufacturing steps [8].

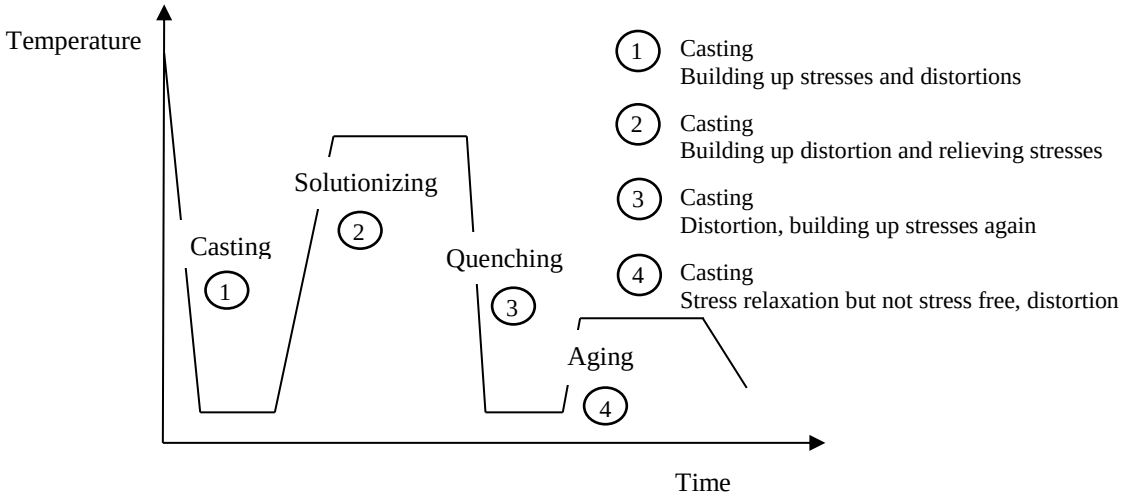

Figure 1.1: Production cycle of aluminum B319.

Chapter 2

2. Background

2.1 Cast AlB319 alloys

Aluminum B319 alloy is of type Al-Si-Cu-Mg alloys. The main phases in the as-cast AlB319 are dendritic α-Al, Al-Si eutectic phase and θ (Al_2Cu) precipitates although Mg, Fe, Mn and other intermetallics are present to some extent [9] (Fig. 2.1). At higher Mg concentrations Q ($Al_5Mg_8Cu_2Si_6$) and β (Mg_2Si) phases also precipitate out (shown in Figure 2.1 – which points). The eutectic Si is in the form of brittle acicular plates that are detrimental to the tensile and impact properties [2]. Iron intermetallic first precipitates as $Al_{15}(FeMn)_3Si_2$ phase that is in the form of skeleton-like or Chinese-script which does not initiate cracks to the same extent as the Al_5FeSi particles which are in the form of long platelets. The Al_5FeSi phase is detrimental to mechanical properties especially ductility, and can also cause shrinkage porosity in castings [10]. Al_2Cu phase precipitates in two distinct forms, i.e., block-like (coarse Al_2Cu precipitates) and eutectic-like (fine Al_2Cu particles interspersed with Al) (Figure 2.2). The proportion of the block-like form increases with decreasing solidification rate, increasing volume fraction of β-Al_5FeSi needles, and modification of the alloy with strontium. The increased number of modified silicon particles serves as nucleation sites for precipitation of very fine individual Al_2Cu particles [11]. Eutectic Al-Al_2Cu-Si forms on Si, β needles, block-like Al_2Cu or as separate pockets within Al matrix [12].

The cooling rate during solidification affects the eutectic silicon size and secondary dendrite arm spacing. Primary and secondary dendrite arm spacings are shown in Figure 2.3. Sand castings solidify at an average solidification rate of lower than 5 °C/s [13].

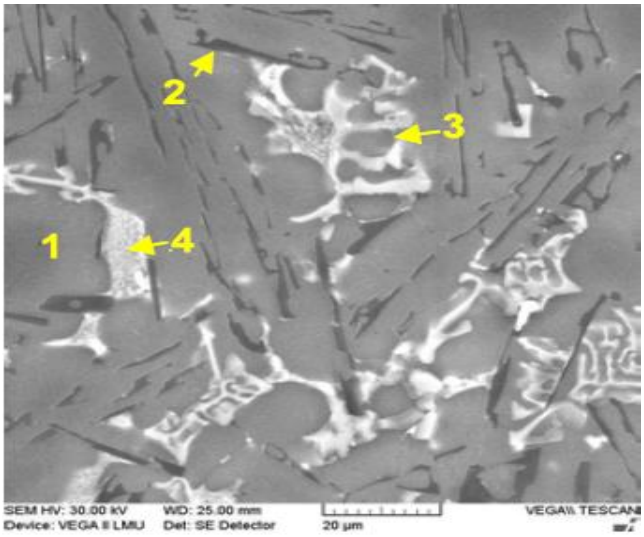

Figure 2.1: A typical as-cast microstructure of Al-Cu-Si-Mg alloys; 1) Aluminum matrix, 2) Si eutectic, 3) Iron intermetallic and 4) Al_2Cu phase [13].

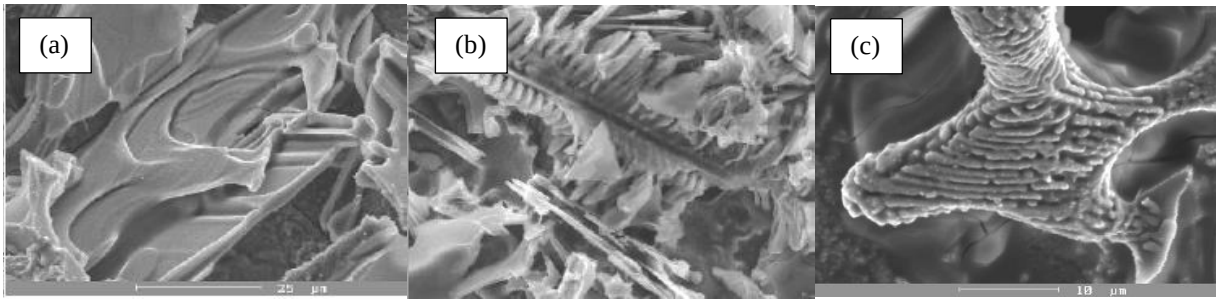

Figure 2.2: Typical phases present in the Al-Si-Cu-Mg alloys; a) Si eutectic and b) skeleton-like $Al_{15}(FeMn)_3Si_2$ phase and c) Al_2Cu eutectic; deep etched in HCl [10].

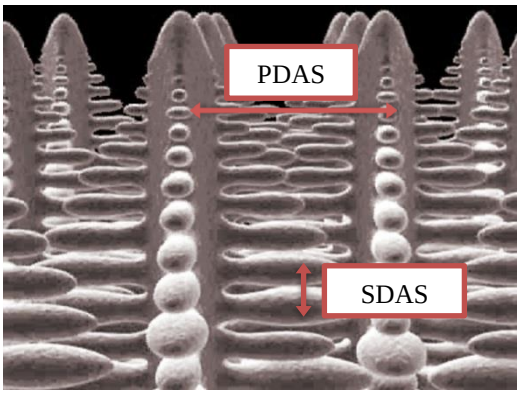

Figure 2.3: General schematic presentation of primary and secondary dendrite arm spacings (PDAS and SDAS) [6].

The solidification sequence in 319.1alloy is reported by Backerud et al. [14] and listed in Table 1.1.

Table 1.1: Reactions occurring during solidification of 319.1 alloy at 0.6 °C/s [14].

Reaction	Suggested Temperature (°C)
1. Development of α-aluminum dendrite network	609
2a. Liquid $\longrightarrow$ Al + $Al_{15}Mn_3Si_2$	590
2b. Liquid $\longrightarrow$ Al + Al_5FeSi + $Al_{15}Mn_3Si_2$	590
3. Liquid $\longrightarrow$ Al + Si + Al_5FeSi	575
4. Liquid $\longrightarrow$ Al + Al_2Cu + Si + Al_5FeSi	525
5. Liquid $\longrightarrow$ Al + Al_2Cu + Si + $Al_5Mg_8Cu_2Si_6$	507

2.2 Heat treatment of AlB319 alloys

Homogenization is a common industrial practice after solidification to obtain the required casting properties. It is a diffusion-controlled process, and its kinetics depends on several factors, such as temperature, diffusion distance (i.e. secondary dendrite arm spacing), diffusivity of the solutes, dissolution rate, and so on. Usually it is carried out on castings to improve the properties of the casting or to facilitate the subsequent steps in the processing to final products [2,15].

Homogenization literally refers to equalization of solute concentration in the single phase (or removing segregation), however, solution heat treatment refers to the process which is mainly related to the secondary phase particle dissolution into the matrix [2,16]. Heat treatment done on AlB319 consists of solution heat treatment, quenching and then aging.

2.2.1 Solution treatment

Solution heat treatment must be applied for a sufficient length of time to obtain a homogeneous supersaturated structure, followed by quenching with the aim of maintaining the

supersaturated structure at ambient temperature. In Al-Si-Cu-Mg alloys, the solution treatment fulfils three roles:

i. Homogenization of the as-cast structure.

ii. Dissolution of certain intermetallic phases such as Al_2Cu and Mg_2Si.

iii. Spheroidization of eutectic silicon [2,17,18].

The segregation of solute elements resulting from dendritic solidification may have an adverse effect on mechanical properties. The time required for homogenization is determined by the solution temperature and by the dendrite arm spacing [19]. Hardening alloying elements such as Cu and Mg display significant solid solubility in heat-treatable aluminum alloys at the solidus temperature; this solubility decreases noticeably as the temperature decreases.

Time and temperature for solutionizing should be optimized. Too long solution treatment at low temperature causes secondary porosity formation during annealing, coarsening of the microstructural constituents and increased processing costs, while too short solutionizing does not lead to a complete dissolution of the alloying elements responsible for subsequent precipitation hardening. From another point, low solution treatment temperature will not homogenize the microstructure, however, high solutionizing temperature can lead to incipient melting and formation of structureless phases when quenching, and storage of high thermal stress in the alloy due to quenching from higher temperature [18,20]. The smaller the SDAS the lower the time needed for solutionizing. Melting of Cu-containing phases starts at lower temperatures as the Mg-content of the alloy increases. Hence, the choice of optimum solution treatment temperature depends on Cu and Mg content of the alloy. The higher the solution treatment temperature, the more accelerated the response of the alloy to aging [21].

During solution heat treatment, soluble intermetallics are dissolved, and the matrix is super-saturated with solute on subsequent quenching. Only those intermetallic phases dissolve that have high solubility at elevated temperature. The primary factor governing the dissolution of intermetallic phases is the relative diffusivity of solutes in the matrix. In addition, other factors that control the dissolution rate of intermetallic phases are interface mobility and a curvature effect. Commercial cast aluminum alloys often contain iron as an impurity [2]. α-Al_5FeSi phases were found to be insoluble, while β-$Al_5(Fe,Mn)Si$ phase dissolved partially in Sr-modified alloys [22-24].The morphology of iron-rich intermetallics plays an important role in the performance of the casting. In general, the sharp edge of iron-rich intermetallic phases may act as a stress

concentrator, which should be avoided. However, despite prolonged solution heat treatment, complete dissolution of iron-rich intermetallics is not possible because of the limited solubility of iron in the aluminum matrix [2].

Al_2Cu phase was observed to dissolve almost completely during solution heat treatment while $Al_5Cu_2Mg_8Si_6$ does not [22,23]. It has been reported that the dissolution mechanism of Al_2Cu phase includes 3 steps: (1) separation of Al_2Cu from β-Al_5FeSi platelets, (2) necking of Al_2Cu phase particles followed by spheroidization, (3) dissolution of the spheroidized Al_2Cu particles by radial diffusion of Cu atoms into the surrounding aluminum matrix [25]. The dissolution of eutectic Al_2Cu occurs through necking, gradual shperoidization of the smaller particles after necking and diffusion of Cu atoms into the surrounding aluminum matrix [26-28], while in the case of block-like Al_2Cu there is no necking, and spheroidization and diffusion take place at a lower rate (Figure 2.4) [26,27].

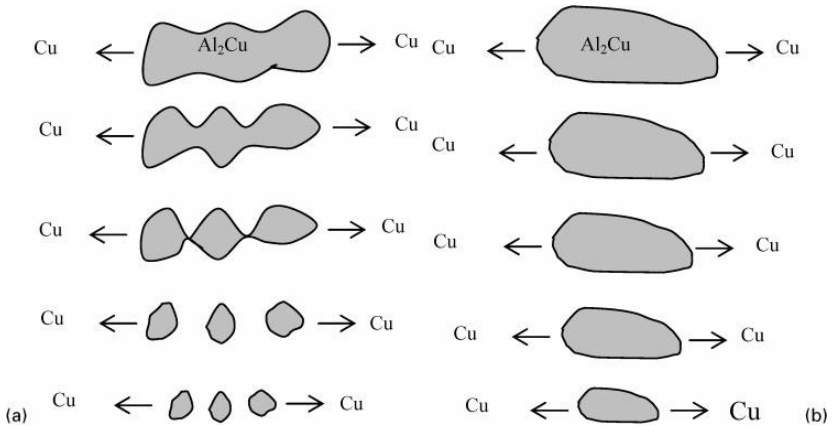

Figure 2.4: A schematic presentation of the dissolution of a) eutectic and b) blocky Al_2Cu [26,27]

Apelian et al. [29] showed that homogenization and dissolution of the Mg_2Si phase in A356 alloy are/is complete after 30-45 minutes of solution heat treatment and prolonged hours are needed to spheroidize the Si particles. The spheroidization rate is much higher in modified alloys, while the coarsening rate is higher in unmodified alloys because of large differences in particle size distribution. Mechanical properties are greatly affected by the Si eutectic shape and

distribution. Si particles are needle shaped but during solution treatment fragment, and become spheroidized [10].

One problem associated with the homogenization process is incipient melting. If the composition of a binary alloy is higher than C_{max} (Figure 2.5) and the alloy in annealed at a temperature higher than T_{eut}, the alloy starts to melt. The melting usually occurs at the grain boundaries where the eutectic is located. In alloys with segregation of the alloying element, the composition may locally exceed the critical composition, C_{max}, even though the mean composition is lower. In this case incipient melting occurs even when T is lower that T_{eut}. [15].

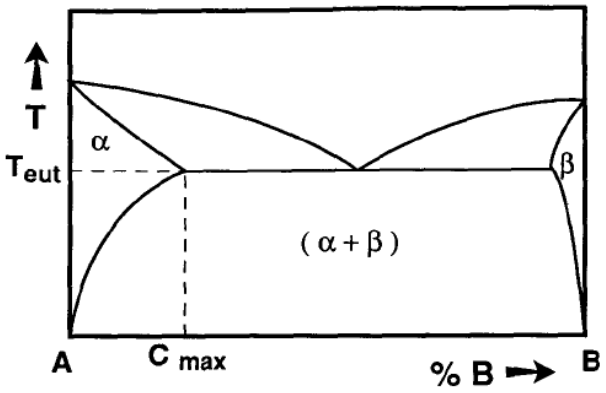

Figure 2.5: A schematic presentation of eutectic binary phase diagram [15].

To overcome the incipient melting in AA319 and at the same time get the utmost benefit of solution heat treatment on homogenizing the microstructure a two stage solution heat treatment with the first stage temperature below the incipient melting temperature (T_{im}) and the second stage temperature above the T_{im} has been suggested. In 2 stage solution treatment, porosity is lower due to better dissolution of Al_2Cu and better homogeneity. In addition to incipient melting, a high solution treatment temperature causes macrocracking and buckling (shape deformation) because of the severity of incipient melting of Al_2Cu. It has been shown that a two stage solution treatment of 495°C/2h followed by 515°C/4h is superior to one stage treatment of 495°C/8h [12]. Skowloski et al. [12] showed that a two stage solution heat treatment with the first stage temperature above incipient melting temperature (T_{im}) and the second stage

temperature below T_{im} has better effect over a conventional solution treatment or a two stage solution treatment with the first stage temperature below the T_{im} and the second stage temperature above the $T_{im.}$ They suggested a treatment of 4 hours at 520°C followed by 1 hour at 490 °C as the best cycle for Al-Si-Cu-Mg alloys. In addition, they assert that even a cycle of 1 hour at 520 °C followed by 1 hour at 490°C will produce better result than a cycle of 5 hours at 485 °C, but in a nearly half of the time. Normally an increase in SDAS will cause a decrease in mechanical properties, however, this 2-stage treatment helps alloy have better mechanical properties even in larger SDAS.

Solution heat treatment using conventional furnaces (CF) entails long soaking times. Fluidized beds (FB) reduce the time needed for solution treatment due to rapid heating rate, which affects the diffusion rate, and control of the temperature. Also, high heating rate activates the precipitation rate of the hardening phases, so precipitates form in less time and obtain a smaller size during aging. Due to the presence of low melting point Al_2Cu in B319, fluctuations in temperature should be controlled. This can be achieved using FB technique. The high heating rate in fluidized beds promotes the fragmentation and spheroidization kinetics of eutectic Si particles through the generation of high thermal stresses owing to the thermal mismatch between the eutectic Si and the Al matrix. This thermal mismatch occurs as a result of the thermal expansion coefficient of Si being much lower than that of Al. A longer solution heat-treatment time leads to a coarsening of the Si particles where the driving forces for the coarsening of eutectic Si during solution heat treatment have been related to the reduction of strain energy and surface energy of the Si particles [30-32].

Another benefit of high heating rate is being able to capture as many dislocations as possible preventing the annihilation of dislocations through recovery. The dislocation concentration in the matrix affects the aging kinetics; the slow heating rate in a conventional furnace annihilates the dislocations through recovery, thereby reducing their density prior to reaching the aging temperature. The dislocations are known to be potential sites for Al_2Cu precipitates which lead to a pronounced improvement in mechanical performance through artificial aging procedures [21].

Han et al. [28] have shown that the $Al_5Mg_8Cu_2Si_6$ phase is insoluble in the matrix due to its complicated nature. This phase precipitates at 491.3 °C which is 10 °C below the precipitation temperature of Al_2Cu, 501.4 °C. This phase precipitates before (pre-eutectic) and after (post-

eutectic) Al_2Cu phase. Hence, solutionizing at temperature close to eutectic temperature of Al_2Cu will cause melting of $Al_5Mg_8Cu_2Si_6$ which in turn leads to the porosity formation; in terms of mechanical properties there should be a balance between Al_2Cu dissolution and porosity formation. Wang et. al. [33] have shown that the maximum solution treatment temperature to avoid from melting in Al-Si-Cu-Mg cast alloys with over 2% Cu is 505 °C; however, by gradual solution treatment this temperature can reach to 525 °C. Gauthier et al. [34,35] have reported that a solution heat treatment process consisting of a stage at 540 °C followed by slow cooling to let the molten (undissolved) Al_2Cu solidifies in the usual manner, followed by quenching into water, produces better mechanical properties in Al-Si-Cu-Mg (0.1%Mg) alloys. They found the optimum solution treatment process to be 8 h at 515 °C. Sokolowski et al. [10] suggested a two-step solutionizing process consisting of 2-4 h at 495 °C followed by 4 h at 515 °C to be the optimum solution treatment. Sablonniere et. al. [36,37] recommended a single-step solution treatment at 510 °C for 12-24 hours which should be followed by 2-5 h aging at 158 °C.

2.2.2 Quenching

Following solution heat treatment, quenching is the next important step in the heat treatment cycle. The objectives of quenching are to suppress precipitation during quenching; to retain the maximum amount of the precipitation hardening elements in solution to form a supersaturated solid solution at low temperatures; and to trap as many vacancies as possible within the atomic lattice.

The quench rate is critical in most Al-Si casting alloys where precipitates form rapidly due to high level of supersaturation and high diffusion rate. At higher quench temperatures the supersaturation is too low and at lower temperatures the diffusion rate is too low for precipitation to be critical. An optimum rate of quenching is necessary to maximize retained vacancy concentration and minimize part distortion after quenching. A slow rate of quenching would reduce residual stresses and distortion in the components, however, it causes detrimental effects such as precipitation during quenching, localized over-aging, reduction in grain boundaries, increase tendencies for corrosion and result in a reduced response to aging treatment. Faster rates of quenching retain a higher vacancy concentration enabling higher mobility of the elements in the primary Al phase during aging and thus can reduce the aging time significantly, however, it leads to higher residual stress and distortion in the part.

The effectiveness of the quench is dependent upon the quench media (which controls the quench rate) and the quench interval. The media used for quenching aluminum alloys include water, brine solution and polymer solution. Water used to be the dominant quenchant for aluminum alloys, but water quenching most often causes distortion, cracking, and residual stress problems. Air blast quenching or water mist sprays may be used if the objective is to reduce quench distortion and cost, provided that the lower mechanical properties that result are acceptable for the application in question. The quench media should have sufficient volume and heat extracting capacity to produce rapid cooling. Thick sections which require a high quench rate are normally quenched in water whose temperature is between 25 to 100 C. The quench rate can be reduced in thin sections (which are more prone to distortion) by quenching in oil or commercially available polymer-based compounds. The selection of quench medium is often determined by several factors, such as application, quench sensitivity of the alloy, residual stress, structural integrity, and so on. Among them, quench sensitivity of the alloy is the most important factor. Quench sensitivity is generally high in alloys containing higher solute levels and containing dispersoids that act as nucleation sites for coarse precipitates [2].

2.2.3 Aging

Age-hardening has been recognized as one of the most important methods for strengthening aluminum alloys, which results in the breakdown of the supersaturated matrix to nanosized particles capable of being sheared by dislocations [2,34]. By controlling the aging time and temperature, a wide variety of mechanical properties may be obtained; tensile strengths can be increased, residual stresses can be reduced, and the microstructure can be stabilized. The precipitation process can occur at room temperature or may be accelerated by artificial aging at temperatures ranging from 90 to 260°C. After solution treatment and quenching the matrix has a high supersaturation of solute atoms and vacancies. Clusters of atoms form rapidly from the supersaturated matrix and evolve into Guinier–Preston (GP) zones. Metastable coherent or semi-coherent precipitates form either from the GP zones or from the supersaturated matrix when the GP zones have dissolved. The precipitates grow by diffusion of atoms from the supersaturated solid solution to the precipitates [2].

The T_6 heat treatment is illustrated in Figure 2.6 for an Al-Si-Cu alloy as an example. The evolution of the microstructure is shown; from (1) atoms in solid solution at the solution

treatment temperature, through (2) a supersaturated solid solution at room temperature after quench, to (3) precipitates formed at the artificial aging temperature [2].

The precipitation sequence for an Al-Si-Cu alloy, such as 319, is based upon the formation of Al_2Cu-based precipitates. The Al_2Cu precipitation sequence is generally described as follows: [18,38]

$$\alpha_{ss} \rightarrow \quad GP\ Zones \quad \rightarrow \quad \theta'' \quad \rightarrow \quad \theta' \quad \rightarrow \quad \theta\ (Al_2Cu)$$

In Al-Si-Cu-Mg at high Mg levels (more than 6% [5]) Q and β phases may also form. Cu can increase the fraction of the β″ phase formed, but it can also form the Q″ phase, which has a lower strength contribution compared to the β″ phase. The β″ phase is therefore preferred, rather than the Q″ phase [5,8,39]

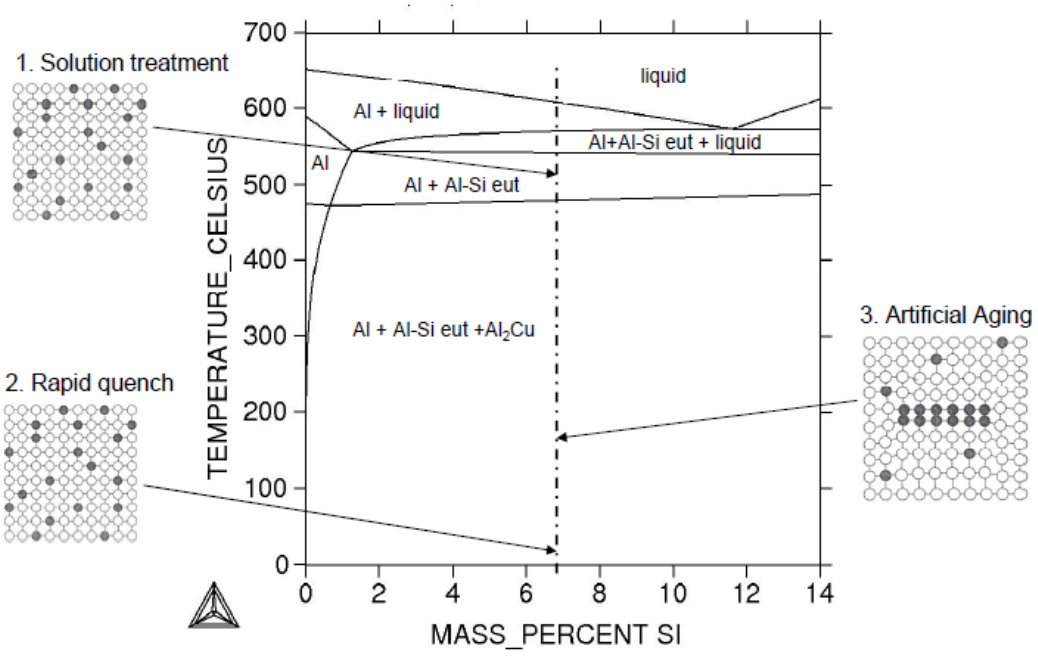

Figure 2.6: T_6 heat treatment of Al-Si-Cu alloys [5].

The time and temperature of aging treatment determines the number density, size, and size distribution of precipitates [2]. Fine and dense precipitates with a smaller inter-particle

spacing are formed at a lower aging temperature of 150 °C compared to coarse, less dense and more widely dispersed at higher temperature, i.e., 250 °C. The strength of 319 alloys increases with the Mg content and decreases with Sr and aging temperature and time [40]. It is been reported that the precipitates that predominate at the peak aging of cast A319 aluminum alloy (Al–4.93 wt%Si–3.47 wt%Cu) after solution treatment at 500 ± 5 °C for 8 h and aging at 170 ± 5 °C for 24 h are coherent θ″ together with semi-coherent θ′ at lower number density. It is been suggested that θ″ is mainly responsible for peak aging in cast A319 aluminum alloy [41,42].

Dislocation density affects aging response. These dislocations form during quenching. θ′ phase forms on dislocation while θ″ forms somewhere in the bulk [43]. The more the dislocation density, the higher the fraction of θ′; so the strength of the alloy is lower. The strength of an age-hardenable alloy is governed by the interaction of moving dislocations and precipitates. The obstacles in precipitation hardened alloys which hinder the motion of dislocations may be either the strain field around the GP zones resulting from their coherency with the matrix, or the zones and precipitates themselves, or both. The dislocations are then forced to cut through them or go around them forming loops.

When the alloy is naturally aged prior to artificially aging, age hardening response would be slower, but the time to peak and the peak hardness will remain unaffected.A pre-step aging at lower temperature after solution treatment and then aging at the regular temperature, results in improved mechanical properties because pre-aging causes finer dispersion of precipitates. This is due to the fact that higher density of precipitates leads to the lower inter-precipitates spacing in which dislocations bow. However, the single step still has remained the most economical temper in terms of hardness [44].

2.3 Modelling dissolution during homogenization

Modelling can facilitate the design of an alloy and its heat treatment process, which meets specified requirements for a certain component. Development of models can also help in the search for new alloys as knowledge is gained about the influence of the microstructure on the alloy properties.

Two processes are involved in the dissolution of a precipitate: 1) atom transfer across the interface separating the matrix and the precipitate phase (interface diffusion) and 2) diffusion of the solutes away from the interface (long range diffusion) [45]. There are two limiting cases; 1)

the dissolution rate is limited by long range solute diffusion through the matrix and 2) the transfer of atoms across the matrix-precipitate interface controls the dissolution rate. In the former case local interfacial equilibrium exists while in the latter it does not, and the rate of dissolution is controlled by and interfacial reaction.

The time needed for the dissolution of secondary phases and homogenization of the as-cast microstructure during a post casting heat treatment can be modelled using various approaches. Dissolution of second phase particles was first modelled by Aaron [46]. He assumed that the dissolving particle is in equilibrium with the matrix and as the particle dissolves the re-equilibrium at the particle-matrix interface to the new equilibrium concentration occurs rapidly in comparison to other processes involved in the dissolution.

$$\frac{dR(t)}{dt} = \frac{K^2 D}{2[R(t) - R_0]} \qquad (2.1)$$

In the above equation $R(t)$ is the precipitate radius or half-thickness as a function of time (t) during dissolution, K is a material constant, D is the volume interdiffusion coefficient andR_0 is the radius or half thickness of the initial particle. In the model developed by Aaron just the steady state part is taken into account.

After Aaron, Whelan [47] considered both the steady state and transient parts of the dissolution kinetics. He considered the precipitate-matrix interface to be stationary and found the dissolution rate of a spherical particle as follows:

$$\frac{dR}{dt} = -\frac{kD}{2R} - \frac{k}{2}\sqrt{\frac{D}{\pi t}} \qquad (2.2)$$

Where $k = 2(C_I - C_M)/(C_P - C_I)$, R is the radius of the precipitate and D is the diffusion coefficient. The term in R^{-1} on the right of equation (2-2) arises from the steady state part of the diffusion field. The term $t^{-1/2}$ arises from the transient part.

In most alloy systems of interest, $|k| < 0.3$, and it has been shown that for small values of k, the stationary interface is a good assumption. It is noteworthy to say that for small values of k it is concentration inequality $C_P - C_M \gg C_I - C_M$ rather than slow interface reaction that guarantees R(t) to be slowly varying as a function of time [48]. A small value of k means that the

concentration of the alloying elements in the particle is so large compared to the solubility of them in the matrix that atoms can diffuse away from the particle without causing a rapid movement of the particle/matrix interface [49].

When the transient part is zero such as over long times for the range of $r < \sim 2000\dot{A}$ and small rate constant (k), Thomas and Whelan have shown that the dissolution rate can be found according to equation (2-3) [46,50].

$$\frac{d(r^2)}{dt} = -kD \qquad (2.3)$$

Nolfi et al. [51] broadened the model developed by Whelan. They considered the effect of interfacial reactions as well and defined a parameter named σ which specifies the thermodynamic state of the interface:

$$\sigma = \left(\frac{KR_0}{D} + 1\right)^{-1} \qquad (2.4)$$

Where K is the reaction rate constant, D is the diffusivity of solutes in matrix and R_0 is the precipitated radius. If K is infinite then local equilibrium prevails; if K deviates infinitesimally from zero, then interfacial reactions are rate controlling. For intermediate values of K, mixed mode occurs.

Aaron and Kotler in 1971 [48] introduced the effect of particle surface curvature according to the well-known Gibbs-Thompson effect and figured out that the influence of curvature is negligible unless the difference between the solute concentration at the particle-matrix interface and the matrix concentration is sufficiently small. In this case, the presence of curvature tends to speed up dissolution, being particularly important at long times (i.e. small precipitate sizes).

Brown in 1976 [52] considered the effect of morphology on the dissolution kinetics. He considered spherical, cylindrical and planar shapes. The dissolution time for cylindrical particle lies in between of spherical and planar but closer to the spherical shape. He also showed that there is a progressive decrease in the dissolution time with increasing saturation which is due to the fact that the concentration gradient at the phase interface increases with increasing saturation (Figure 2.7).

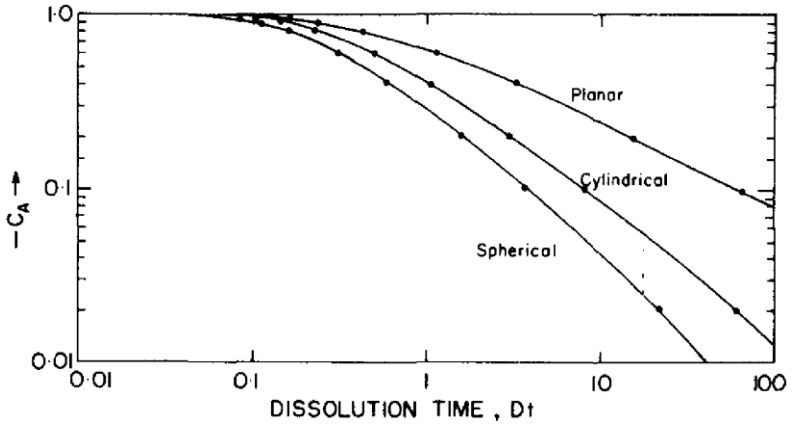

Figure 2.7: Dissolution times for planar, spherical and cylindrical precipitates as a function of saturation, C_A [52].

Tundal and Ryum in 1992 [49] introduced the idea of having a size distribution in particles instead of having an array of particles with equal size. It was found that small particles decrease in size at higher rate than large particles which makes the presence of a size distribution in particles to greatly influence the dissolution kinetics.

Singh and Flemings [38] considered a plate-like dendrite morphology, having an initial sinusoidal composition distribution in the primary phase and constant second phase composition. According to their model the expression which relates volume fraction of the second phase to solution time is:

$$\frac{g+a}{g_0+a} = \exp\left(-\frac{Dt}{l_0^2}.\frac{\pi^2}{4}\right) \qquad (2.5)$$

Where g and g_0 are the volume fraction of the second phase at time t and t=0, respectively, D is the diffusion coefficient at the solution temperature, l_0 is one half secondary dendrite arm spacing, t is the time of solution treatment, $a = \frac{C_M - C_0}{C_\beta}$, C_M is the maximum solubility at solution temperature, C_0 is the initial composition and C_β is composition of β phase.

The critical time for complete solutionizing, t_c, is obtained by setting $g = 0$

$$t_c = \frac{4l_0^2}{\pi^2 D}\ln\frac{g_0+a}{a} \qquad (2.6)$$

Teleshov and Zolotorevsky [53] also derived an approximate expression for the time required for total dissolution of the second phase. Composition of the second phase was assumed constant and interface motion was neglected. This analysis is a solution to Fick's first law using a mean concentration gradient, $\Delta C/\Delta X$, where the effective diffusion distance, ΔX, is estimated from the particle/matrix interface area, S, and the dendrite arm spacing, d. Assuming a plate-like morphology ($S = 1/l_0$), the time to dissolve the precipitates may be written as:

$$t_c = \frac{g_0[C_\beta - C_M]}{\left[(C_M - C_0) + \frac{g_0}{2}(C_\beta + C_M)\right]}\left(\frac{l_0^2}{D}\right) \qquad (2.7)$$

Rometsch [54] modelled the dissolution of binary second phase particle during solution heat treatment. He considered equally sized spherical diffusion field around equally sized particle, considering there are no other particles other than dissolving particles and that the particle-matrix interface is not moving as particles dissolve. Based on these microstructural simplifications, he developed a numerical finite difference model whose output is dissolution and homogenization time. This model solves Fick's first law in radial coordinates. He validated the model for aluminum A356 and A357. The results are shown in Table 2.1.

Table 2.1: Model predictions for A356 and A357 [54].

Alloy and condition	Numerical model	Experimental result
A356 Dissolution time	3 min	2-4 min
A356 Homogenization time	5.1 min	8-15 min
A357 Dissolution time	38.7 min	<50 min
A357 Homogenization time	40.7 min	<50 min

Vermolen [55-71] developed a model for multicomponent systems. He used the multi-component version of Fick's second law (Equation 2.8) and for simplicity assumed that all species diffuse independently, and that the diffusion coefficients are constant.

$$\frac{\partial c_i}{\partial t} = \frac{D_i}{r^a}\frac{\partial}{\partial}\left(r^a \frac{\partial c_i}{\partial r}\right) \qquad (2.8)$$

Here $D_i$and c_i, respectively, denote the diffusion coefficient and the concentration of the species i, and a is a geometric parameter, which equals 0, 1, or 2 for a planar, a cylindrical, or a spherical geometry, respectively. As all cross-diffusion coefficients are set to zero, this is a good approximation for most (dilute) commercial alloys. The dissolution rate (interfacial velocity) is obtained as follows:

$$\frac{dS(t)}{dt} = \frac{D_i}{c_i^{part} - c_i^{sol}}\frac{\partial c_i}{\partial S}(S,t) \qquad (2.9)$$

Where c_i^{part} is the weight percent of diffusing element i in the particle, c_i^{sol} is the concentration of element i at the particle-matrix interface and dS/dt the velocity of boundary movement. He found good agreement between the model and the analytical solution at shorter dissolution time, while analytical results deviate from numerical results at longer times (Figure 2-8).

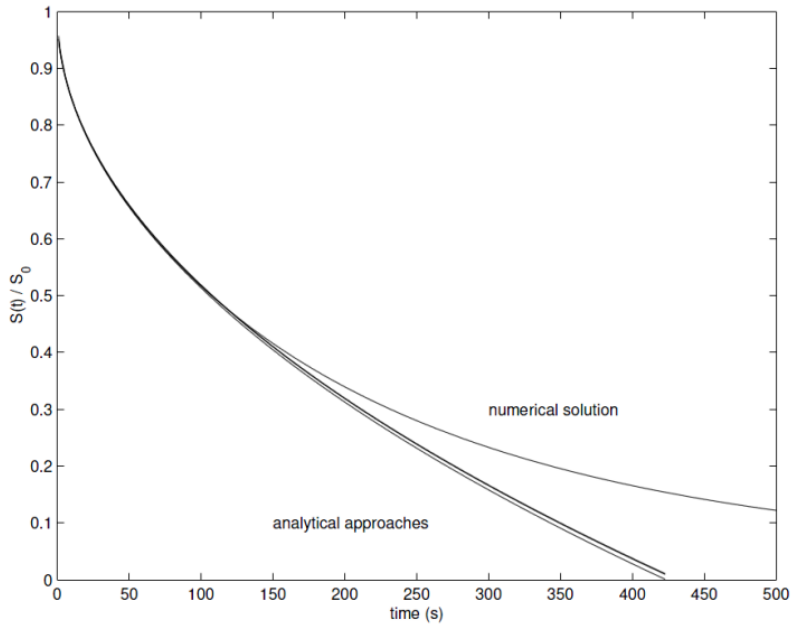

Figure 2.8: The interface position as a function of time during the dissolution of a planar phase obtained for analytical and numerical solutions [60].

Sjölander [72] modelled the dissolution of Al_2Cu phase in Al-Mg-Si-Cu alloys using Fick's second law. She found out that the dissolution process is diffusion-controlled [73].

Although there are various models for particle dissolution, most of them are applicable for wrought alloys, and there has been less attention on cast alloys in literature. Cast alloys are more complicated in terms of modelling as particle dissolution is accompanied by removal of micro and macro segregation which adds difficulties in the model approximation. Homogenization of cast AlB319 is complex due to concurrent dissolution of θ and Q phase. This study captures the effect of segregation as well as secondary dendrite arm spacing on the particle dissolution and further homogenization, and concurrent dissolution.

Chapter 3

3. Scope and objectives

The thermal processing of high-volume cast-aluminum engine blocks and cylinder head components is a key concern of automotive engineers today. Heat treatment is an indispensable step in manufacturing engine blocks, as mechanical properties are selectively controlled by deliberate manipulation of the chemical and metallurgical structure of a component. However, apart from the desired effects, the heat treatment process can be accompanied by unwanted effects such as component distortion, high material's hardness, low material's strength and a lack of toughness, which can lead to crack formation and fatigue failure. Therefore, success or failure of heat treatment not only affects manufacturing costs but also determines product quality and reliability. Hence, optimization of the heat treatment process is of great significance in the industry due to the ever increasing energy costs and competition. Heat treatment must therefore be taken into account during development and design, and it has to be controlled in the manufacturing process. Part designers are looking for process feasibility, a specific microstructure fitting to the in-service requirements, minimum part distortion, and proper distribution of residual stresses. In simulation-based design and manufacturing it is desirable to calculate the effects of heat treatment in advance and to optimize them by varying materials and workpiece shape.

Cast Al-Si-Cu-Mg alloys are well studied in terms of the influence of different alloying elements and modifiers on their microstructure and mechanical properties. Also, the solution heat treatment and aging process that is done on these types of alloys is well investigated, and the optimum solution heat treatment has been suggested. In addition, microstructural investigation has been done on these alloys and the type of intermetallics and secondary phases that form are

well understood across the entire manufacturing process from casting through to age hardening and final mechanical properties. However, modelling the homogenization process is the main knowledge gap in this area that has remained relatively unstudied. There has been extensive work done on modelling solution heat treatment of wrought aluminum alloys, while cast aluminum alloys have less been studied. Althuogh Colley [74] devleoped a model for A356 to examine the metallurgical changes during homogenization and subsequent aging, the alloy he examined was by comparison much simpler as it only invovled the dissolution of Mg_2Si. The B319 alloy is much more complex and its homogenization involves the concurrent dissolution of the Al_2Cu and Q phases in addition to the Mg_2Si.The benefit of developing models to predict homogenization includes an improvement in our understanding of alloy behaviour during multi-stage heat treatment, which in turn can enable process optimisation from the standpoint of the material and result in lower variability in final component properties. This is particularly important when casting large components with complex solidification patterns and non-uniform as-cast microstructures that respond to solution treatment locally at different rates.

The aim of this work was to model the homogenization process of cast AlB319; this includes dissolution of the secondary phases that are Al_2Cu and Q, as well as the removal of segregation. The effect of SDAS and homogenization temperature as well as the effect of two-step heat treatment is investigated. The final model is then used so that a quantitative understanding of the influence of the process parameters during casting and heat treatment of Al B319 can be obtained.

Chapter 4

4. Modelling and Experimental Methods

In this study, the homogenization process applied to aluminum alloy B319 that consists of the dissolution of secondary phases and the removal of segregation was modelled.

The metallurgical changes that occur during heat treatment of AlB319 were modelled using MATLAB and COMSOL. MATLAB is a commercial software package that provides users with an interactive development environment, so that you can use a high-level language as well as built-in features to perform numerical computation, algorithm development, and application development. COMSOL Multiphysics software, on the other hand, allows users to customize and combine any number of physics, the way they want to.

To model the dissolution phenomena two approaches were applied; stationary interface and moving boundary. In the former approach it is assumed that the particle-matrix interface is stationary. In the latter it is assumed that by gradual dissolution of particle the boundary between particle and matrix moves to accommodate for the particle diameter reduction.

Dissolution of the θ phase was modelled using MATLAB with a finite difference method and COMSOL which uses a finite element method. Dissolution of the Q phase was modelled using MATLAB. Also, the coupling effect of the θ and Q phases in dissolution time was investigated using MATLAB.

Using the models, the effect of particle morphology (shape) and SDAS on the dissolution time was examined. In the present study the geometries that are considered for the dissolving particles are sphere, cylinder, plate and ellipse. Both two and three-dimensional models were developed using COMSOL software. After the dissolution process was complete, the time

needed for complete removal of segregation was modelled to address the whole homogenization process.

Finally, the models were validated through a series of experimental measurements using conventional and fluidized sand bed furnaces for single-step and two-step heat treatment. Qualitative analysis was done using Scanning electron microscope (SEM). Optical microscope (OM) with image analysis software was utilized for quantitative analysis.

4.1 Model development

Particle dissolution is assumed to proceed by a number of subsequent steps: decomposition of the chemical bonds in the particle, crossing of the interface by atoms from the particle and long-distance diffusion in the matrix (Figure 4.1). It is assumed in the model that the first two steps proceed sufficiently fast with respect to the long-distance diffusion that they do not affect the dissolution kinetics.

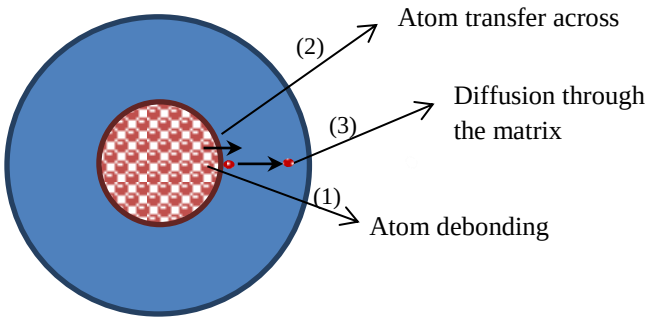

Figure 4.1: A schematic presentation of the steps involved in the particle dissolution process.

4.1.1 Model assumptions

To simplify the model some assumptions should be made; these are as follows,

1) Particles are distributed evenly in the matrix, and have equal sizes and uniform compositions.
2) Particles maintain their stoichiometric composition during the whole process of dissolution.

3) The rate of dissolution is limited by the long-range diffusion; hence, equilibrium is always established at the interface between the particle and the matrix, and the concentration of each element at the interface is equal to the solubility of that element at the solutionizing temperature.
4) The diffusion coefficient, D, is independent of composition and the presence of the other alloying elements. Hence, all cross-diffusion coefficients are set to zero. This is expected to be a good assumption for dilute systems.
5) Soft impingement does not occur. Diffusion fields of particles do not interact. This implies a dilute concentration of solute.
6) Diffusion only takes place inside the Al-rich phase. Precipitate phases are diffusion-free.
7) The model does not differentiate between blocky and eutectic Al_2Cu phase.
8) The effect of convection has been neglected.

4.1.2 Description of the Models

Generally, for modelling the particle dissolution in a field based on diffusion, some aspects are considered:

1- Selection of diffusion equation: 1- Fick's First Law, 2- Fick's Second Law.
2- Solution of equations: 1- finite difference, 2- finite element.
3- Solution of differential equations sets: 1- Explicit, 2- Implicit.
4- Meshing: 1- equal sizes, 2- different sizes by getting distance from the centre of the diffusion field.
5- Movement of mesh: 1- Fixed Mesh 2- Moving Mesh.
6- Reduction of particle mass: 1- system mass conservation, 2- local mass conservation at the interface and checking system mass conservation.
7- Number of components: 1- single component, 2- multi component.
8- Number of Phases: 1- single phase, 2- two or more phases.
9- Number of geometry dimension: 1- one, 2- two, 3- three.
10- Geometry coordination: 1-spherical, 2- cylindrical, 3- cartesian.

In this study three different approaches were selected such that all of these aspects are considered.

1- Single Component Fixed Mesh (SCFM): In this method, Fick's first Law for a single component system is solved explicitly based on the finite difference method. In this approach the mass of particle is reduced based on system mass conservation but the radius of particle is remained fixed (Fixed Mesh). The time step is selected automatically based on convergency criteria. This method is used only for spherical one dimensional system.
2- Multi Component Moving Mesh (MCMM): In this method, Fick's second Law for a single or multi component system is solved implicitly based on finite difference method. The mass of particle is reduced based on local mass conservation at the interface, and the particle radius reduces based on moving mesh. This method is used only for one dimensional spherical, cylindrical and planer systems but it can be used for two phases that are coupled via fields variables.
3- COMSOL: COMSOL is a 3D finite element software which is used for multiphysics modelling. In this study, two physic sections of the code were used: 1- Transport of dilute species 2- Deformed geometry. The major advantage of this code is the capability of simulation of complicated 3D geometries. However, this code cannot be used for multicomponent systems directly. Therefore, the equation of the local mass conservation at the interface must be solved separately with a User Defined Function (UDF). Moreover, the system mass conservation is not conserved when local mass conservation at the interface is used. Furthermore, moving mesh in complicated geometries causes mesh distortion at the interface. Hence, two methods for particle dissolution were proposed: 1- moving mesh based on system mass conservation for simple geometries, and 2- fixed mesh for complicated geometries, while the average concentration of the field is the major parameter for determination of the particle mass.

4.1.3 Fixed mesh approach

A schematic of this approach for a spherical particle is shown in Figure 4.2. It can be seen that the particle is dissolving the particle-matrix interface which is shown by red line is being kept at its initial position.

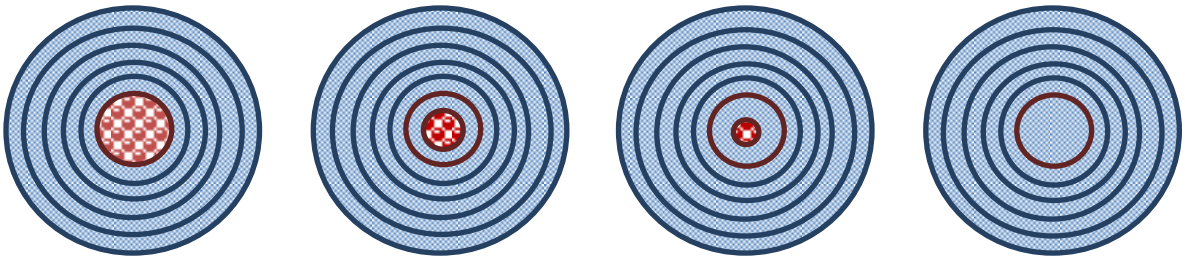

Figure 4.2: A schematic presentation of stationary interface dissolution process for a spherical particle.

4.1.3.1 Governing equations

As-cast aluminum B319 has a dendritic microstructure. The intermetallic phases such as iron or Cu precipitates (Al_2Cu and $Al_5Mg_8Cu_2Si_6$) form at interdendritic spaces when cooling from solidification temperature. Hence, one can relate interparticle spacing to secondary dendrite arm spacing (SDAS). It is assumed that the particles are equally sized and surrounded by the diffusion field in the matrix. In order to derive the relationship between SDAS and the size of diffusion field, microstructure is divided into equally sized cubic cells as diffusion fields with the particles at the centre. The size of these cubic cells is equal to SDAS.

In the case of spherical particles, we can use spherical diffusion field which its radius, r_{df}, can be found by equalizing the volume of the cubic cell to the spherical equivalent one (Figure 4.3),

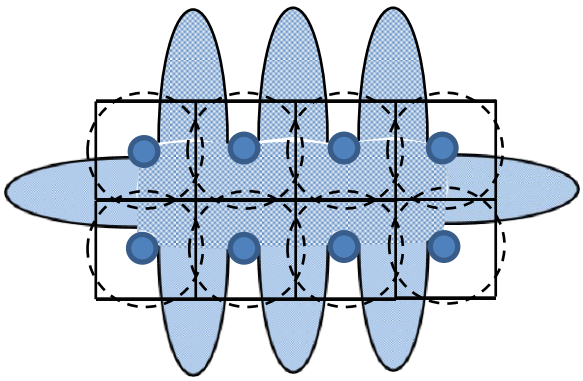

Figure 4.3: A schematic of secondary phase particles location and the diffusion field around the particle.

$$r_{df} = \sqrt[3]{\frac{3SDAS^3}{4\pi}} \qquad (4.1)$$

According to Romesch [54], if volume fraction of a particle is denoted by f_v^P the particle radius, r_p, can be estimated as follow,

$$r_p = \sqrt[3]{\frac{3f_v^P SDAS^3}{4\pi}} \qquad (4.2)$$

There are alloying elements such as Cu and Mg, and impurities such as iron (Fe) in the alloy. Dissolution of the Al_2Cu phase is controlled by the diffusion of Cu into the matrix, while diffusion of Cu, Mg and Si are rate controlling in the dissolution of $Al_5Mg_8Cu_2Si_6$. The initial average matrix concentration of each element, C_M, can be determined from the alloy concentration of that element, C_A, and the volume fraction of the precipitate in the as-cast microstructure as follows,

$$Matrix\ concentration\ = Alloy\ concentration - Particle\ concentration$$

$$C_{Matrix}\rho^{Matrix} f_v^{Matrix} = C_{Alloy}\rho^{Alloy} f_v^{Alloy} - C_\theta \rho^\theta f_v^\theta \qquad (4.3)$$

For Al_2Cu:

Since $f_v^{Alloy} = 1$ and $C_\theta = wt\%Cu^\theta$,

$$C_M^{Cu} = \left[C_A^{Cu} - \left(f_v^\theta * \frac{\rho^\theta}{\rho^{Alloy}} * wt\%Cu^\theta - f_v^Q * \frac{\rho^Q}{\rho^{Alloy}} * wt\%Cu^Q\right)\right] * \frac{1}{f_v^{Matrix}} \qquad (4.4)$$

Where ρ^θ, ρ^Q and ρ^{Alloy} are the Al_2Cu, Q and alloy densities, respectively. $wt\%Cu^\theta$ is the weight percent of Cu in a stoichiometric Al_2Cu particle. f_v^{Matrix} is the volume fraction of matrix which is assumed to be $1 - f_v^\theta - f_v^{Fe\ int.mtl.} - f_v^{Si\ eut.}$. Where $f_v^{Fe-int.mtl}$ and $f_v^{Si-eut.}$ are the volume fraction of Fe intermatallics and Si eutectic, respectively. It is assumed that there are just Al_2Cu precipitates present in the alloy.

For the Q phase,

$$C_M^{Cu} = \left[C_A^{Cu} - \left(f_v^Q * \frac{\rho^Q}{\rho^{Alloy}} * wt\%Cu^Q - f_v^\theta * \frac{\rho^\theta}{\rho^{Alloy}} * wt\%Cu^\theta\right)\right] * \frac{1}{f_v^{Matrix}} \quad (4.5)$$

$$C_M^{Si} = \left[C_A^{Si} - \left(f_v^Q * \frac{\rho^Q}{\rho^{Alloy}} * wt\%Si^Q - f_v^{Fe\ int.mtl.} * \frac{\rho^{Fe\ int.mtl.}}{\rho^{Alloy}} * wt\%Si^{int.mtl.} - f_v^{Si\ eutectic} * \frac{\rho^{Si\ eutectic}}{\rho^{Alloy}} * wt\%Si^{Si\ eutectic}\right)\right] * \frac{1}{f_v^{Matrix}} \quad (4.6)$$

$$C_M^{Mg} = \left[C_A^{Cu} - \left(f_v^Q * \frac{\rho^Q}{\rho^{Alloy}} * wt\%Mg^Q\right)\right] * \frac{1}{f_v^{Matrix}} \quad (4.7)$$

Where $wt\%Cu^Q$, $wt\%Si^Q$ and $wt\%Mg^Q$ are the weight percent of Cu, Si and Mg in a stoichiometric $Al_5Mg_8Cu_2Si_6$ particle.

The diffusion field is divided into shells which surround the particle and are increasing in size by dr (Figure 4.4).

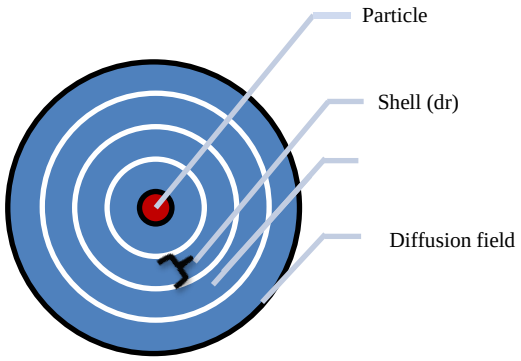

Figure 4.4: The diffusion field around particle and the diffusion shells.

Mass transport across the boundaries is given by:

$$\frac{m}{\rho} = j.A.t \quad (4.8)$$

And according to Fick`s first law

$$j = -D\frac{\partial c}{\partial r} \qquad (4.9)$$

$D$is defined according to the well-known Arrhenius relationship

$$D = D_0 \exp\left(\frac{-Q}{RT}\right) \qquad (4.10)$$

Where Q is the activation energy for diffusion of element in the matrix.
So one can calculate the mass transfers in and out of each shell,

$$m = D\rho\ \frac{\partial c}{dr} 4\pi r^2 t \qquad (4.11)$$

$$m_{in} = D\ \left[\frac{(C_{n-1} - C_n)\rho^{Alloy}}{dr}\right] 4\pi (r_{n-1})^2 dt \qquad (4.12)$$

$$m_{out} = D\ \left[\frac{(C_n - C_{n+1})\rho^{Alloy}}{dr}\right] 4\pi (r_n)^2 dt \qquad (4.13)$$

4.1.3.2 Initial conditions

The initial concentration of each element in matrix is set to c_i^M and the concentration of the element at the particle-matrix interface is c_i^{sol}.

$$c_i(r, 0) = c_i^M \qquad r_p < r \leq r_{df} \qquad (4.14)$$

$$c_i(r, 0) = c_i^{sol} \qquad r = r_p \qquad (4.15)$$

The model requires that c_i^{sol} be greater than c_i^M otherwise instead of dissolution growth will occur. This situation is demonstrated in Figure 4.5. As the particle dissolves the concentration profile in the diffusion field around the particle is changing according to Figure 4.6, where Cu concentration in particle, interface and alloy is shown by C_P, C^{sol} and C_A, respectively.

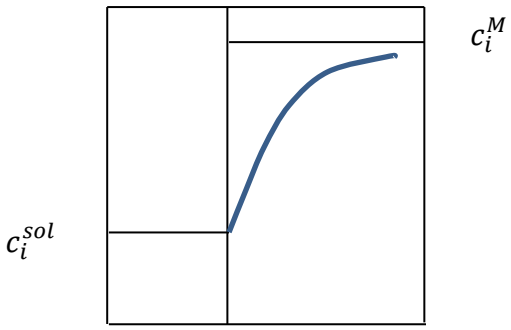

Figure 4.5: A schematic presentation of the situation in which particle growth occurs instead of dissolution.

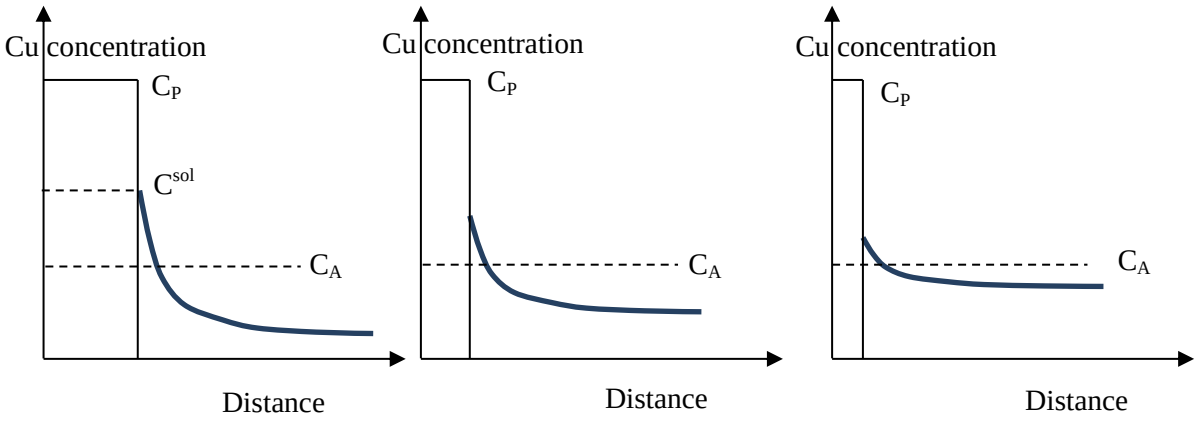

Figure 4.6: A schematic presentation of the Concentration profile in the matrix around particle as dissolution time elapses.

4.1.3.3 Boundary conditions

Since it is assumed that we have equally sized diffusion fields that stay unchanged in size, and there is not any impingement of diffusion filed into each other, so there is no flux at the outer boundary of the diffusion field.

$$\frac{\partial c_i}{\partial r} = 0 \qquad r = r_{df} \qquad (4.16)$$

This implies that

$$m_{out}(n) = 0 \qquad (4.17)$$

And at the particle-matrix interface which is stationary we have

$$m_{in}(1) = D\frac{(c^{sol} - c_i)\rho}{dr/_2} 4\pi\left(r(1) - dr/_2\right)^2 t \qquad (4.18)$$

4.1.4 Moving mesh

A schematic of this approach is shown in Figure 4.7. It can be seen that as the particle is dissolving and reducing its size, so the matrix area is getting bigger. Re-meshing is done after each time step which results in bigger mesh sizes (larger dr) as time elapses.

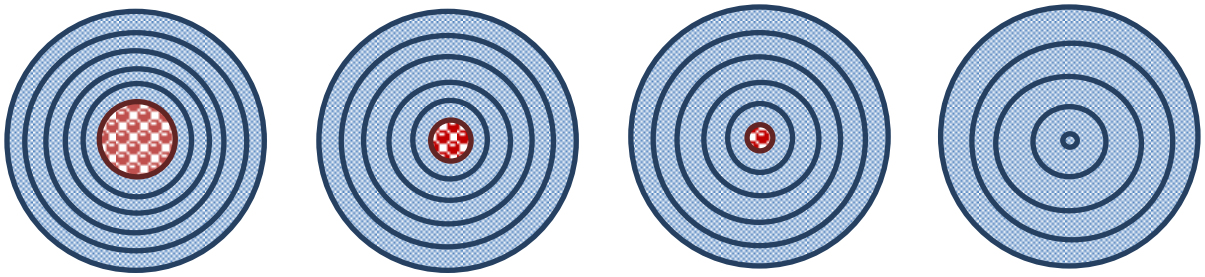

Figure 4.7: A schematic of moving interface dissolution process.

4.1.4.1 Governing equations

For a multicomponent particle that consists of n chemical elements (Sp_i , $i \in \{1, \dots, n\}$), the stoichiometry of the particle can be denoted by $(Sp_1)_{m_1}(Sp_2)_{m_2}(Sp_3)_{m_3}(\dots)(Sp_n)_{m_n}$.The numbers m_1, m_2, …, m_n are stoichiometry constants. Since we have assumed that the particles remain stoichiometric and that there is always thermodynamic equilibrium at the particle-interface matrix, we can use the Gibbs free energy of the stoichiometric compound to obtain the

hyperbolic relationship for the interfacial concentrations. The interfacial concentration of species i is denoted by c_i^{sol}.

$$\left(c_1^{sol}\right)^{m_1}\left(c_2^{sol}\right)^{m_2}(\ldots)(c_n^{sol})^{m_n} = K_{sol} = K_{sol}(T) \qquad (4.19)$$

The factor K is referred to as solubility product. It depends on temperature T according to an Arrhenius relationship

$$K = K_0 \exp\left(\frac{-\Delta H}{RT}\right) \qquad (4.20)$$

We denote the position of the moving particle-matrix interface by R(t) which extends from 0 to r_{df}.

Transportation of each solute element in a finite matrix, $M(t) = (R(t), r_{df})$ with R(t) the moving boundary and r_{df} the fixed boundary, is described as follow,

$$\frac{\partial c_i(r,t)}{\partial t} = \frac{D_i}{r^a}\frac{\partial}{\partial r}\left\{r^a \frac{\partial c_i(r,t)}{\partial r}\right\} \qquad (4.21)$$

Where D_i and c_i are the diffusion coefficient and the concentration of the species i in the matrix. $c_i(r,t)$ is continuous, and has continuous derivatives with respect to t and r. The geometry is planar, cylindrical and spherical for respectively a = 0; 1 and 2. The particle-matrix interface, R(t), moves due to the mass balance which yields:

$$\int_{r=0}^{r_{df}} c_i(r,t) r^a dr = c_i^p \cdot \frac{R^{a+1}}{a+1} + \int_{r=R(t)}^{r_{df}} c_i(r,t) r^a dr \qquad (4.22)$$

Differentiating with respect to t of Equation 4.22 and using Equation 4.21, Equation 4.23 can be obtained which is used to find the dissolution rate or the position of the moving boundary.

$$\frac{d}{dt}\left\{\int_{r=0}^{r_{df}} c_i(r,t) r^a dr = c^p \cdot \frac{R^{a+1}}{a+1} + \int_{r=R(t)}^{r_{df}} c_i(r,t) r^a dr\right\}$$

$$0 = c_i^p \frac{a+1}{a+1} R^a \frac{dR}{dt} + \int_{r=R(t)}^{r_{df}} \frac{dc_i(r,t)}{dt} r^a dr + \int_{r=R(t)}^{r_{df}} c_i(r,t) \frac{dr^a}{dt} dr$$

$$0 = c_i^p R^a \frac{dR}{dt} + \int_{r=R(t)}^{r_{df}} \frac{D_i}{r^a} \frac{\partial}{\partial r} \left\{ r^a \frac{\partial c_i(r,t)}{\partial r} \right\} r^a dr + \int_{r=R(t)}^{r_{df}} c_i(r,t) \frac{dr^a}{dr} \frac{dr}{dt} dr$$

$$0 = c_i^p R^a \frac{dR}{dt} + D_i r^a \frac{\partial c_i(r,t)}{\partial r} + c_i(r,t) r^a \frac{dr}{dt}$$

$$0 = c_i^p R^a \frac{dR(t)}{dt} - D_i R^a \frac{\partial c_i(r,t)}{\partial r} - c_i^{sol} R^a \frac{dR(t)}{dt}$$

$$\frac{dR(t)}{dt} = \frac{D_i}{c_i^p - c_i^{sol}} \frac{\partial c_i}{\partial r}(r,t) \qquad (4.23)$$

4.1.4.2 Boundary conditions

Fixed boundary

As it is assumed that we have equally sized diffusion fields that stay unchanged in size and there is not any soft-impingement of diffusion filed into each other, so there is no flux at the outer boundary of the diffusion field. For cases of low overall concentrations in the alloy, the cell size r_{df} may be large, and solution resembles the case where r_{df} is infinite.

$$\frac{\partial c}{\partial r} = 0 \qquad r = r_{df} \qquad (4.24)$$

Moving boundary

At the moving interface $R(t)$ we have the ‘‘Dirichlet boundary condition’’ for each alloying element. The concentration of element i in the particle is denoted by c_i^{sol}; this concentration is fixed at all stages. This assumption follows from the constraint that the stoichiometry of the particle is maintained during dissolution. As dissolution continues, particle size reduces. It is assumed that the dissolution process is diffusion-controlled, hence it is assumed that the material is always at its thermodynamic equilibrium at the precipitate-matrix phase interface. Therefore, the boundary condition is:

$$c_i(R(t),t) = c_i^{sol}(r,t) \qquad 0 < t < \infty \qquad (4.25)$$

Therefore for Q phase it can be obtained that,

$$c_{Cu}(r,t) = c_{Cu}^{sol}$$

$$c_{Si}(r,t) = c_{Si}^{sol}$$

$$c_{Mg}(r,t) = c_{Mg}^{sol}$$

$$\frac{D_{Cu}}{c_{Cu}^{Q} - c_{Si}^{sol}}\frac{\partial c_{Cu}}{\partial r}(r,t) = \frac{D_{Si}}{c_{Si}^{Q} - c_{Si}^{sol}}\frac{\partial c_{Si}}{\partial r}(r,t) = \frac{D_{Mg}}{c_{Mg}^{Q} - c_{Mg}^{sol}}\frac{\partial c_{Mg}}{\partial r}(r,t) \quad (4.26)$$

Equation 4.26 follows local mass-conservation of the components. The unknowns in above equations are the concentrations c_i, interfacial concentrations c_i^{sol} and the interfacial position $R(t)$.

4.1.4.3 Model consistency assessment

It is required that the total mass of all elements is constant in the whole dissolution cell, i.e. over $0 \leq r \leq r_{df}$. If let c_i^M be constant in matrix, then

$$\int_0^{r_{df}} c_i(r,t) r^a dr = c_i^p \frac{S_0^{a+1}}{a+1} + c_i^M \frac{{r_{df}}^{a+1} - S_0^{a+1}}{a+1} \quad (4.27)$$

Subtraction of $\int_0^{r_{df}} c_i^M r^a dr = c_i^0 \frac{{r_{df}}^{a+1}}{a+1}$ from both sides of above equation gives

$$\int_0^{r_{df}} (c_i(r,t) - c_i^0)\, r^a dr = \left(c_i^p - c_i^M\right) \quad (4.28)$$

4.1.5 COMSOL

First of all the geometry of the particles needs to be defined. Four different geometries were considered; spherical, planar, cylindrical and elliptical geometries. The diffusion equation (Equation 4.24) is solved using finite difference method to find the concentration profile after each time step. The mesh structure that is used is shown in Figure 4.8. The mesh quantification is shown in Table 4.1. For two-dimensional models finer and fine meshes and for three dimensional modelling normal and coarse meshes were used.

$$\frac{\partial c_i}{\partial t} + \nabla.(-D_i \Delta c_i) = 0 \qquad (4.29)$$

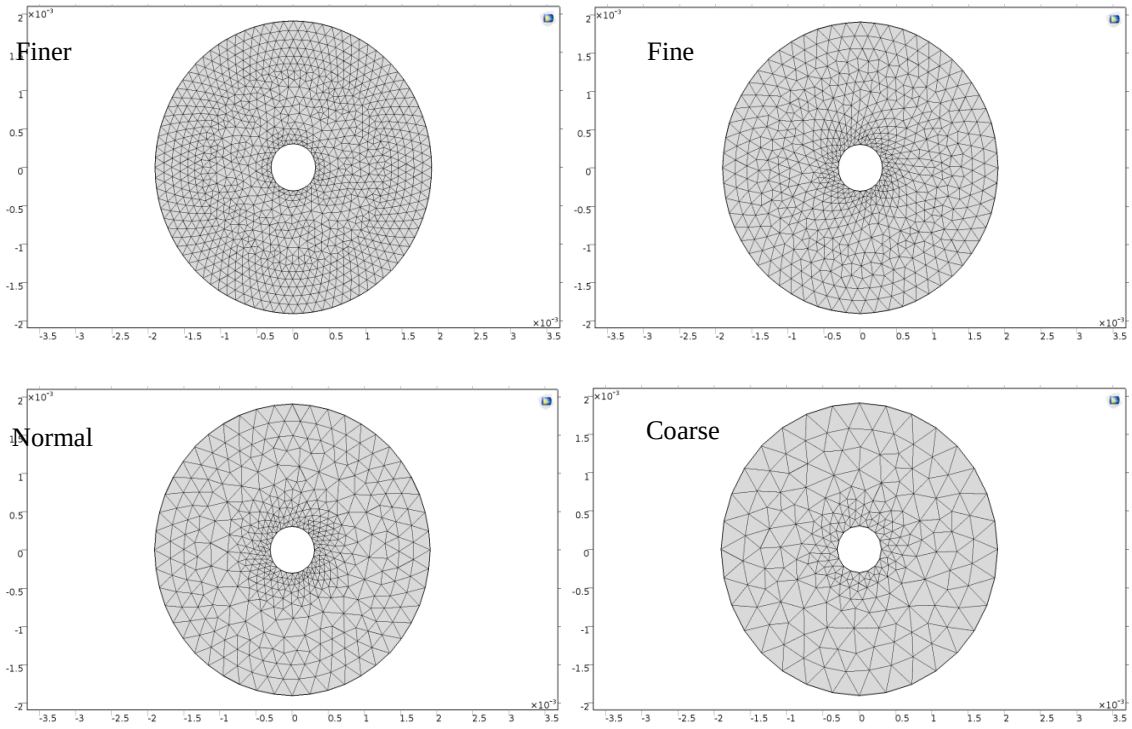

Figure 4.8: Mesh used in COMSOL.

Table 4.1: COMSOL mesh quantification.

Mesh	Number of elements	$\frac{\text{Number of elements}}{\text{Area of the diffusion field}}\ [mm^{-2}]$
Extremely fine	24488	6.87E+03
Extra fine	6540	1.83E+03
finer	2072	5.81E+02
fine	1272	3.57E+02
normal	910	2.55E+02
coarse	436	1.22E+02
coarser	286	8.02E+01
Ultra coarse	128	3.59E+01
Extremely coarse	100	2.81E+01

4.2 Morphology analysis

4.2.1 COMSOL

COMSOL software is used for analysis of the effect of morphology on the particle dissolution. In this method, the radius of the field, r_s, is calculated based on constant volume (3-D modelling) or constant area (2-D modelling). Therefore, we have

$$SDAS^3 = 4/3\pi r_{ss}^3 = a^3 = \pi r_{sc}^2 h = 4/3\pi abc \qquad (4.30)$$

$$SDAS^2 = \pi r_s^2 = a^2 = \pi ab \qquad (4.31)$$

In the model it was assumed that $h = 2r_s$ for cylindrical geometry.

4.2.2 MATLAB

To investigate the effect of morphology on the particle dissolution, MCMM method is applied for spherical, cylindrical and planar shapes. It should be noted that MCMM solves the diffusion equation in 1-D. Therefore the height of the particle and field (for cylinder or planar) is assumed to be equal.

For calculation of r_s (radius of the diffusion field) in spherical coordination, following equation is used

$$SDAS^3 = V_s = \frac{4}{3}\pi r_s^3, \quad r_0 = r_s(F_{vb})^{1/3} \qquad (4.32)$$

For calculation of r_s (radius of field circle) in cylindrical coordination, we can use two approaches.

1) Constant volume with assigning cylinder height as a function of radius

$$H_s = H_0 = r_s \rightarrow SDAS^3 = V_c = \pi r_s^3, \quad r_0 = r_s(F_{vb})^{1/2} \qquad (4.33)$$

2) Constant area

$$SDAS^2 = A_c = \pi r_s^2, \quad r_0 = r_s(F_{vb})^{1/2} \qquad (4.34)$$

For calculation of r_s in planar coordination, we can use three approaches.

1) Constant volume in which height and width are functions of radius

$$H_s = H_0 = W_0 = W_s = 2r_s \rightarrow SDAS^3 = V_p = 8r_s^3, \quad r_0 = r_s F_{vb} \qquad (4.35)$$

2) Constant area in which the width is a function of radius

$$W_0 = W_s = 2r_s \rightarrow SDAS^2 = A_p = 4r_s^2, \quad r_0 = r_s F_{vb} \qquad (4.36)$$

3) Constant interface

$$SDAS = I_p = 2r_s, \quad r_0 = r_s F_{vb} \qquad (4.37)$$

4.3 Thermodynamic analysis

First of all we need to analyze the alloy thermodynamically. A thermodynamic analysis was conducted using FactSage and ThermoCalc software to obtain phase diagram and predict the stability of different phases. These are our guidance tools to establish the temperature ranges over which the phase dissolution occurs and equilibrium concentrations at the particle-matrix interface in the matrix. Figure 4.9 to 4.11 illustrate the results of this analysis. It is seen in Figure 4.9 that the temperature range for dissolution is 475 °C - 505 °C. As shown in Figure 4.10, the equilibrium phases and the temperature ranges in which they are present are Al_2Cu, up to 465°C; $Al_5Cu_2Mg_8Si_6$ (i.e., Q phase), up to 534°C and Iron phase, up to 616 °C. This implies that at solution temperatures of 480 °C and 500 °C for the holding temperature of long enough Al_2Cu will completely dissolve but Q phase will be present to some extent after solution treatment as well as iron phase. It should also be noted that solution treatment temperature cannot be over 505 °C as Cu rich phases start to melt. Also, from the phase diagram we can obtain that at 480 °C and 500 °C the Cu concentration at the interface in the matrix is 3.1 and 3.7, respectively.

After finding an appropriate dissolution temperature, we need to find the diffusivity of the elements present in each phase. For the dissolution of Al_2Cu phase there is just Cu that diffuses, however, for the dissolution of $Al_5Mg_8Si_6Cu_2$, Cu, Mg and Si are the elements which control the dissolution rate. The diffusivity of these elements in Al [75] is shown in Figure 4.11. Although a clear trend of diffusivity: $D_{Si} > D_{Mg} > D_{Cu}$ is seen in this figure, however, at the dissolution temperatures of 480 °C to 500 °C, which correspond to 1000/T of 1.29 to 1.32, the

diffusivity of these elements in Al are so close to each other that we can say all of them are rate controlling in the dissolution of Q phase.

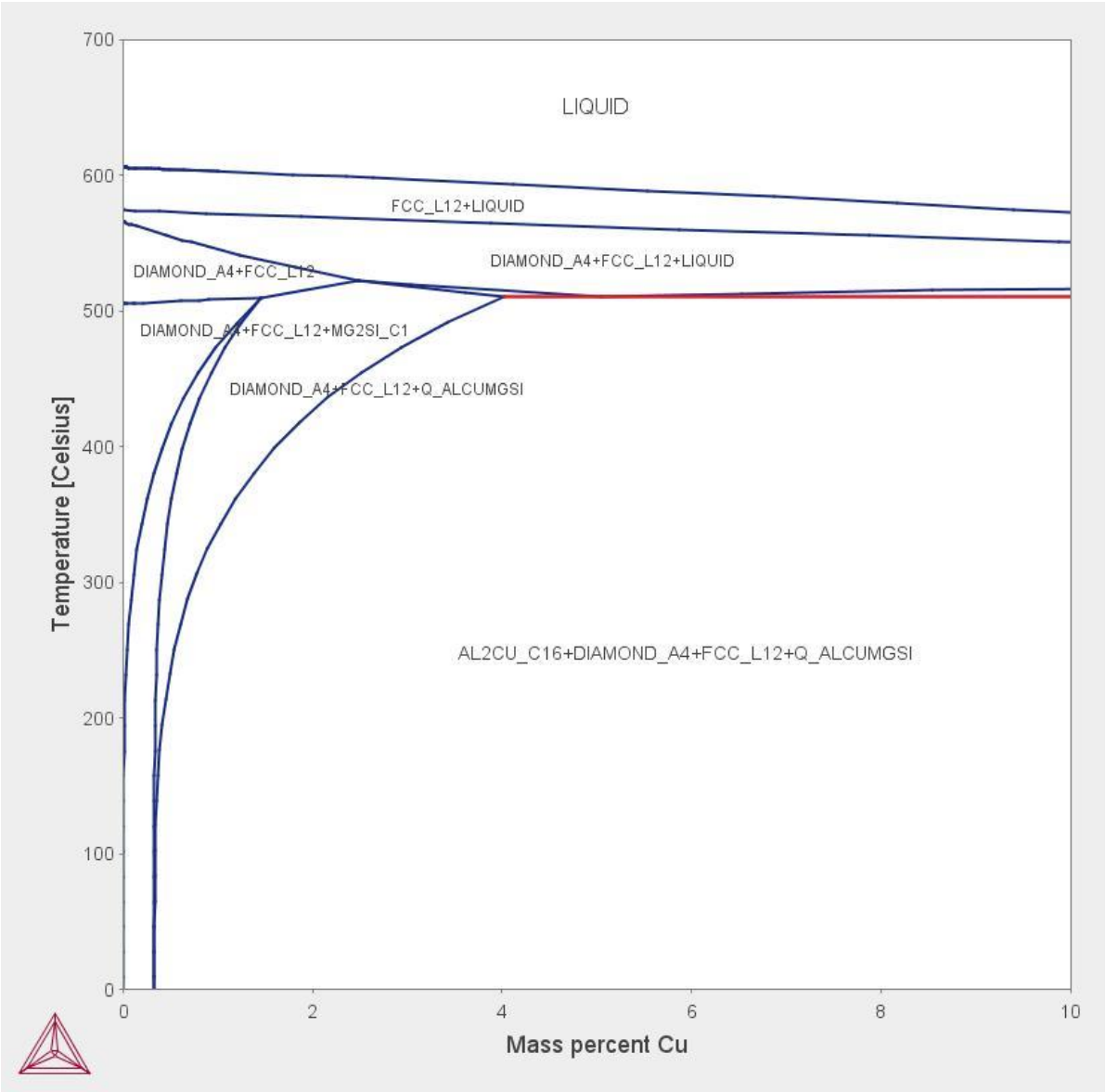

Figure 4.9: Phase diagram of AlB319.

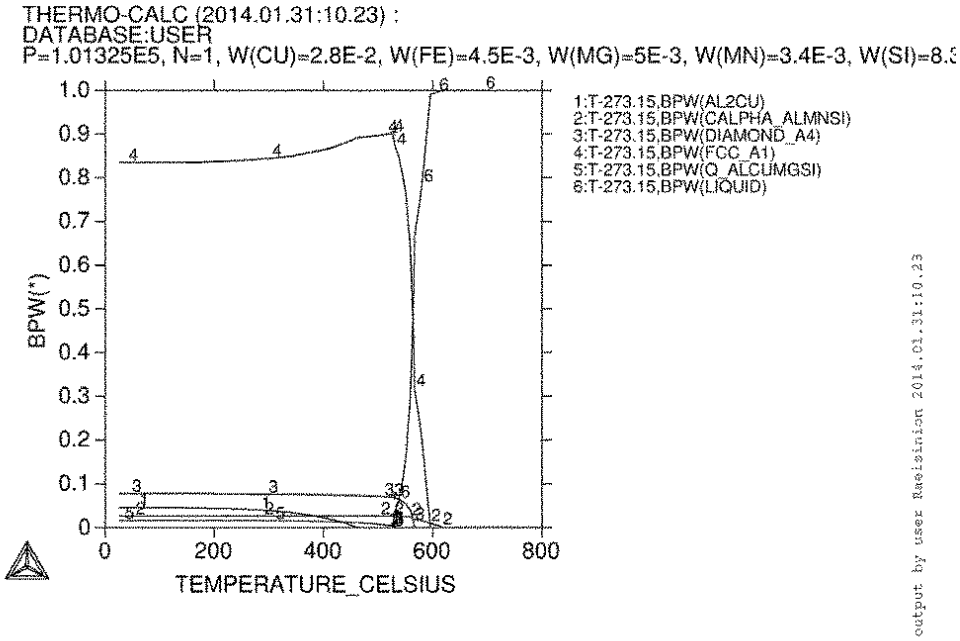

Figure 4.10: Phase stability in AlB319 at different temperatures.

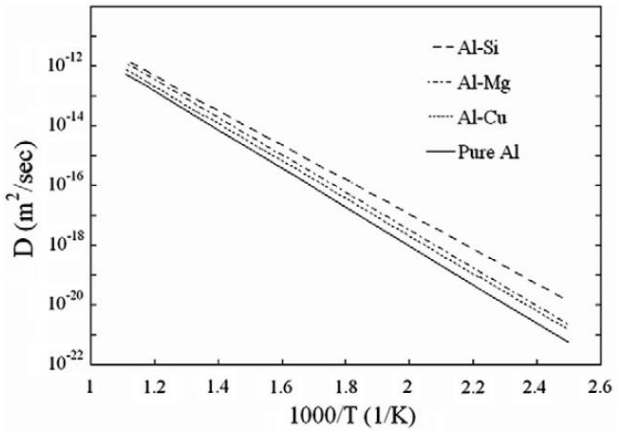

Figure 4.11: Calculated diffusion coefficients of the impurities Mg, Si and Cu in Al in comparison with Al self-diffusion [75].

Volume fraction of Q phase has been assumed to be 0.006 according to ThermoCalc. Densities of the θ and Q and Fe phases are 4.34 g/cm^3 [76,77], 2.79 g/cm^3 [76,78] and 3.3-3.6

g/cm^3 [76,77], respectively. Seifeddine et al. [79] found the density of Al-Si alloys with different concentrations of Cu added. The results are shown in Fig. 4.12.a. according to them the density of the B319 alloy that is used in this study is 2.73 g/cm^3. Nikanorov et al. [80,81] measured the density of Al-Si alloys for different Si content and their results is shown in Figure 4.12.b. According to EDS results there is 65% Si in the Si eutectic phase. By extrapolating the graph in Figure 4.12.b, we can obtain the density of Si eutectic phase which is 2.42 g/cm^3.

The enthalpies and entropies of formation of θ and Q phases and accordingly their solubility products, which can be calculated according to Equation 4.30, are shown in Table 4.2.

$$K = exp\left(\frac{\Delta S}{R} - \frac{\Delta H}{RT}\right) \qquad (4.38)$$

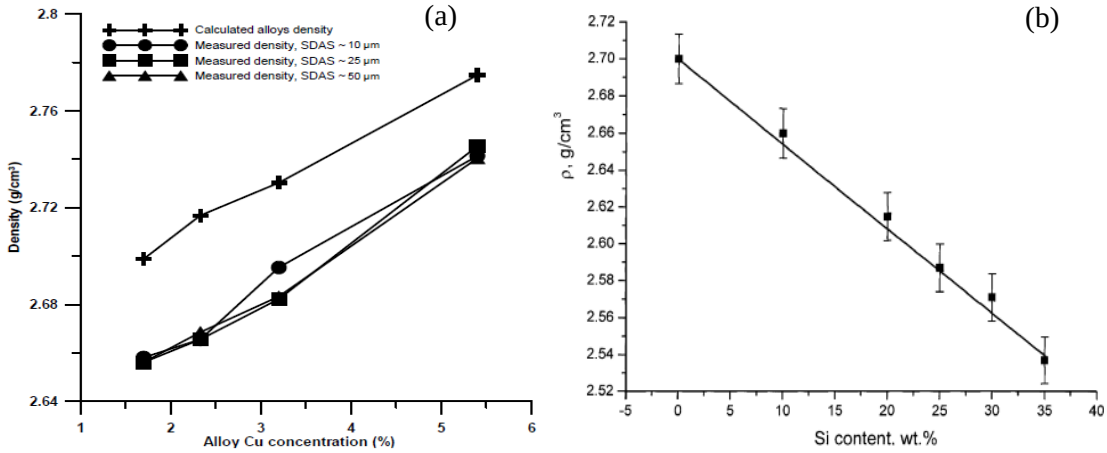

Figure 4.12: Density of Al-Si alloys at different a) Cu and b) Si content [80].

Table 4.2: Enthalpies, entropies and solubility products of the θ and Q phases.

	$\Delta H\ (\frac{J}{mol})$	$\Delta S\ (\frac{J}{mol.K})$
θ	-19600 [82]	-15.1 [83]
Q	-12900 [84-86] -16100 [86]	-20 [86]

4.4 Segregation analysis

As the alloy is a cast alloy there is microsegregation of solutes within the alloy which means that the solute concentration in the central part of a dendrite arm changes gradually during the solidification process, and we need to consider the effect of segregation in our model. Therefore, the next step is to find the segregation ratio in a dendrite arm which is used in calculating the initial concentrations of solute elements for the model. Sheil equation can be used to find the segregation ratio in a dendrite arm [87].

$$x^S = kx_0^L(1-f)^{-(1-k)} \qquad (4.39)$$

Scheil's equation indicates that the concentration approaches infinity at the end of the solidification process ($f \approx 1$). The concentration gradient becomes very high and the driving force for backdiffusion will increase. In this case the back diffusion in the solid phase cannot be neglected. When back diffusion is taken into consideration it is necessary to modify Scheil's equation. Scheil's modified equation for dendritic growth can be written as

$$x^S = kx_0^L\left(1-\frac{f}{1+D_s\frac{4\theta}{\lambda_{den}^2}}\right)^{-(1-k)} \qquad (4.40)$$

The quantity that has been used to describe segregation behaviour of an alloying element is the segregation ratio which is the ratio of the highest and lowest values of the concentration of the alloying element in a dendritic microstructure.

$$S = \frac{x_{max}^s}{x_{min}^s} \qquad (4.41)$$

S is the ratio of the highest and lowest values of the concentration of the alloying element in a dendrite crystal aggregate. The expression for S has been calculated as in equation 4.24 which shows microsegregation ratio,

$$S = \frac{1}{1 - \left(1 - \frac{k\left(1 - \frac{2}{\pi} e^{-\frac{\pi^2 D_s}{\lambda_{den}^2} t_{sol}} \right)}{1 - \frac{2k}{\pi} e^{-\frac{\pi^2 D_s}{\lambda_{den}^2} t_{sol}}} \right) e^{-\frac{\pi^2 D_s}{\lambda_{den}^2} t_{sol}}} \qquad (4.42)$$

In which t_{sol} is the solidification time, λ_{den} the primary dendrite arm spacing, k the partition coefficient, and D_s the diffusion coefficient. The solidification time and primary dendrite spacing are related to the cooling rate and can be defined as follow:

$$t = \frac{\Delta T}{-dT/dt} \qquad (4.43)$$

$$\lambda_{den} = A\,(-\frac{dT}{dt})^n \qquad (4.44)$$

The cooling rate can be found according to equation 4.27[88]:

$$\log\left(\frac{dT}{dt}\right) = -\left[\frac{\log(SDAS) - 2.37}{0.4}\right] \qquad (4.45)$$

The partition coefficient for element i can be found as follows,

$$k_i = \frac{C_i^S}{C_i^L} \qquad (4.46)$$

Where C_i^S and C_i^L are the concentration of the alloying element is solid and liquid, respectively. The concentration of the alloying element is a function of both time and position. It can be found by solving Fick's second law for the diffusion process. If the origin ($y = 0$) is located at the centre of a dendrite arm, the concentration of the alloying element in the solid phase can be written as

$$x(y,t) = x^{S/L} - \left(x^{S/L} - x_{min}\right) e^{-\frac{4\pi^2 D_s}{\lambda^2} t} cos\frac{2\pi y}{\lambda} \qquad (4.47)$$

Where $x(y,t)$, $x^{s/L}$ and x_{min} are the concentration of the alloying element (mole fraction), the concentration of the alloying element in the solid at the interface at time t and x_{min} the concentration of the alloying element at the centre of the dendrite at time t, respectively. y is the distance from the centre of the dendrite, which corresponds to the minimum concentration of the solute, and λ is half of the SDAS and D_s is the diffusion constant of the alloying element in solid.

4.5 Experiments

4.5.1 Wedge casing

The experimental work was done on a 319-type alloy, supplied in the form of industrially cast ingots by Nemak Engineering Centre, Windsor, Ontario. These were remelted and cast into a wedge mould at CANMET Materials Technology Laboratory located in Hamilton, Ontario. No strontium or grain refiner additions were made to this alloy. A schematic of the wedge casting geometry used at CANMET Materials is shown in Figure 4.13. Different distances from the end-chill and correspondence microstructures are seen in the figure.

4.5.2 Chemical composition

The overall alloy composition, measured by an optical emission spectroscopy technique is shown in Table 4.3. Metallographic specimens for investigation of the as-cast microstructure were taken vertically from the bottom of the chill at distances of 12mm, 25mm, 50mm and 75mm.

Table 4.3: 319 chemical composition.

Element	Al	Si	Cu	Mg	Fe	Mn
Amount (wt%)	Bal.	8.3	2.8	0.5	0.45	0.34

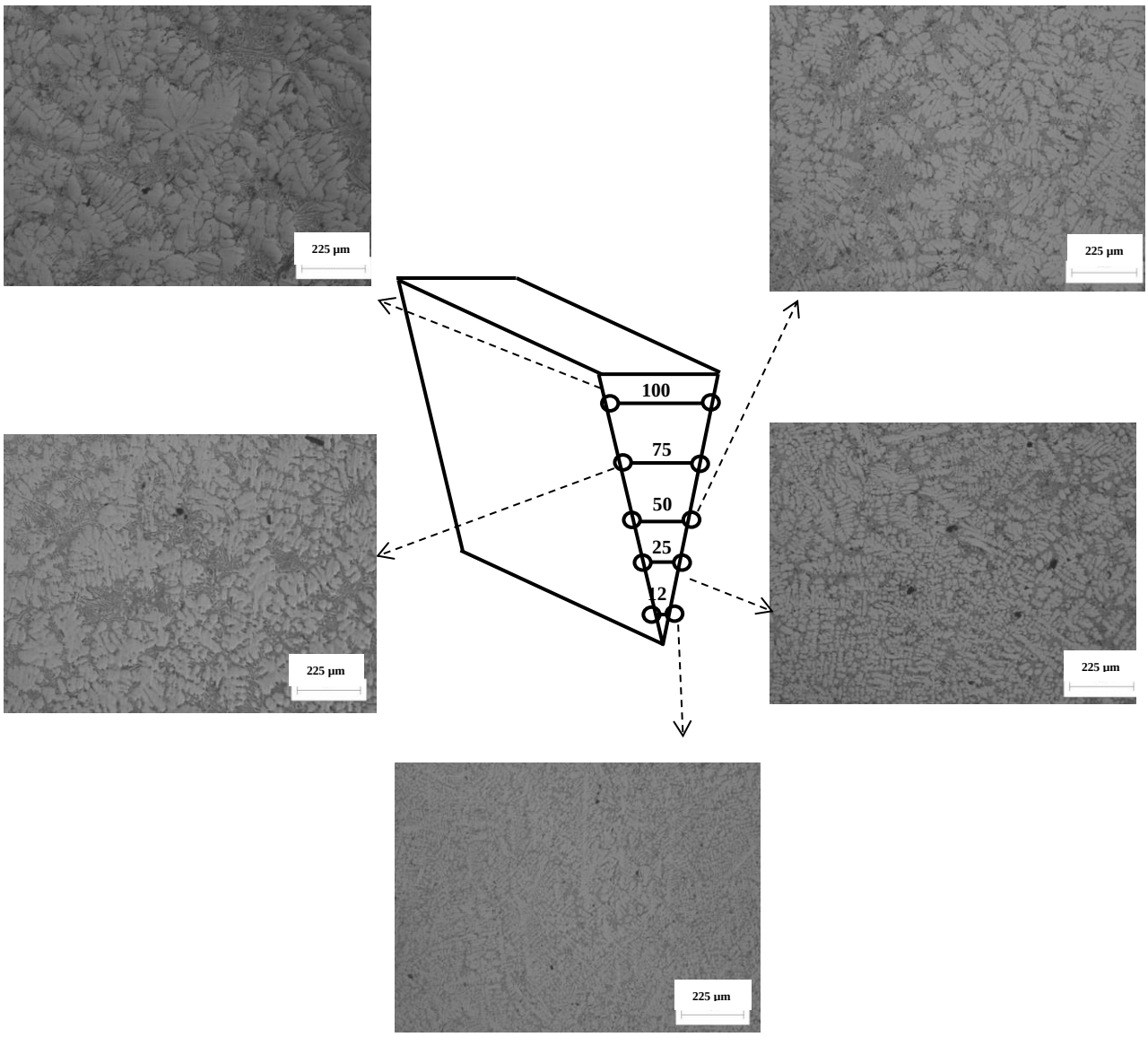

Figure 4.13: Schematic of the cast ingot showing the different sections' microstructure (distances are in mm).

4.5.3 Heat Treatment

Specimens for the heat treatment investigation were taken from a section of the casting located at 25 mm and 60 mm vertically from the end chill. Specimen dimensions were approximately 15mm (l) × 15mm (w) × 10mm (h). Solution heat treatments were done using conventional furnace (CF) and fluidized sand bath (FB) at soak temperatures of 490 °C to 510 °C

for various times up to 6 hours in CF and 2 hours in FB to investigate the effect of solution heat treatment on dissolution of particles. Measurements when calibrating the CF showed that it takes approximately 15 minutes for the samples to reach the set temperature. Therefore, samples are exposed to an unavoidable non-isothermal heating process upon reaching to the desired temperature, but considering the length of the overall homogenization process this represents a minimal amount of time and can be ignored. Samples were then removed from the furnace and immediately quenched into water at temperature of 21 °C.

4.5.4 Metallography and Image Analysis

All metallographic examinations were carried out on vertical sections perpendicular to the solidification direction. The specimens were ground and polished using MD-Nap polishing cloth with diamond suspension and MD-Chem cloths with colloidal silica suspensions to finish. Microstructural investigations were done using optical and scanning electron microscopes. Image quantification of area fraction for various phases was done on 2D images using image analysis software. Secondary dendrite arm spacings in the as-cast material and volume fraction of different particles present in the as-cast and heat treated specimens after different times were measured using standard ASTM method. To measure the volume fraction 50 fields in a straight line were examined.

As-cast and heat treated specimens were examined using SEM in secondary electron (SE) mode with an accelerating voltage of 20 keV and working distance of 17 mm. EDS was done to identify the various phases in the alloy.

Chapter 5

5. Results and Discussion

5.1 Microstructural investigations

The coarseness of the microstructure is characterized by SDAS which is determined by the cooling rate from solidifying temperature. The average measured primary dendrite arm spacing (PDAS), SDAS, particle sizes, interparticle spacing and volume fraction of different phases at sections distanced 25, 60 mm and 115 mm from the end chill are shown in Table 5.1.

Table 5.1: As-cast microstructure parameters.

Distance from end chill (mm)	PDAS (μm)	SDAS (μm)	Al_2Cu size (μm^2)	Distance between particles (μm)	Volume fraction of θ (%)	Volume fraction of Si eutectic	Volume fraction of iron phase	Si eutectic size (μm)
25	87	14	43.7	19.5	1.8	6.93	2.07	1.24
60	102	22	56.4	25.2	1.8	___	___	1.61
115	140	39	___	___	2.6	___	___	___

Figure 5.1.a shows the SEM micrograph of the as-cast sample with SDAS of 14 μm. Dendritic microstructure and particles that are solidified at interdendritic regions are seen. Figure 5.1.b shows particles that have formed at the interdendritic regions at larger magnification.

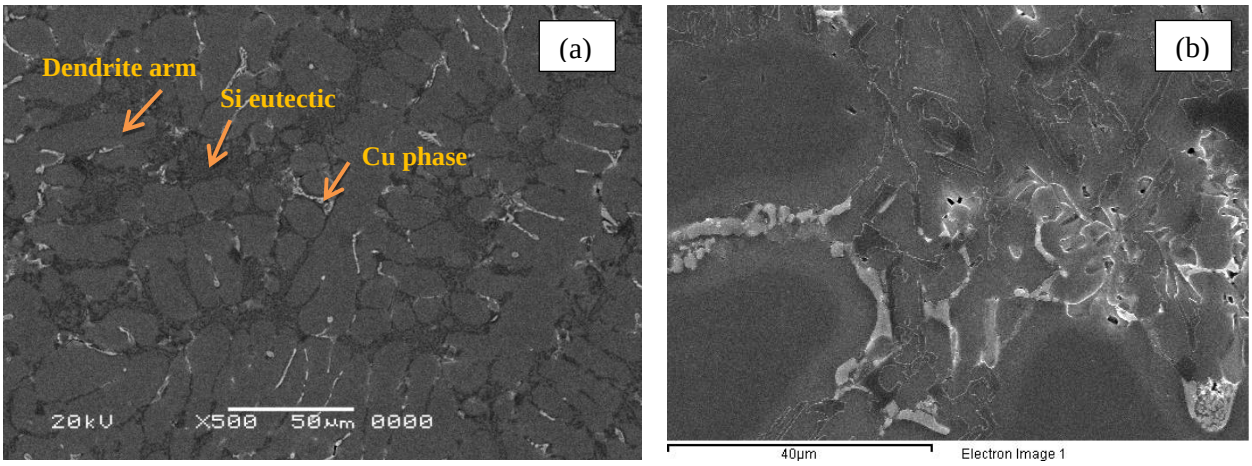

Figure 5.1: As-cast microstructure showing dendritic microstructure and different phases at a). smaller and b) larger magnification.

Figure 5.2.a and b show optical micrograph of the as-cast microstructure for two SDASs at higher magnification. It can be seen that the microstructure consists of α–Al dendrites, Si eutectic and intermetallic phases including Al_2Cu and AlFeSi. Si eutectic particles are seen as dark elongated particles which are reported to be detrimental to mechanical properties [89] as they have needle like morphologies which are crack initiators. Two types of iron intermetallic phases can be seen in the micrograph; Needle-like β-Al_5FeSi that are deleterious for mechanical properties [90] and more rounded skeleton-like α-$Al_{15}(Mn,Fe)_3Si_2$ (Figure 5.3.a). It is seen that the iron intermetallic is a preferable site for nucleation of θ phase (Figure 5.3.b). Two different precipitate phases, θ-Al_2Cu and Q-$Al_5Mg_8Si_6Cu_2$ are shown in Figure 5.4.a. It is seen in the microstructure that Q forms besides θ phase. There are two types of Al_2Cu phase; blocky and eutectic, and eutectic Al_2Cu itself has two types; coarse and fine, which are shown in Figure 5.4.b. The size of Al_2Cu particles varies from a few square micrometer to hundreds of square micrometer.

Figure 5.5 depicts the effect of solution heat treatment on microstructure, and coarseness of the microstructure on solutionizing. Fig. 5.5.a shows the as-cast microstructure. It can be seen that after solution heat treatment for 8 hrs at 500 °C at both SDASs of 14 µm (Figure 5.5.b) and 22 µm (Figure 5.5.c), the Cu-rich phase has been dissolved, however, after solution heat treatment at larger SDAS (22 µm) the iron intermetallic has undergone a little change but at smaller SDAS (14 µm) iron phase has fragmented into smaller pieces.

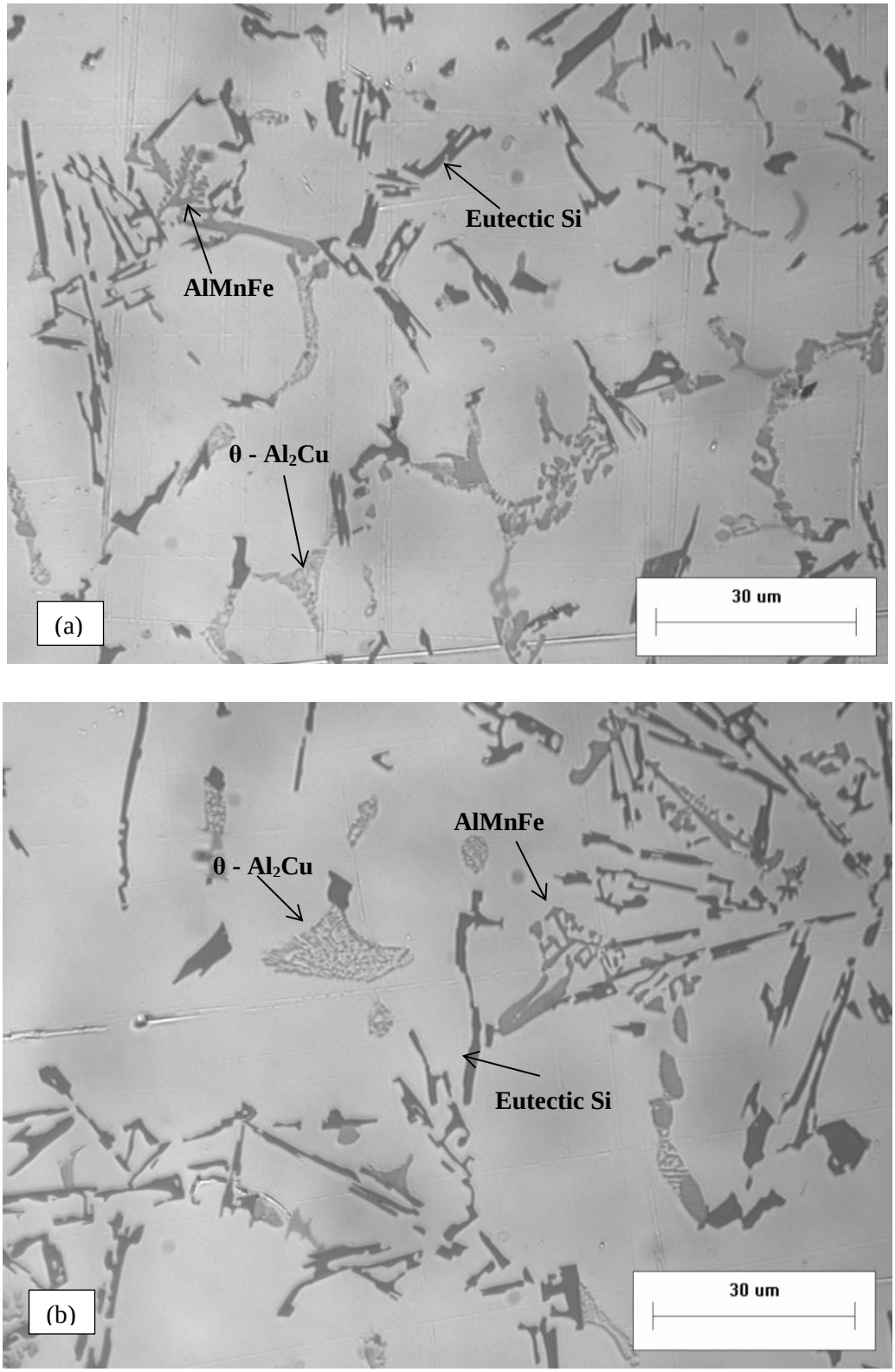

Figure 5.2: Optical micrograph of the as-cast at SDAS of a) 14 and (b) 22 µm.

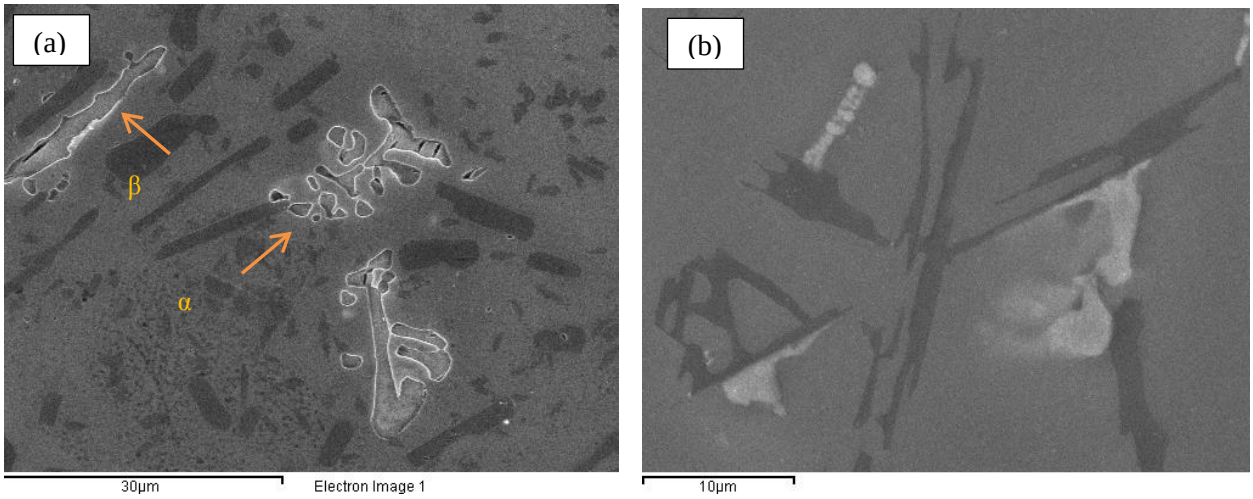

Figure 5.3: a) The morphologies of iron-intermetallic phases and b) nucleation of precipitates on Fe-intermetallic.

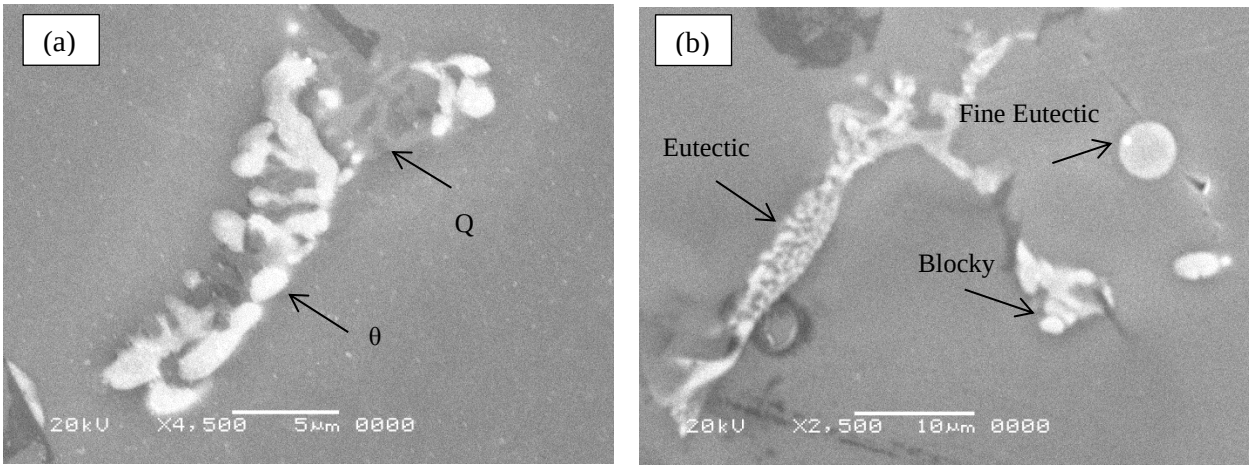

Figure 5.4: a) The θ and Q phases and b) different types of the θ phase.

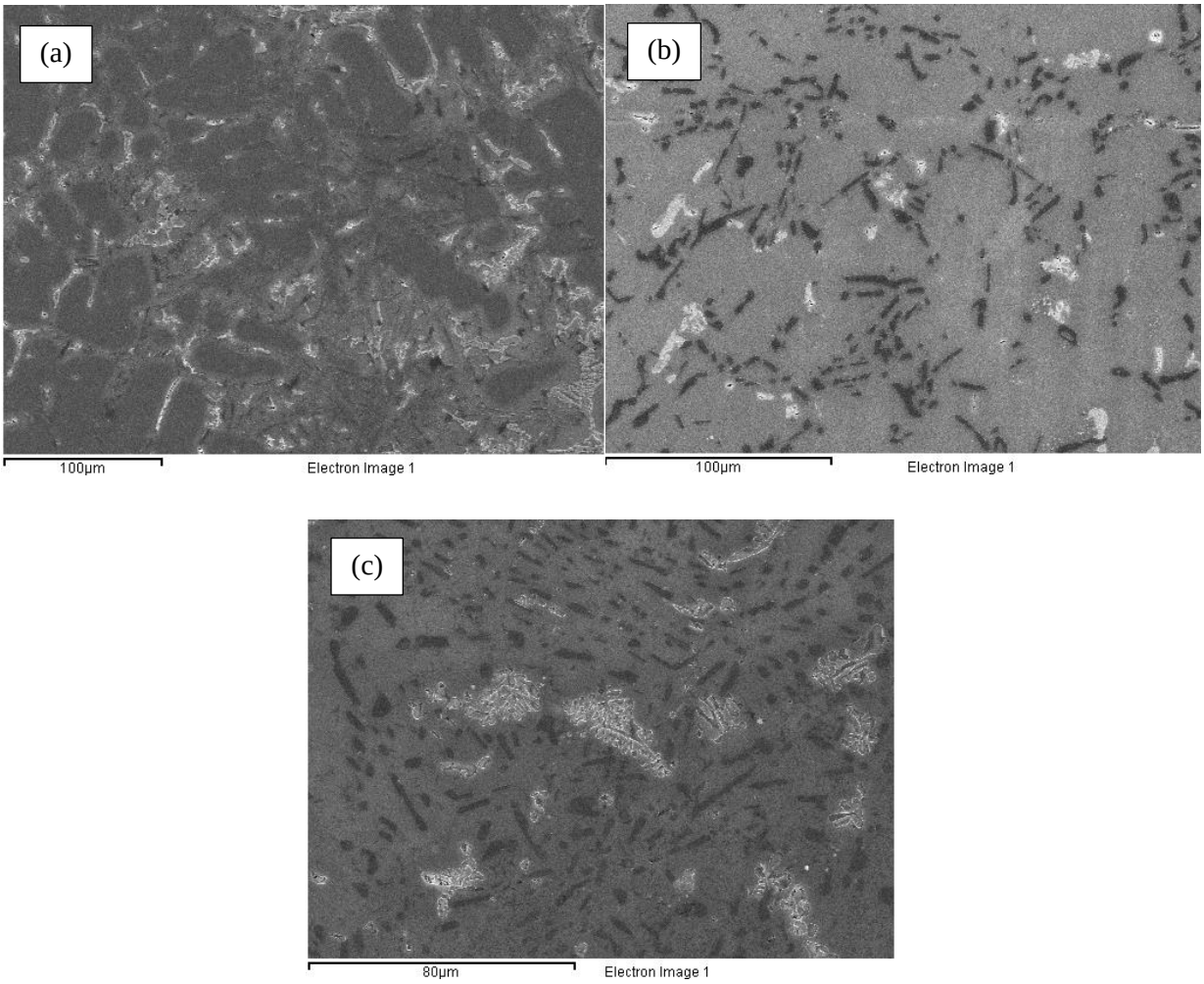

Figure 5.5: a) as-cast and solution heat treated for 8 hrs at 500 °C for SDAS of b) 14 µm and c) 22 µm.

5.2 Model predictions and experimental results

5.2.1 Conventional furnace versus fluidized bed

The measured volume fraction of Al_2Cu phase versus dissolution time in CF and FB are shown in Figure 5.6. It can be seen that there is huge difference in the dissolution time in CF and FB. At temperature of 500 °C and for SDAS of 14 µm it takes 1200 sec in fluidized bed while 7000 sec in CF for complete dissolution of Al_2Cu, and for SDAS of 22 µm it takes 2700 sec in FB while 15000 sec in CF to achieve complete dissolution. This is due to the high heat transfer rate and tight control on the temperature in FB which influences the heating time as well as

diffusion rate of solutes away from the dissolving particle and accelerates the dissolution process [40-42].

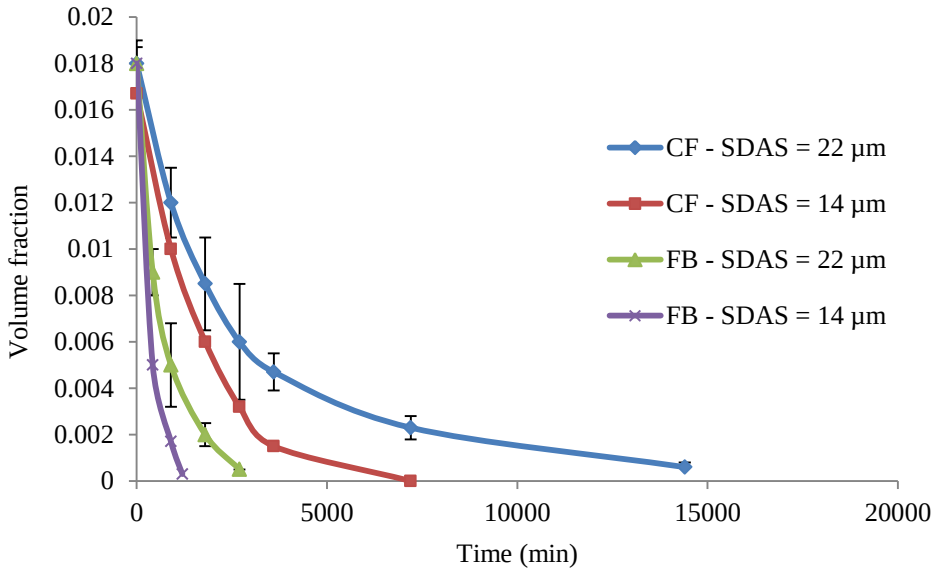

Figure 5.6: Experimentally measured volume fraction of Al_2Cu particle vs. dissolution time for Conventional Furnace (CF) and Fluidized Bed (FB).

5.2.2 Mesh sensitivity

The result of mesh sensitivity analysis for the SCFM and MCMM models are shown in Figure 5.7 and 5.8, respectively. The results are for SDAS of 22 µm and temperature of 500 °C. It can be seen that as the number of meshes goes higher than 100 for the SCFM model and 50 for the MCMM model the results are less sensitive to the number of mesh. Hence, the number of mesh used in this approximate was chosen to be 100 for the MCMM model and 50 for the FCMM model. Figure 5.9 shows COMSOL mesh sensitivity for spherical particle. It can be seen that the results are not sensitive to the mesh size when the mesh size is smaller than coarse mesh. Hence, mesh sizes smaller than ultra-coarse mesh were used in this study (i.e. Finer, Fine, Normal and Coarse).

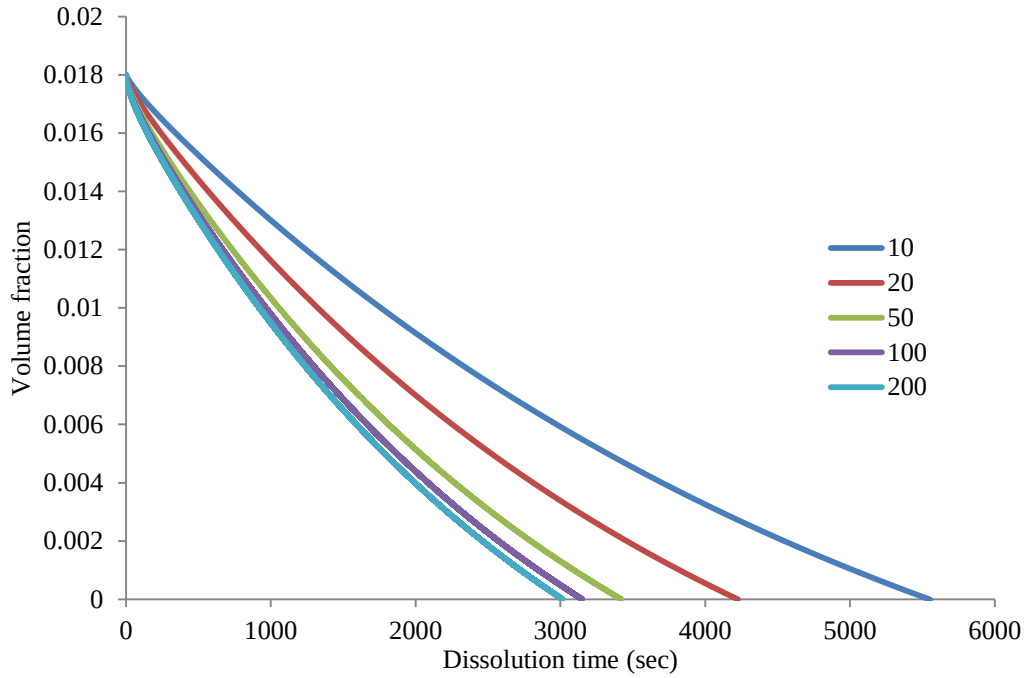

Figure 5.7: Mesh sensitivity of the SCFM approximate for different number of meshes.

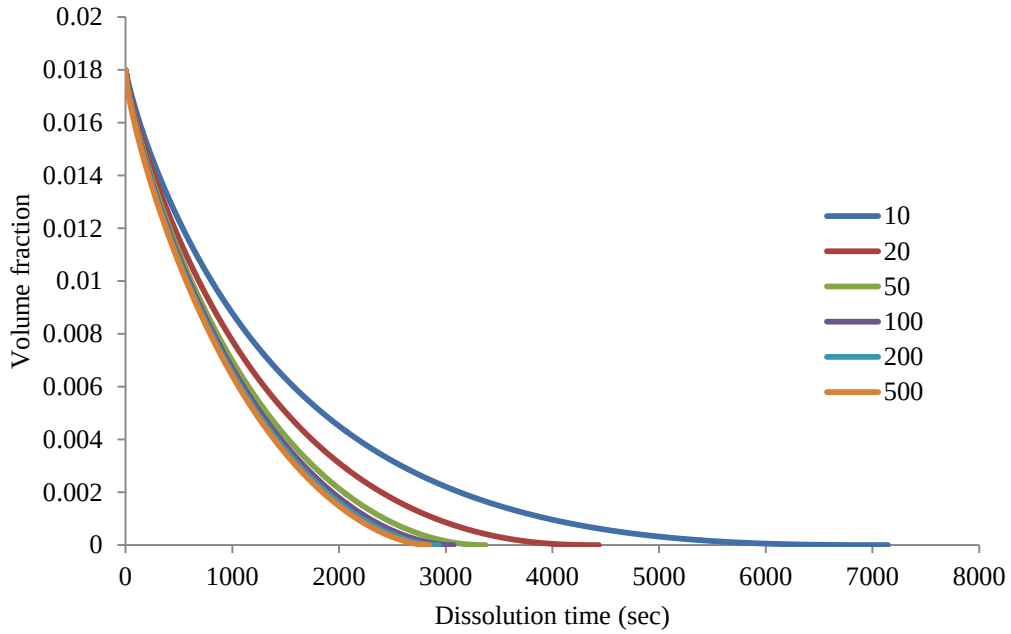

Figure 5.8: Mesh sensitivity of the MCMM approximate for different number of meshes.

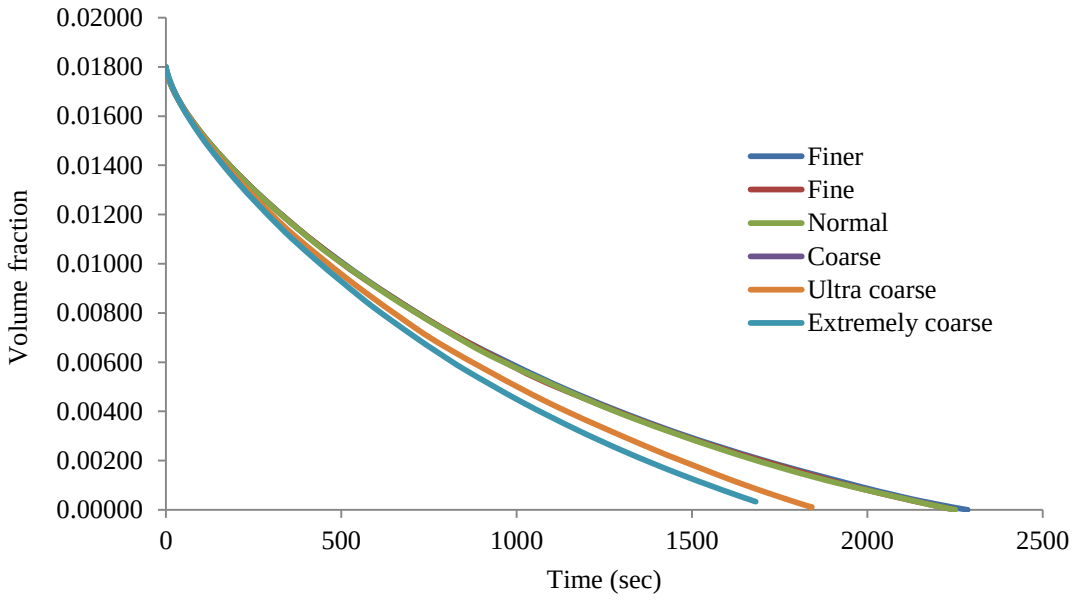

Figure 5.9: Mesh sensitivity of COMSOL approximate at different mesh sizes.

5.2.3 Single component fixed mesh model -MATLAB

Image analysis was used to determine the input parameters and to validate the model. The SCFM model predictions for single step solution heat treatment are compared to experimental results in Figure 5.10. It is noticeable that the volume fraction of Al_2Cu phase decreases rapidly at the initial stage of the dissolution but decreases at lower rate at longer times. This is due to the fact that at the initial stage of the solution heat treatment, the concentration gradient between the particle-matrix interface and the matrix is high that leads to a higher driving force for diffusion and consequently dissolution, which diminishes as the process proceeds leading to a lower driving force. It also can be seen that dissolution times are significantly affected by the fineness of the microstructure; increasing SDAS, increases the dissolution time. It is due to the fact that slower solidification rates, i.e. larger SDAS, results in increase in particle size, which in turn results in longer diffusion distance, and hence increase in dissolution time. It can be noted from the Figure that by increasing the SDAS, the initial volume fraction of Al_2Cu increases. This is due to the longer solidifying time which allows more Cu to diffuse and more Al_2Cu phase to form.

Experimental results using FB show that at 500 °C dissolution is more or less complete after 15 min, 45 min and 4 hr for SDAS of 14, 22 and 39 µm, respectively. Dissolution is more or less complete after 5 hr at 490 °C and for SDAS of 39 µm. Although, Al_2Cu particles do not fully disappear after these reported times, the amount of observed Al_2Cu following these times is so low (0.0001 wt%) that it can be considered negligible. It falls within the experimental error considering the degree of inhomogeniety inherent in castings and that the area fraction was used as an approximate for volume fraction. It can be seen that at the initial stages of the dissolution process, the model predictions falls behind the experimental measurements, which is more noticeable at larger SDAS, however, at longer times these two values are comparable. Overall, there is fairly good agreement between the model predictions for dissolution time and experimental measurements. The model is flexible in that it can predict dissolution times as a function of temperature, SDAS, diffusion field radius and initial concentration gradient, however, it can only be used for single component system such as Al_2Cu in this study in which there is just one solute component diffusing.

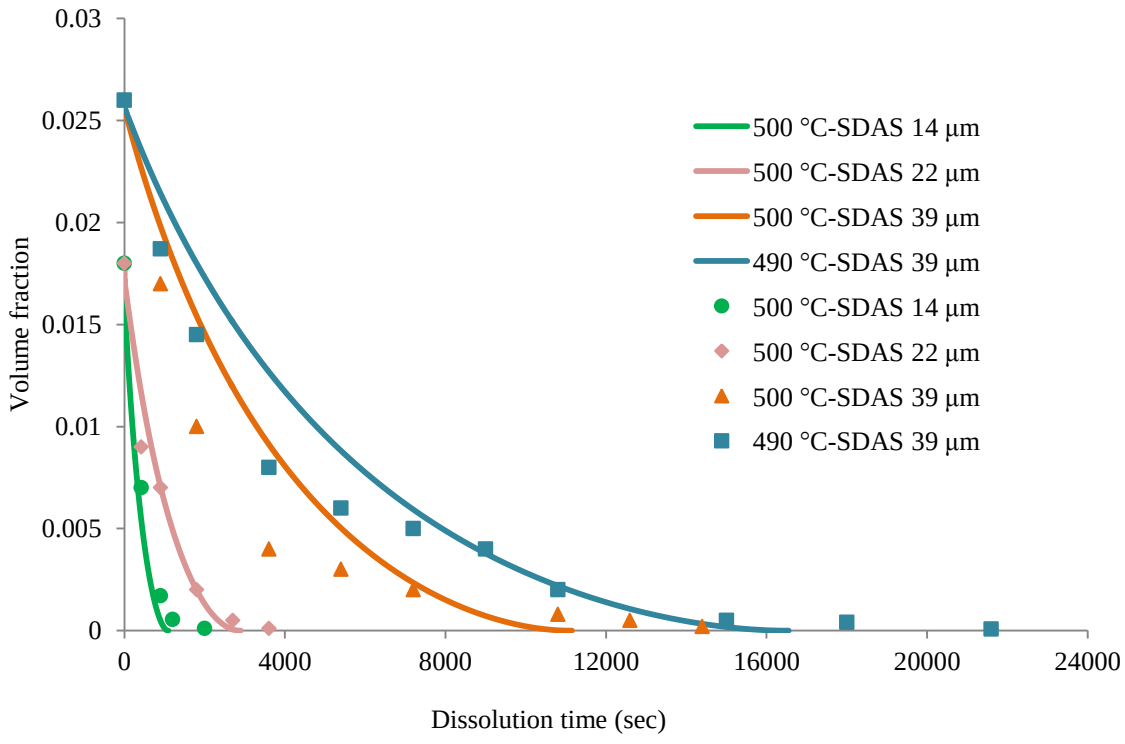

Figure 5.10: Experimental measurements (symbols) versus SCFM approach model predictions (lines).

5.2.4 Multi-component moving mesh model -MATLAB

Figure 5.11 shows the MCMM approach predictions versus experimental results for single step solution heat treatment. It can be seen that the results of this model are in better agreement with the experimental results in comparison with the SCFM model, which is indicative of higher accuracy of this model compared to the fixed boundary model. It also shows that fixed boundary is not a good assumption in this alloy system. The good agreement between experimental results and the model suggest that the assumption that the distance between particles is equal to the SDAS is reasonable. This is in consistent with image analysis observations for SDAS.

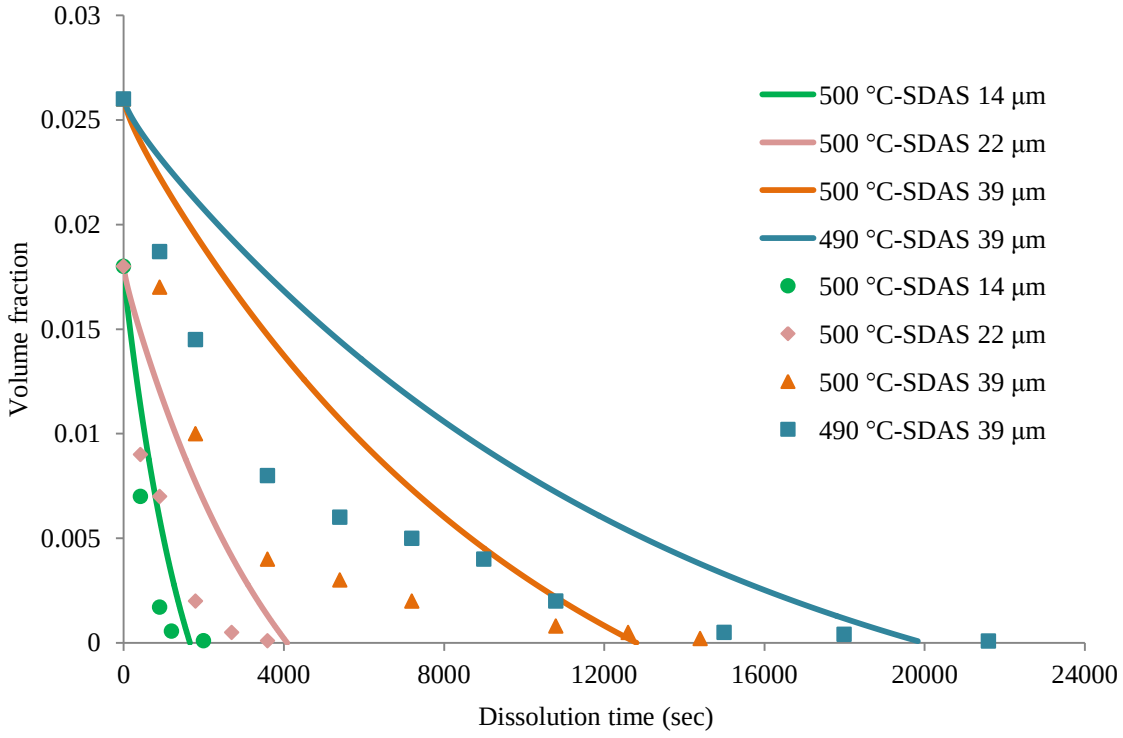

Figure 5.11: Experimental measurements (symbols) versus MCMM approach model predictions (lines).

Figure 5.12 shows the MCMM model prediction as well as experimental results of two step solution heat treatment. The model predicts that for two-step solutionizing with the first step

temperature of 490 °C and holding time of 4200 sec, it takes 1 hr at 510 °C (the second step temperature) to dissolve all the particle, and 4900 sec if the first step temperature is decreased to 500 °C. Experimental measurements using FB show 3600 and 5400 sec for the second step at 500 °C and 510 °C sec, respectively.

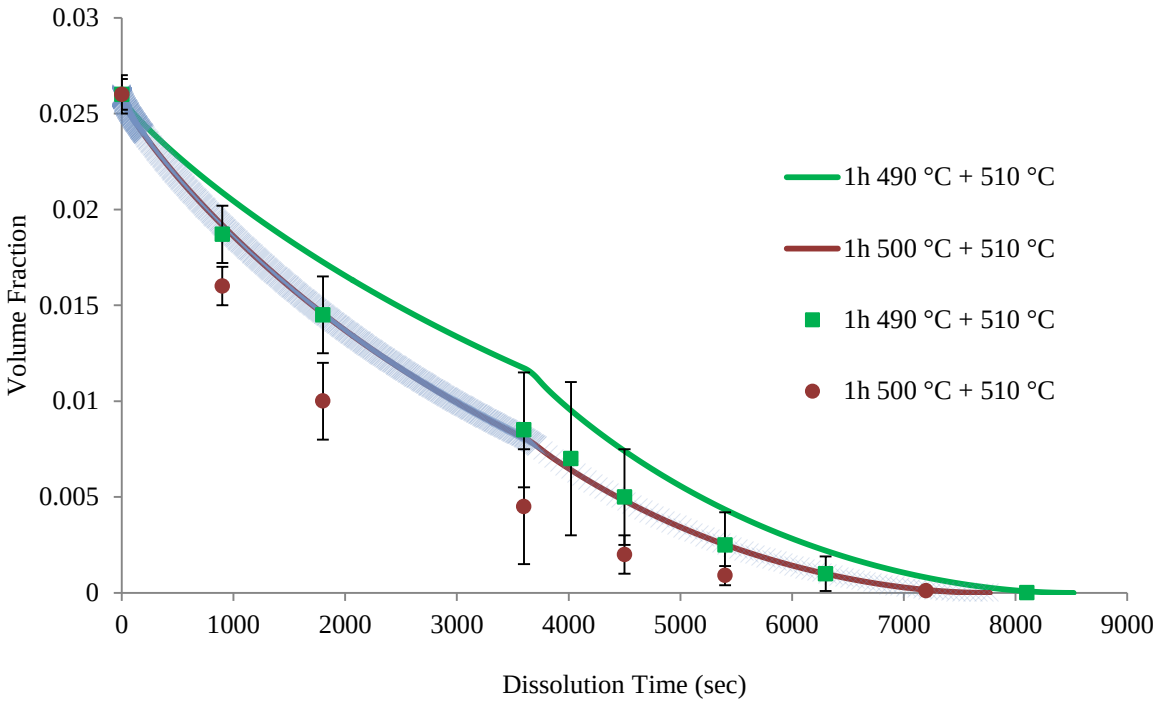

Figure 5.12: Experimental measurements (symbols) versus MCMM approach model predictions (lines).

FB was used to validate the models because it minimizes the non-isothermal heating of the sample and increases heat transfer rate, therefore, it leads to more accurate results. It is seen that there is a good agreement between model predictions and experimental data which confirms the validity of the approach and assumptions made. Therefore, it is suggested that this model can be used to determine the dissolution time at other temperatures and for other SDASs, or even further for other cast systems with different dissolving particles. Despite the general good agreement between the model prediction and experimental result, there are some deviations

which can be attributed to the assumptions made in the model to simplify the equations. First and the foremost source of error is that it was assumed that the volume fraction is equal to the area fraction when measuring the amount of particles in the alloy. The second source of error emanates from the assumption that the diffusion of each solute element is independent from the diffusion of other elements, while in reality the cross diffusion is reported to exist in the systems of multiple solute [43], which cause changes in the diffusion coefficient of each element. In addition, the high inhomogeneity in the casting alloy causes a lot of variation in the experimental measurements. Furthermore, calculation of concentration at the particle-matrix interface may have some discrepancy using different thermodynamic software—ThermoCalc vs. FactSage (shown in appendix B and C)—that results in somehow different phase diagrams which may report different results from the experimental data if we would have done Electron Probe Micro Analysis (EPMA).

5.2.5 Q-phase dissolution

MCMM model is the only approach for prediction of dissolution in multicomponent systems. It was assumed that we have both Q and θ in the diffusion field in which the dissolution of each phase affects the dissolution of the other. Figure 5.13 shows the volume fraction of the Q phase versus time until the system reaches homogeneity, for SDAS of 22 μm and at temperature of 500 °C. The initial Q phase volume fraction is assumed to be 0.006 according to ThermoCalc. It can be seen from the Figure that the Q phase does not dissolve fully in the system. This is in agreement with the ThermoCalc prediction which shows incomplete dissolution of Q phase at the studied dissolution temperatures. It can be seen from the Figure that the volume fraction of the Q phase changes rapidly within the first 2000 sec of the dissolution process when the θ phase is also dissolving and the change in volume fraction continues with a lower rate due to less driving force available for its dissolution. After 6000 sec, the volume fraction of the Q phase in the system is about 0.0023. Higher dissolution temperatures are not allowed for this alloy system as we have incipient melting of the particles instead of dissolution. The final remaining volume fraction of Q depends on the solubility product (K_{sol}) and Temperature. For the Q phase with three different components, the reduction of particle mass is based on the local mass conservation at the particle-field interface. Equation 4.23 determines the rate of the particle-matrix moving interface velocity. In some situations which depend on temperature and K_{sol}, this

equation leads to dr/dt=0 when there is no concentration gradient available in the system. In such cases the particles does not completely dissolve. In fact, K_{sol} (T) is the only factor that can change the ultimate particle size or even can cause the particle to completely dissolve.

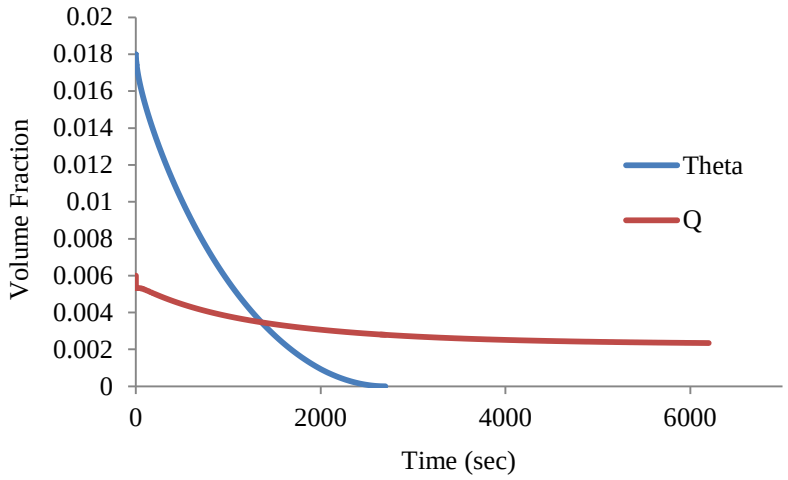

Figure 5.13: Dissolution of the Q phase.

The concentration of Cu, Mg and Si component versus position within the diffusion field at different times (t = 0, 500, 2000 and 5000 sec) are shown in Figure 5.14 to 5.16. It can be seen that the overall solute concentrations within the dendrite change from the as-cast condition values to about 0.85, 0.2 and 8.04 for Cu, Mg and Si, respectively, at the solution treatment time, and after that no further change occurs. The change in the solute concentration within the dendrite is most rapid while the Q phase is dissolving. Although homogenization is occurring for 8 min after there is no further dissolution, the solute concentration does not change greatly.

These models could not be validated through experimental measurements as the volume fraction of the Q phase was very low for the alloy studied, and we only contented with the analytical validation of the model that was done using Vermolen approach [61] which is present in the appendix D and the results of the ThermoCalc prediction which shows the value of the Q phase to be 0.0015 at the studied temperature.

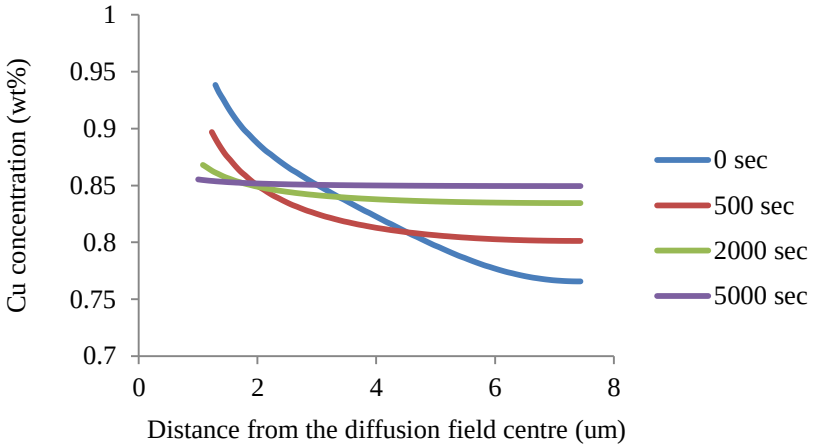

Figure 5.14: Concentration of Cu within the diffusion field at different times of heat treatment.

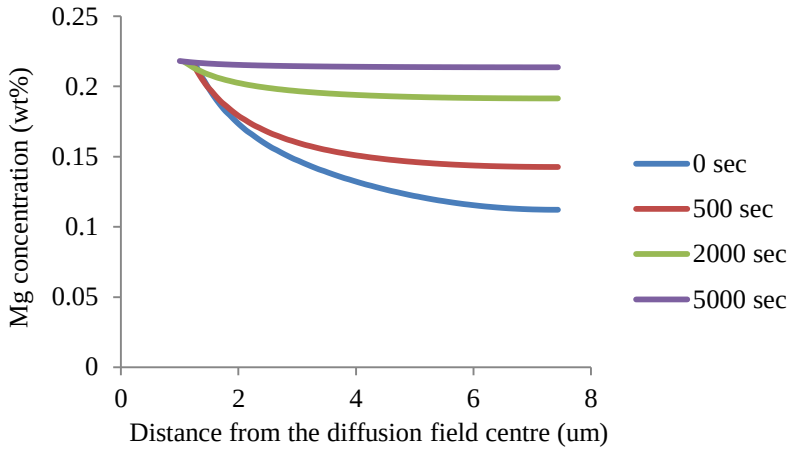

Figure 5.15: Concentration of Mg in the diffusion field at different times of heat treatment.

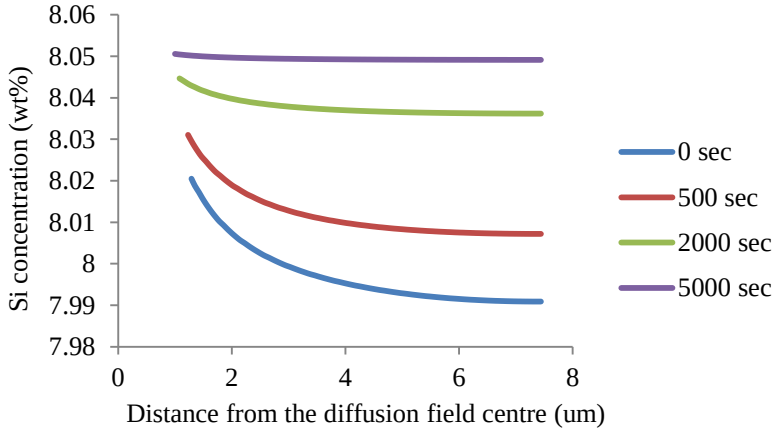

Figure 5.16: Concentration of Si in the diffusion field at different times of heat treatment.

5.2.6 COMSOL

COMSOL predictions for dissolution time of a spherical particle in 2D versus experimental measurements for single step solution heat treatment are shown in Figure 5.17. It can be seen from these figures that there are some underestimation for dissolution time. Figure 5.18 shows COMSOL prediction for an ellipse with aspect ratio of 8. Figure 5.19 shows COMSOL prediction for dissolution time of a spherical particle. Figure 5.20 and 5.21 show COMSOL predictions with finer mesh for dissolution time of an ellipsoid particle with aspect ratio of 5 and 7, respectively. Figure 5.22 shows the COMSOL prediction and experimental measurements for volume fraction of the θ phase versus dissolution time for the two-step solution heat treatment. It can be seen that by going from spherical to ellipsoid morphology, and increasing the aspect ratio of the ellipse to 8 and the ellipsoid to 7, experimental results better match the model predictions of 2D and 3D models. Considering the fact that the assumption made in the model that the particles are distanced by a SDAS is true as was confirmed via image analysis, this results suggest that the real morphology of the particles is ellipsoid. Image analysis also showed that the particles were not spherical.

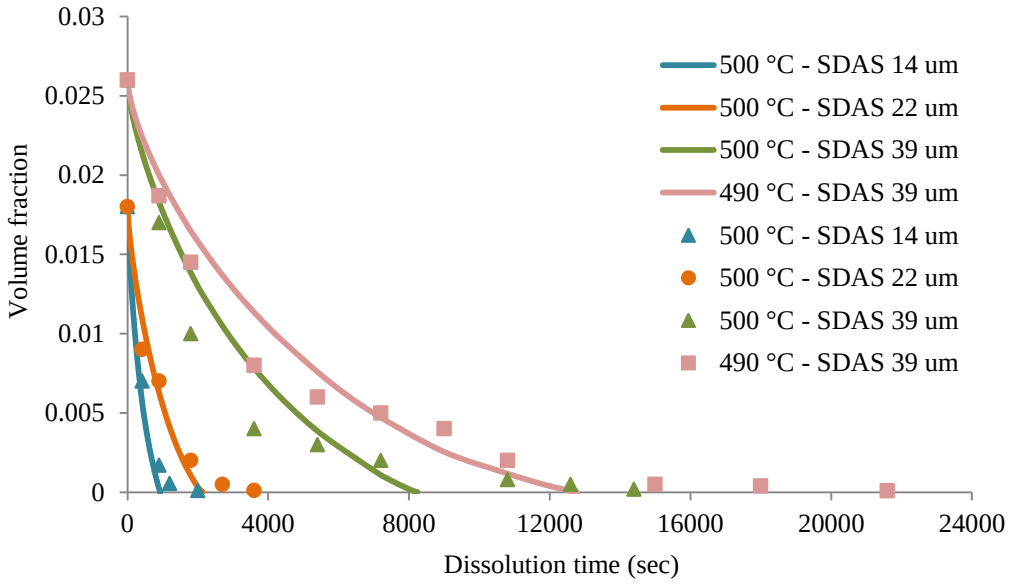

Figure 5.17: Experimental measurements (symbols) versus 2D COMSOL predictions (lines) for a spherical particle.

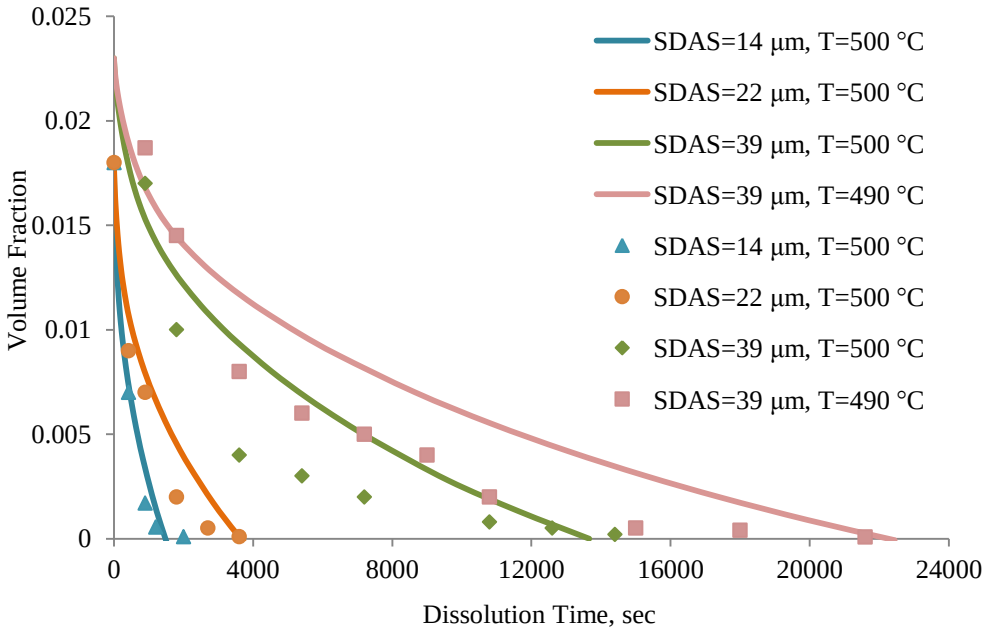

Figure 5.18: Experimental measurements (symbols) versus 2D COMSOL predictions (lines) for ellipsoid particle with aspect ratio of 8.

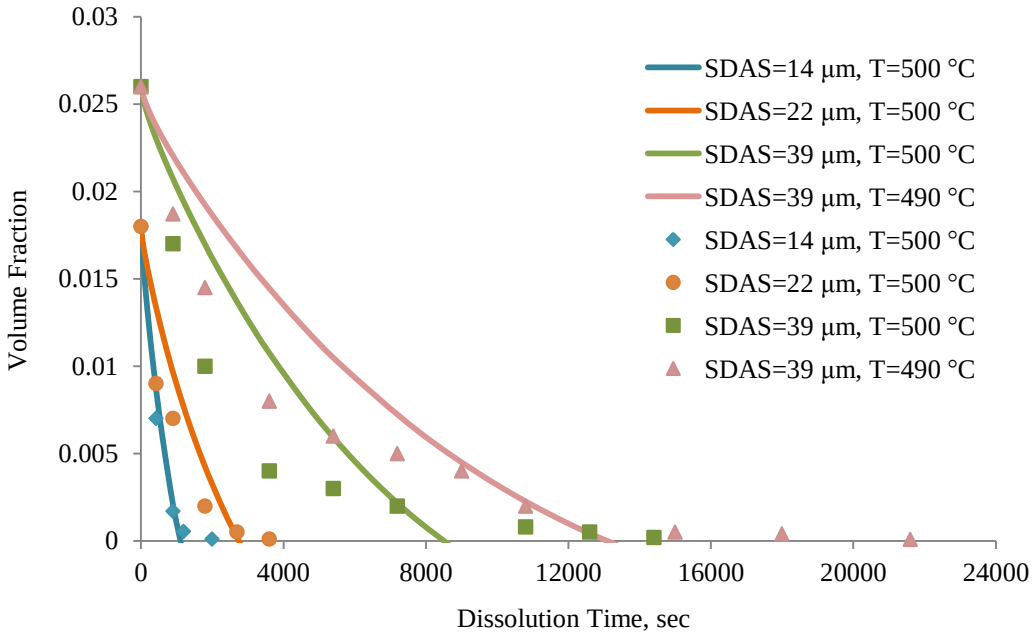

Figure 5.19: Experimental measurements (symbols) versus 3D COMSOL predictions (lines) for a spherical particle.

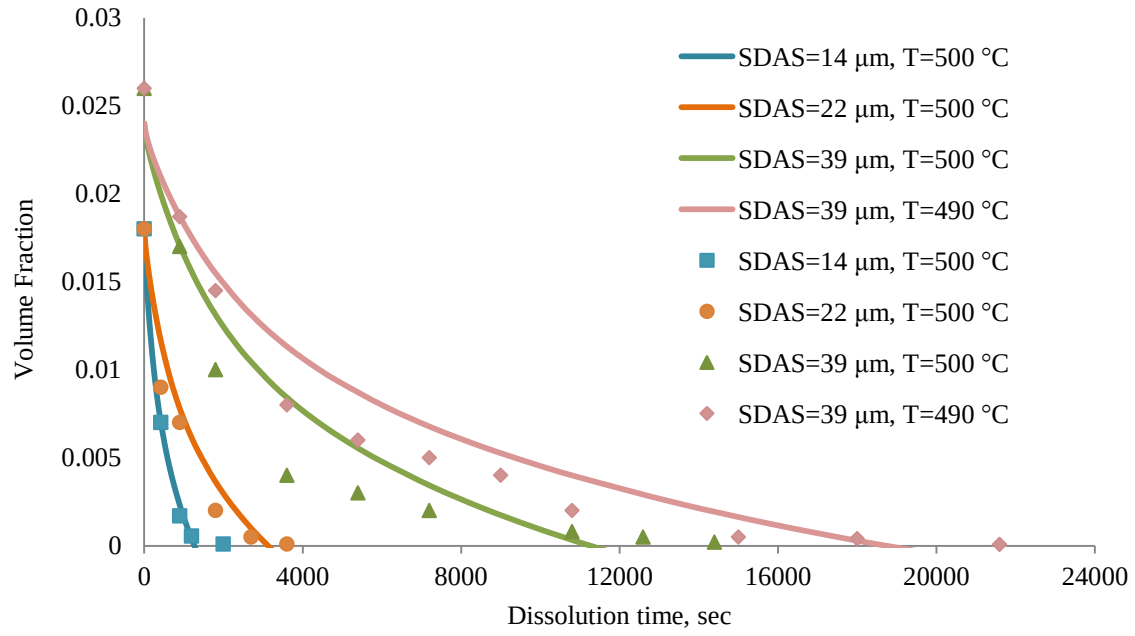

Figure 5.20: Experimental measurements (symbols) versus 3D COMSOL predictions (lines) for ellipsoid particle with aspect ratio of 5.

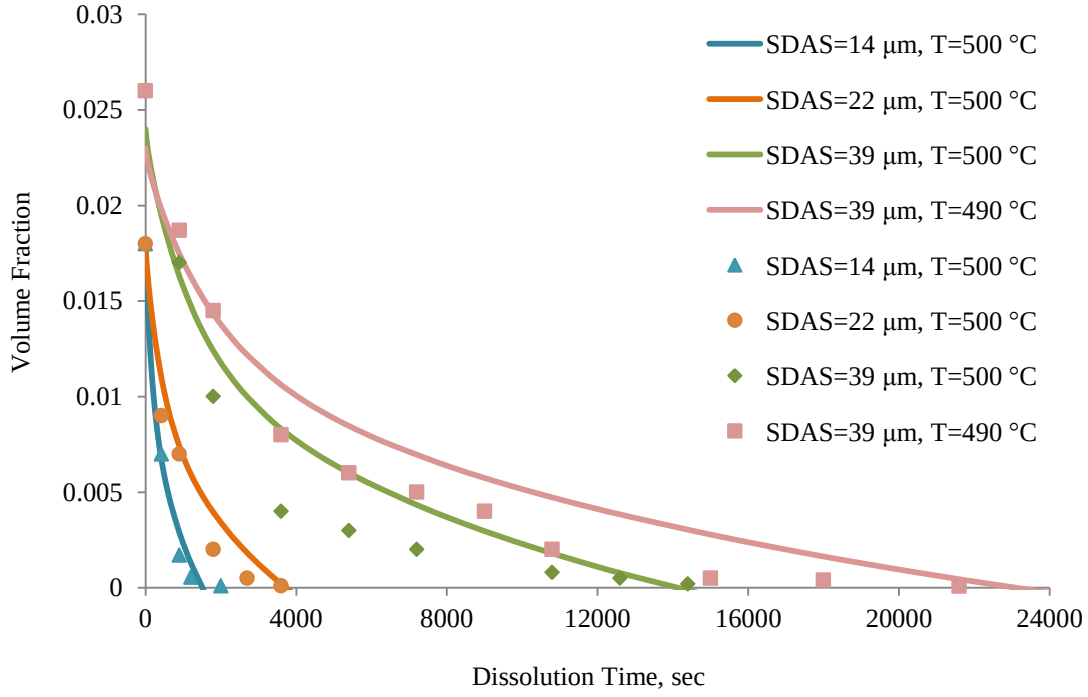

Figure 5.21: Experimental measurements (symbols) versus 3D COMSOL predictions (lines) for ellipsoid particle with aspect ratio of 7.

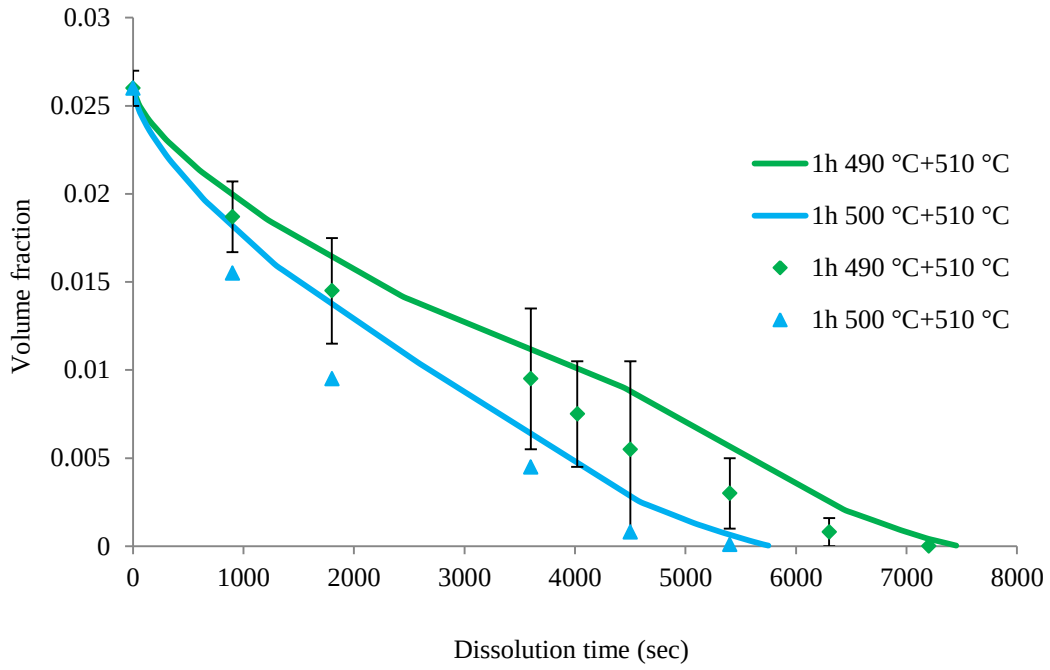

Figure 5.22: COMSOL predictions and experimental results in two step solution heat treatment.

Because of the inhomogeneous microstructure, there is large variation in the measurements for Al_2Cu volume fraction. At the initial stages of the dissolution the amount of error in the volume fraction is high, and it becomes smaller as the particles dissolve. The error bars are omitted from the graphs due to the complications they will cause in the figures.

5.2.7 Effect of particle morphology

To investigate the effect of particle shape on the dissolution time, the MCMM model as well as COMSOL software were used. Spherical, cylindrical and planer coordinates were modelled using MCMM; using COMSOL we were able to model elliptical morphology as well. It should be noted that the diffusion field size is not the same for different shapes, and it was calculated based on Equation 4.1.

MCMM prediction of volume fraction for SDAS of 22 µm and temperature of 500 °C for three shapes are shown in Figure 5.23. These results show that cylindrical and planer shapes have less dissolution times compared to the spherical shape which may be due to the higher surface to volume ratios that they have. The result for the dissolution time of a spherical particle

better fits the experimental results, which suggests that the simplification of using spherical morphology for modelling dissolution in this alloy system was valid.

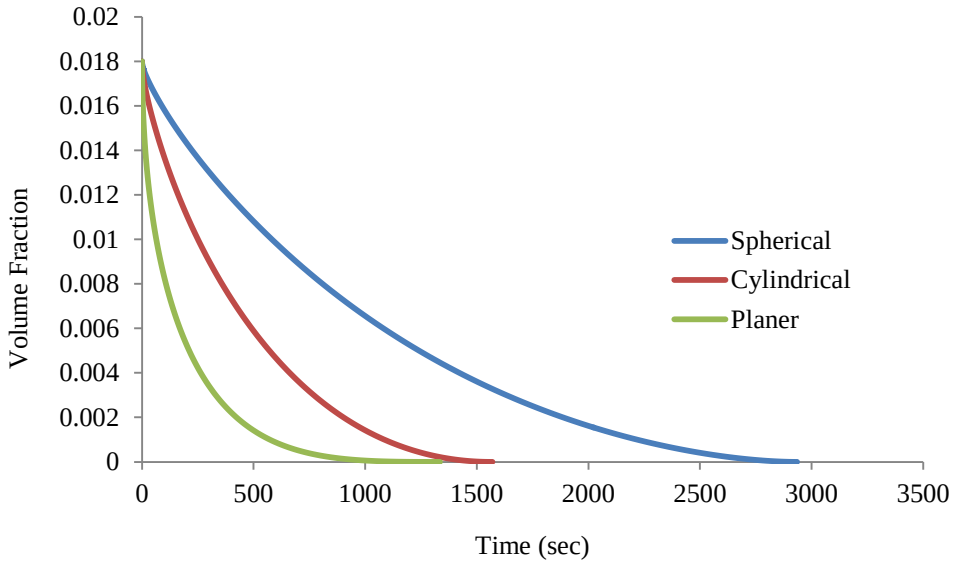

Figure 5.23: MCMM prediction of the effect of particle shape on the dissolution time.

COMSOL predictions of the dissolution of an elliptical particle with different aspect ratios for SDAS of 22 µ and temperature of 500 °C are shown in Figure 5.24. It can be seen that at the beginning of the dissolution process, increasing the aspect ratio decreases the dissolution time, which could be justified by the higher surface to volume ratio at higher aspect ratio, however, at longer dissolution times this trend changes and increasing aspect ratio, increases the dissolution time. This is due to the fact that there is another factor affecting the dissolution time in modelling, which is the uniformity of the diffusion of solutes. At high aspect ratios, diffusion is less uniform at two directions in comparison to the case in which the aspect ratio is low and the shape is close to a circle.

COMSOL prediction of the effect of morphology on the dissolution time is shown in Figure 5.25. Same trend as in MCMM model is seen with COMSOL. Dissolution time increases by going from planar to cylindrical and spherical to elliptical shape due to the decrease in surface to volume ratio from planar to spherical morphology. In the case of ellipse for the aspect ratio of 3 the predicted dissolution time is somewhat similar to the spherical particle. It could be due to

the competing effects of the increase of the surface to volume ratio and the diffusion non-uniformity in the field.

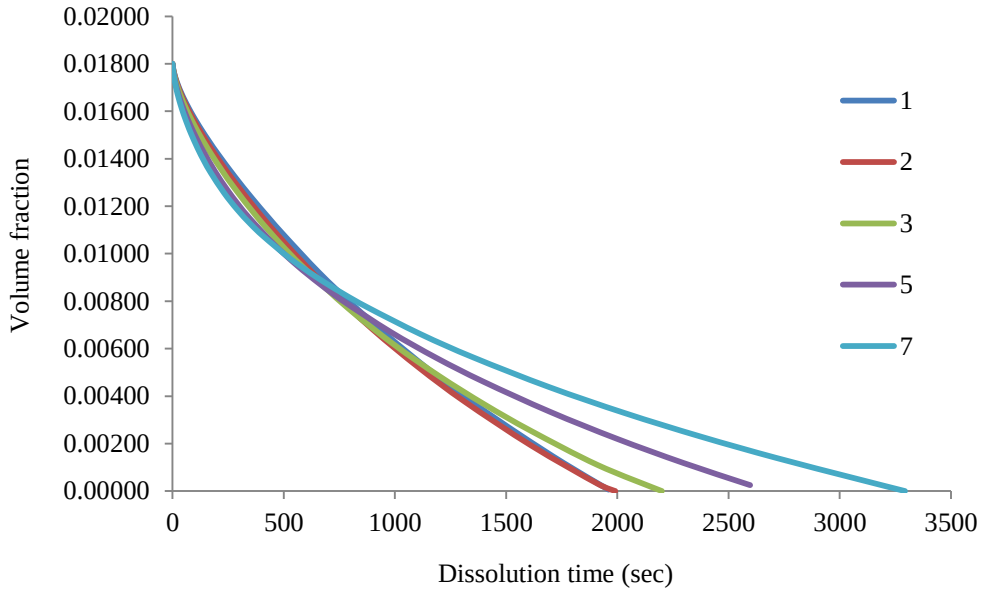

Figure 5.24: COMSOL predictions of the dissolution of an elliptical particle with different aspect ratios.

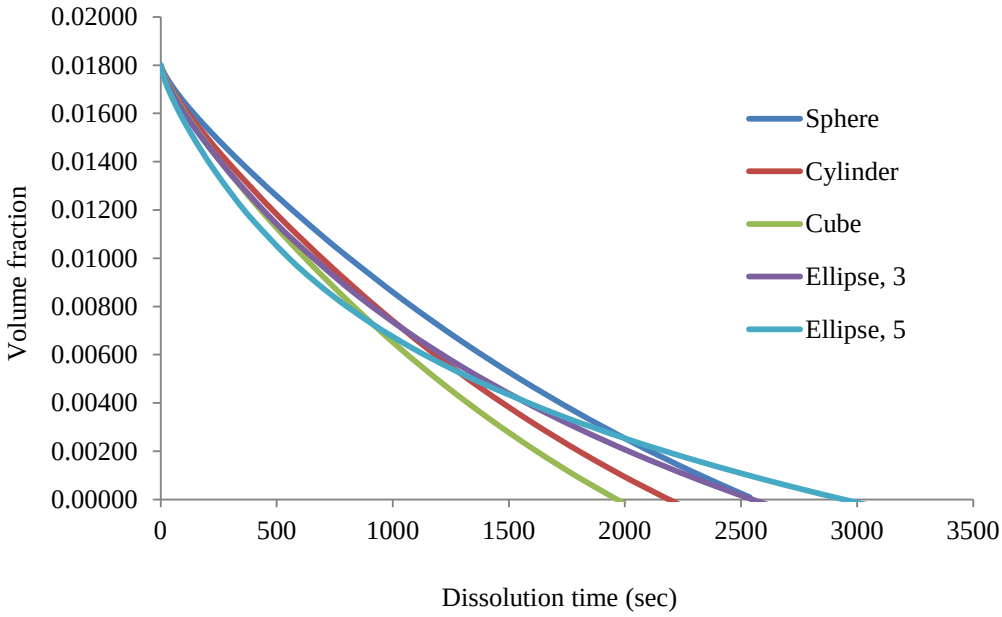

Figure 5.25: COMSOL predictions of the effect of particle shape on the dissolution time.

The COMSOL predictions of the Cu concentration gradient during the dissolution of spherical, planar and elliptical θ phase at different times for SDAS of 22 µm and temperature of 500 °C are shown in Figure 5.26, 5.27 and 5.28, respectively.

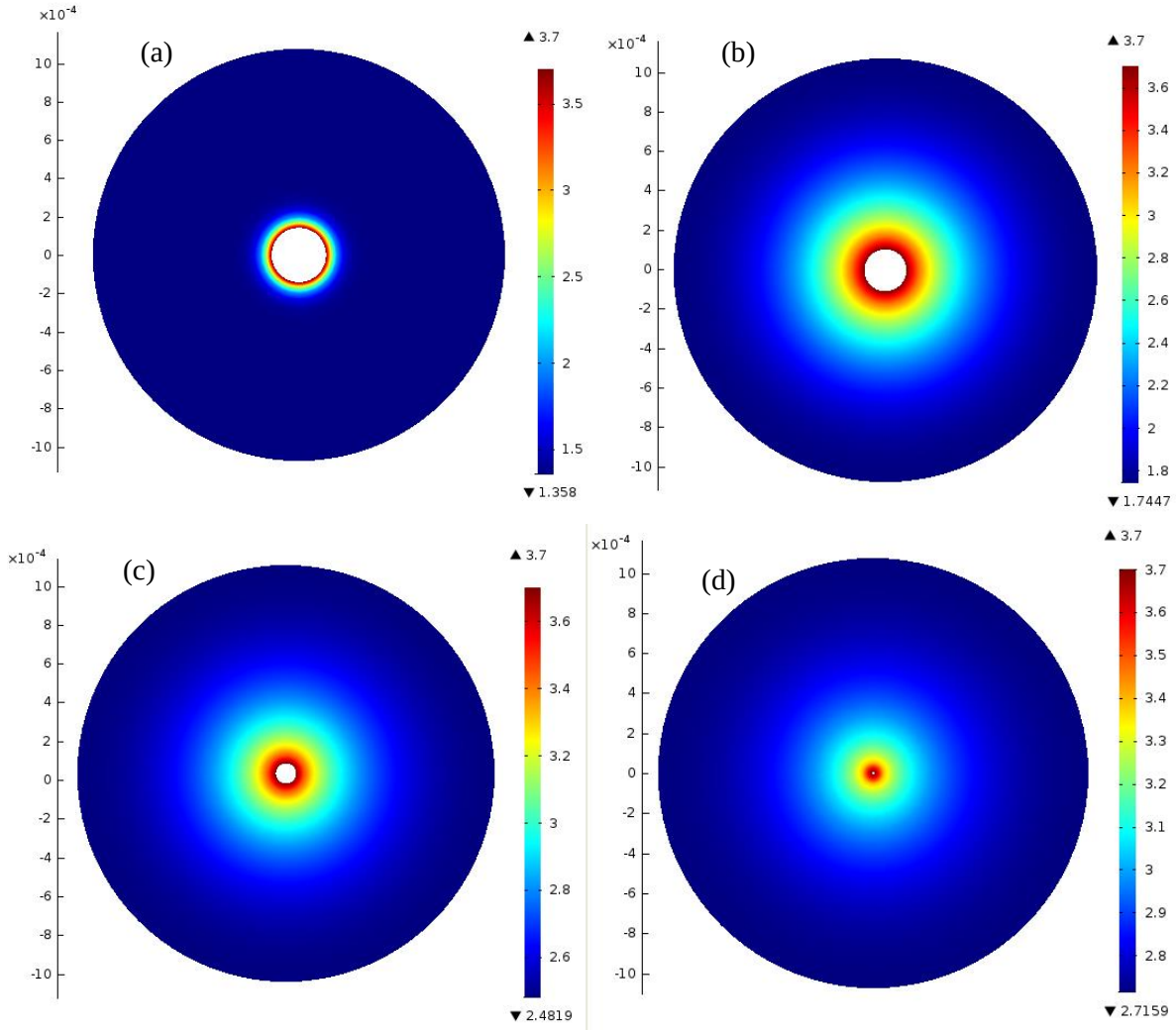

Figure 5.26: COMCOL prediction of the concentration Cu within the diffusion filed and radius of a spherical particle versus time for a 2D Circle (SDAS=22 µm, temperature= 500 °C) at (a) 0, (b) 500, (c) 1500 and (d) 2100 sec.

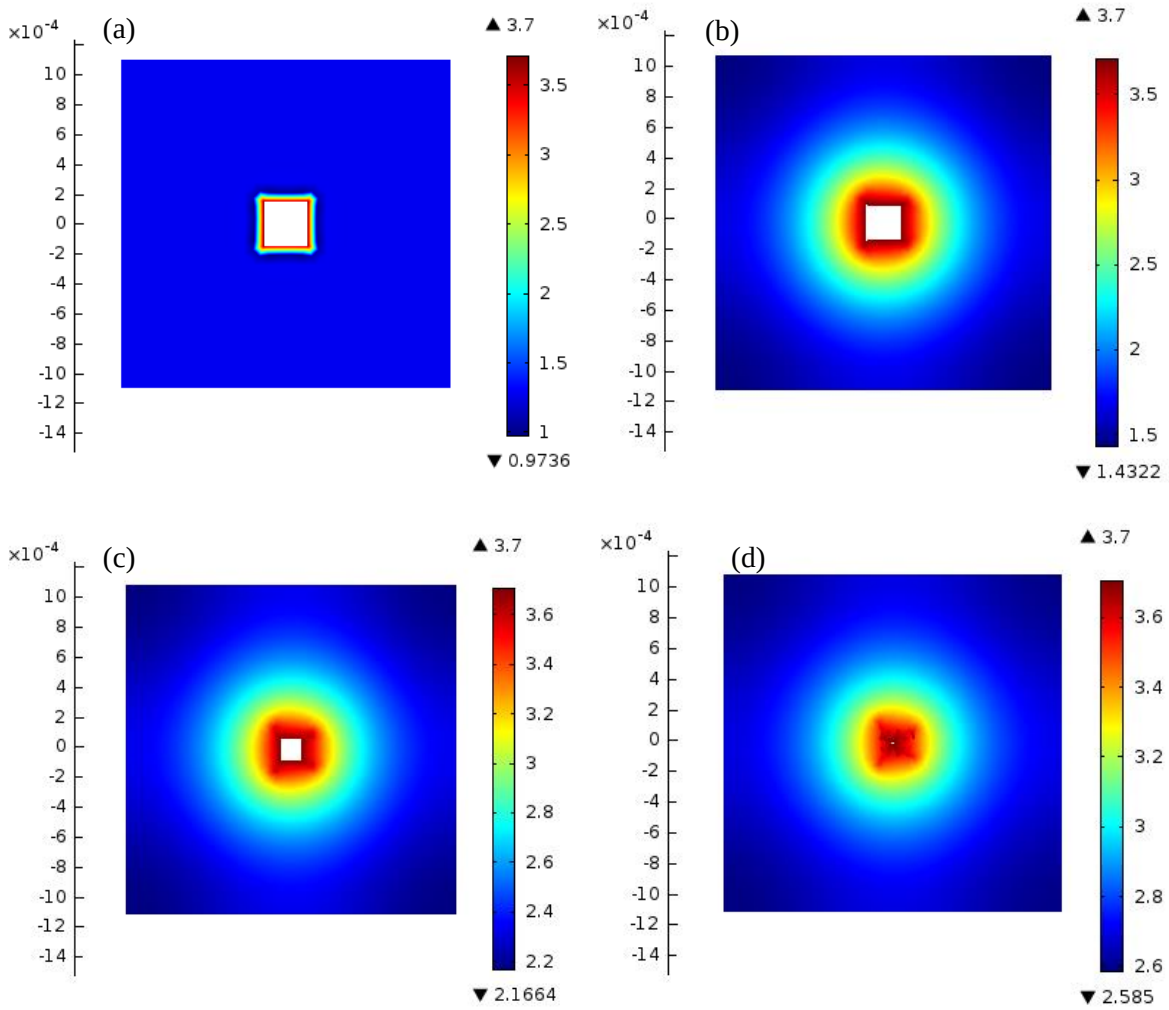

Figure 5.27: COMCOL prediction of the concentration of Cu within the diffusion field and radius of a planar particle versus time for a 2D Circle (SDAS=22 µm, temperature= 500 °C) at (a) 0, (b) 500, (c) 1500 and (d) 2100 sec.

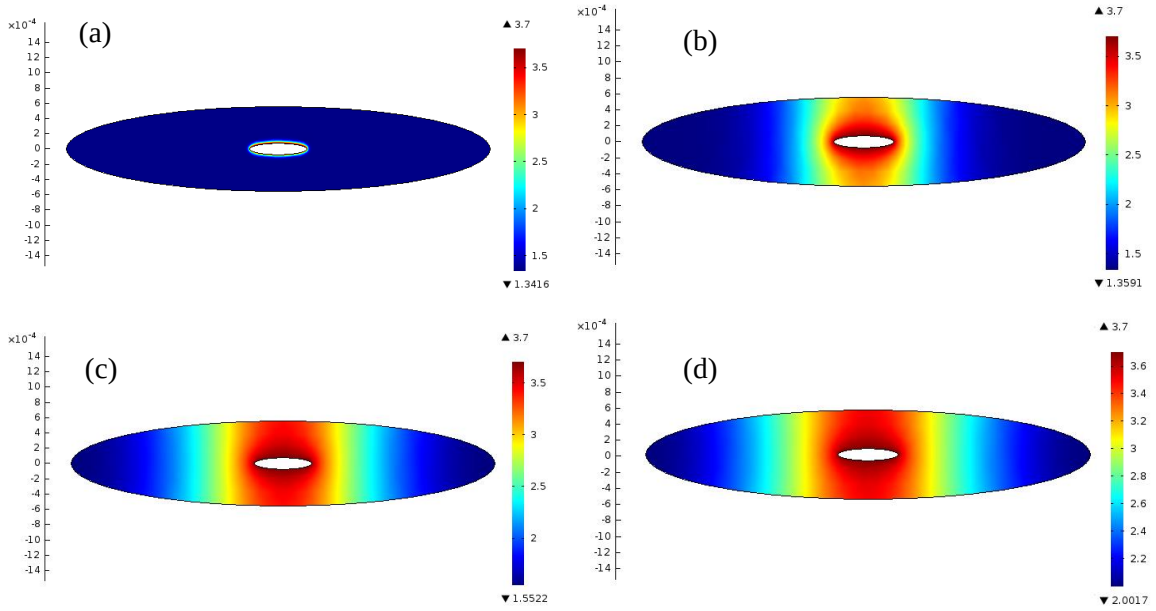

(c):t=1500 sec (d) :t=2100 sec

Figure 5.28: COMCOL prediction of the concentration of Cu within the diffusion field and radius of an elliptical particle versus time for a 2D Circle (SDAS=22 µm, temperature= 500 °C) at (a) 0, (b) 500, (c) 1500 and (d) 2100 sec.

5.2.8 Effect of the diffusion field size on the particle dissolution

The effect of the diffusion field size on the dissolution of a spherical and planar particle is seen in Figure 5.29 and 5.30, respectively. If the initial diffusion field radius is decreased, the dissolution time increases up to a peak which corresponds to the Cu solubility limit in the matrix. At still smaller diffusion field radius, the dissolution cannot be fully complete and the particles remain undissolved since the matrix becomes saturated of the solute. That the atoms from the alloying elements reach the diffusion field boundary after complete dissolution of the particle or not depends on the cell size and its geometry.

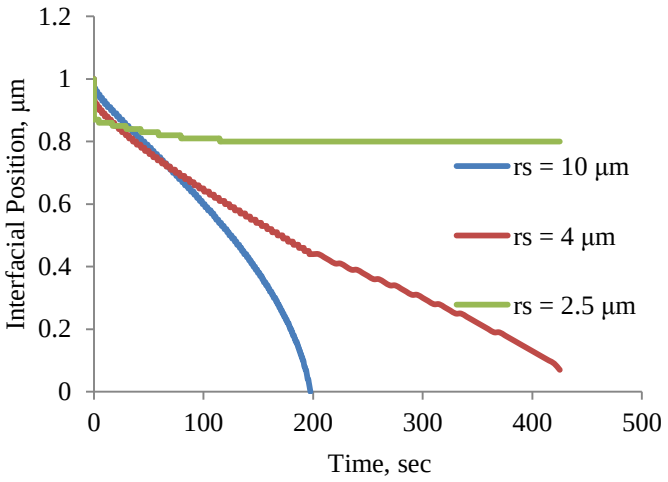

Figure 5.29: Dissolution time for a spherical particle at different diffusion field sizes.

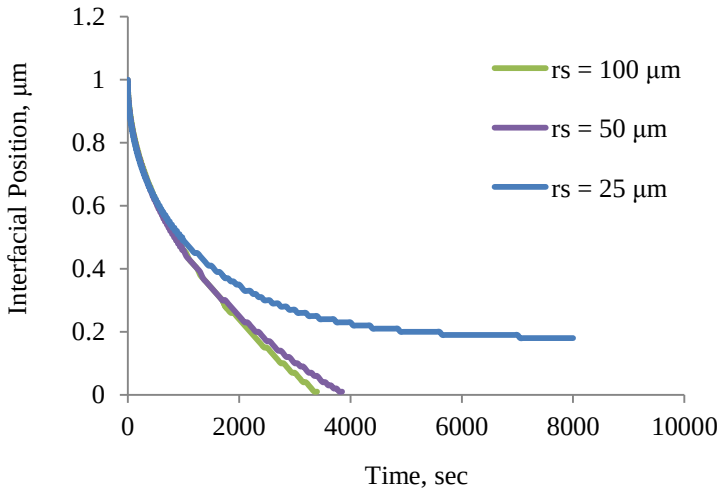

Figure 5.30: Dissolution time for a planar particle at different diffusion field sizes.

5.2.9 Homogenization

Now that the model has been validated, we can apply it to predict the homogenization time. The Homogenization time—that is the time needed for complete removal of concentration gradient within the dendrite and that the Cu concentration approaches the nominal Cu concentration of the alloy which is 2.8—versus SDAS is shown in Figure 5.31. It can be seen

that at smaller SDASs the difference between the dissolution time and homogenization time is short, however, as the SDAS increases the difference between the time needed for complete dissolution and homogenization increases. It is due to the fact that at smaller SDAS the diffusion field and so the diffusion distance is smaller and by the time the dissolution is achieved the homogenization is also completed, while at larger SDAS it takes longer for the solute to diffuse along the dendrite and so it takes longer for the complete homogenization to be achieved.

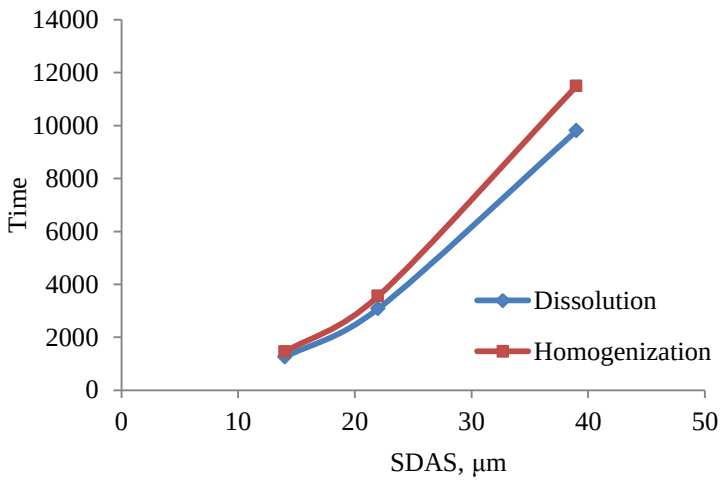

Figure 5.31: Dissolution and homogenization times for different SDASs at T = 500 °C.

The model prediction for concentration gradient between the centre and the edge of the dendrite is shown in Figure 5.32. The results show that the concentration at center of the dendrite is about 1%Cu less than the concentration of the edge at the initial stage of dissolution. At initial dissolution times, the concentration at the edge increases rapidly to 3.5 wt% Cu as particle is dissolving, which shows the dominant effect of dissolution over solute redistribution at the initial stages of the heat treatment. This causes an increase in the concentration difference between centre and edge. This difference between the dendrite centre and edge concentration then starts to decrease due to the homogenization that is also occurring during the solution heat treatment. When dissolution is complete, the concentration at the dendrite edge decreases rapidly to 3.1 wt%. The more obvious trend is that the overall Cu concentration within the dendrite increases as

the Al_2Cu particles are dissolving and changes from 0.5 wt% at the initial stages of solution heat treatment up to 2.8 wt% when dissolution is complete. After the dissolution it takes 3, 8 and 28 minutes for SDASs of 14, 22 and 39 μm, respectively, that the homogenization achieve and that the concentration reaches the nominal Cu concentration of the alloy. Such short dissolution and homogenization times suggest that the typical 8-hour industrial solution treatments are more likely to be dictated by ductility and toughness requirements. The latter are mainly affected by the spherodisation and coarsening of silicon, which were not modelled in this study.

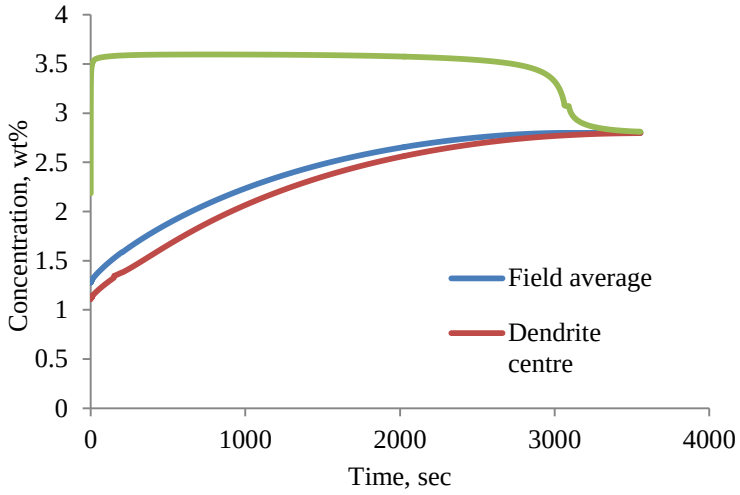

Figure 5.32: Concentration gradient along the diffusion field at T = 500 °C and for SDAS of 22 μm.

Chapter 6

6. Conclusions and Future work

6.1 Conclusions

Dissolution of secondary phases was modelled using MATLAB and COMSOL and the conclusion remarks are as follows:

- Using MATLAB, dissolution of a single or multi component particle was modelled in one dimension, while, COMSOL has the capability of modelling in two and three dimensions, and the ability to model complicated geometries such as planar, cylindrical and elliptical. However, we were not able to model dissolution of a multicomponent phase using COMSOL as it needs the use of a user defined function to solve the equation of the local mass conservation, which was not in the scope of this study.
- It was shown that numerical modelling can be a powerful tool for gaining an understanding of the solution treatment and homogenization behaviour of Al-Mg-Si-Cu alloys. The numerical models presented here highlight the relative sensitivities of the dissolution and homogenization times to SDAS and solution treatment temperature. Both the modelling and experimental results confirm that at 500 °C dissolution is more or less complete after 15 min, 45 min and 4 hr for SDAS of 14, 22 and 39 μm, respectively. Dissolution times are increased by increasing SDAS or decreasing solutionizing temperature as was expected. As image analysis revealed, the assumption made that the particles were spaced by a SDAS was true. Hence, variation of the model predictions from experimental results were indicative of the fact that particles do not have simple spherical geometry and their morphology is more close to ellipsoid with aspect ratio of 7. For the two-step solution heat treatment for SDAS of 39 μm, it was shown that solution

heat treatment of 1 hr 490 + 1 h 500 or 1 hr 490 °C + 30 min 510 °C can almost dissolves all the secondary particles. After the dissolution it takes 3, 8 and 28 minutes for SDASs of 14, 22 and 39 µm, respectively, for homogenization to achieve. Such short dissolution and homogenization times suggest that the typical 8-hour industrial solution treatments are more likely to be dictated by ductility and toughness requirements. The latter are mainly affected by the spherodisation and coarsening of silicon, which were not modelled in this study.

- The effect of the morphology of the dissolving particle was also studied. It was shown that going from planar to cylindrical to spherical and elliptical morphology, dissolution time increases due to the decrease in surface to volume ratio. For the case of elliptical morphology, it should be noted that there are two competing effect; one is the effect of surface to volume ratio, and the other is the effect of uniformity of the diffusion of solute. At the initial stages of the dissolution the effect of surface to volume ratio prevails, while at the longer times the effect of non-uniform diffusion due to having asymmetrical diffusion distance is predominant. Therefore, dissolution time increases compared to spherical morphology; dissolution time increases by increasing the aspect ratio of the ellipse.
- The numerical modelling of the Q phases showed that this phase cannot be fully dissolved at the studied temperatures for solution heat treatment, which were chosen by the particle incipient melting restrictions. Experimental studies for the Q phase volume fractions could not be obtained due to the very low volume fraction of the Q phase in the studied alloy, however, modelling results were in agreement with the ThermoCalc predictions.

6.2 Future work

- The modelling homogenization process can be validated using EPMA to find the solute concentration along the dendrite arm. EPMA can also be used to verify the solute concentration at the particle-matrix interface.
- Image analysis can be done to find the aspect ratio of the particle and the real shape of the particle.

- Three dimensional analysis can be done to validate the approximation of equalisation of area fraction to volume fraction.
- Experimental measurements could be done on a slightly different type of alloy with higher amount of Mg and therefore higher amount of the Q phase to validate the accuracy of the model in predicting concurrent dissolution of the θ and Q phases.
- Model sensitivity analysis to parameters such as diffusion coefficient, activation energy, solubility product and particle-matrix interface concentration can be done. It then should be concluded if interdiffusion of alloying elements can be neglected or not.
- A more complicated model can be developed to investigate the effect of interface interaction in addition to the diffusion as well as the effect of unequal particle sizes in the alloying system.
- A user defined function in COMSOL for application of local mass conservation at the interface could be developed. With this subroutine, the user can use COMSOL to predict dissolution time for multicomponent systems.

7. References

[1] G. E. Totten and D. S. MacKenzie, Handbook of Aluminum: Vol. 1, Physical Metallurgy and Processes, Ch. 1, 2003.

[2] ASM metals handbook, Vol 15, Ch. 1, 2008.

[3] I. J. Polmear: Light alloys, metallurgy of the light metals, 1980.

[4] L. Backerud, G. Chai and J. Tamminen, Solidification characteristics of aluminum alloys, Vol. 2: Foundry alloys, Des Plains, IL, AFS/Skanaluminium, 1990.

[5] L. Arnbert, L. Backerud and G. Chai, Solidification characteristics of aluminum alloys, Vol. 3: Dendritic coherency, Des Plains, IL, AFS, 1996

[6] A. Manente and G. Timelli, Recent Trends in Processing and Degradation of Aluminium Alloys, Ch. 9, 2011.

[7] R. Colas, A. Rodrı´guez, J. Talamantes and S. Valtierra, Solidification analysis of aluminium engine block, International Journal of Cast Metals Research Vol. 17 No. 6, pp. 332-338, 2004.

[8] M. Schneider and C. Heisser, Modeling of microstructure and mechanical properties of aluminum alloys during the casting and heat treatment process, AFS Proceedings, American foundary society, pp. 1-9, 2012.

[9] A. M. Samuel, P. Ouellet, F. H. Samuel and H. W Doty, Microstructural interpretation of thermal analysis of commercial 319 Al alloy with Mg and Sr additions, AFS Trans., Vol. 105, pp. 951-962, 1997.

[10] E. Tillová, M. Chalupová, L. Hurtalová, M. Bonek and L.A. Dobrzański, Structural analysis of heat treated automotive cast alloy, Vol 47, issue 1, 2011.

[11] F. H. Samuel, A.M. Samuel and H. W. Doty, "Factors controlling the type and morphology of Cu-containing phases in 319 Al alloy", *AFS Trans.*, Vol. 104, pp. 893-901, 1996.

[12] J. H. Sokolowski, M. B. Djurdjevic, C. A. Kierkus, D. O. Northwood, Improvement of 319 aluminum alloy casting durability by high temperature solution treatment, Journal of Materials Processing Technology, Vol. 109, pp. 174-180, 2001.

[13] E. Tillová, M. Chalupová and L. Hurtalová, Scanning electron microscopy, Ch. 21: Evolution of Phases in a Recycled Al-Si Cast Alloy During Solution Treatment, 2012.

[14] F. H. Samuel, A.M. Samuel and H. W. Doty, Factors controlling the type and morphology of Cu-containing phases in 319 Al alloy, AFS Transactions, Vol. 104, No. 9, pp. 893-901, 1996.

[15] O. Reiso, ,H. G. Øverlie and N. Ryum, Dissolution and melting of the secondary Al2Cu phase particles in an AlCu alloy, METALLURGICAL TRANSACTIONS A, Vol. 21A, pp. 1689-1695, 1990.

[16] I. Aguilera Luna, H. Mancha Molinar, M. J. Castro Roman, J. C. Escobedo Bocardo and M. Herrera Trejo, Improvement of the tensile properties of an Al–Si–Cu–Mg aluminum industrial alloy by using multi stage solution heat treatments, Materials Science & Engineering A, Vol. 561, pp. 1–6, 2013.

[17] G.Q. Wang, X.F. Bian and J. Y. Zhang, Gradual Solution Heat-Treatment of AlSiCuMg Cast Alloys, Rare Metals, Vol. 22, pp. 304-308, 2003.

[18] A.M.A. Mohamed and F.H. Samuel, Heat Treatment - Conventional and Novel Applications, Ch. 4:A Review on the Heat Treatment of Al-Si-Cu/Mg Casting Alloys, 2012.

[19] S. Shivkumar, S. Ricci, B. Steenhoff, D. Apelian and G. Sigworth, An Experimental Study to Optimize the Heat Treatment of A356 Alloy, AFS Transactions, Vol. 97, pp. 791-810, 1989.

[20] F. H. Samuel, "Incipient melting of $Al_5Mg_8Si_6Cu_2$ and Al_2Cu intermetallics in unmodified and strontium-modified Al-Si-Cu-Mg (319) alloys during solution heat treatment", Journal of Materials Science 33 (1998) 2283-2297.

[21] A.M.A. Mohamed, F.H. Samuel and S. Al kahtani, Influence of Mg and solution heat treatment on the occurrence of incipient melting in Al–Si–Cu–Mg cast alloys, Materials Science and Engineering A, Vol. 543, pp. 22– 34, 2012.

[22] F.H. Samuel, Incipient melting of Al5Mg8Si6Cu2 andAl2Cu intermetallics in unmodified and strontium-modified Al-Si-Cu-Mg (319) alloys during solution heat treatment, JOURNAL OF MATERIALS SCIENCE, Vol.33, pp. 2283-2297, 1998.

[23] W. Guo-hua, Z. Xiao-qin, L. Shao-guang, D. Wen-jiang and Z. Yan-ping, Effect of solution heat treatment on the microstructure and mechanical properties of Bb319 alloy in the lost foam casting process, Tsinghua Tongfang Knowledge Network Technology Co., Ltd.(Beijing), 2006.

[24] D. Ovono, I. Guillot and D. Massinon, The microstructure and precipitation kinetics of a cast aluminium alloy, Scripta Materialia, Vol. 55, pp. 259–262, 2006.

[25] Z. Li, A. M. Samuel and F. H. Samuel, Effect of alloying elements on the segregation and dissolution of $CuAl_2$ phase in Al-Si-Cu 319 alloys, Journal of Materials Science 38, pp. 1203-1218, 2003.

[26] Y. M. Han, A. M. Samuel, F. H. Samuel and H. W. Doty, Dissolution of Al_2Cu phase in non-modified and Sr-modified 319 type alloys, International journal of Cast Metals Research, Vol. 21, No. 5, pp. 387-393, 2008.

[27] Li, A.M. Samuel, F.H. Samuel, C. Ravindran, S. Valtierra and H.W. Doty, Factors Affecting Dissolution of Al2Cu Phase in 319 Alloys, AFS Transactions, Vol. III, pp. 03-100, pp.1-14,2003.

[28] Y. M. Han, A. M. Samuel, F. H. Samuel, S. Valtierra and H. W. Doty, Effect of solution heat treatment type on the dissolution of copper phases in Al-Si-Cu-Mg type alloys, AFS Trans, Vol 116, pp. 79-90, 2008.

[29] D. Apelian, S. Shivkumar, and G. Sigworth, Fundamental Aspects-of-Heat Treatment of Cast Al-Si-Mg Alloys,AFS Transactions, Vol. 97, pp. 727-742, 1989.

[30] Z. Li, A.M. Samuel, F. H. Samuel, C. Ravindran and S. Valtierra,Factors Affecting Dissolution of CuAl2 Phase in 319 Alloys, Transactions of the American Foundry Society and the One Hundred Seventh Annual Castings Congress, Milwaukee, WI; USA, pp. 26-29, 2003.

[31] Kh. A. Ragab, A.M. Samuel, A.M.A. Al-Ahmari, F.H. Samuel and H.W. Doty, Influence of fluidized sand bed heat treatment on the performance of Al–Si cast alloys, Materials and Design, Vol. 32, 1177–1193, 2011.

[32] S.K. Chaudhury and D. Apelian, Fluidized Bed Heat Treatment of Cast Al-Si-Cu-Mg Alloys, METALLURGICAL AND MATERIALS TRANSACTIONS A, Vol. 37A, pp. 2295-2311, 2006.

[33] G.Q. Wang, X. F. Bian and J. Y. Zhang, Gradual Solution Heat-Treatment of AlSiCuMg Cast Alloys, Rare Metals, Vol. 22, pp. 304-308, 2003.

[34] J. Gauthier, P.R. Louchez and F. H. Samuel, Heat Treatment of 319.2 Aluminum Automotive Alloy: Part 1, Solution Heat-Treatment, Cast Metals, Vol. 8, No.2, pp. 91-106, 1995.

[35] J. Gauthier and F. H. Samuel, Tensile Properties and Fracture Behavior of Solution Heat Treated 319.2 Aluminum Automotive Alloy, AFS Transactions, Vol. 103, pp. 849-858, 1995.

[36] H. de la Sablonnière and F. H. Samuel, Solution heat-treatment of 319 Aluminium Alloy Containing ~0.5wt% Mg Casting Alloys Part 1: Solidification and Tensile Properties, International Journal of Cast Metals Research, Vol. 9, pp. 195-211, 1996.

[37] H. de laSablonniere and F. H. Samuel, Effect of Mg content (~0.5 wt%) and solution heat treatment on the tensile properties of 319.1 aluminum alloy castings, Light Metals, pp. 235-245, 1996.

[38] S. N. Singh, B. P. Bardes and M. C. Flemings, Solution treatment of cast Al-4.5Cu alloy, METALLURGICAL TRANSACTIONS, Vol. 1, pp. 1383-1388, 1970.

[39] A.M. Samuel, H.W. Doty, S. Valtierra and F.H. Samuel, Defects related to incipient melting in Al-Si-Cu-Mg alloys, Materials and Design, Vol. 52, 947–956, 2013.

[40] S. Alkahtani, Mechanical performance of heat treated 319 alloys as a function of alloying and aging parameters, Materials and Design, Vol. 41, pp. 358-369, 2012.

[41] A. Wiengmoon, J.T. H. Pearce, T. Chairuangsri, S. Isoda, H.Saitoe and H. Kurata, HRTEM and HAADF-STEM of precipitates at peak ageing of cast A319 aluminium alloy, Micron, Vol. 45, 32–36, 2013.

[42] P. Apichai1, J. Kajornchiyakul, J.T.H. Pearce and A. Wiengmoon, Effect of Precipitation Hardening Temperatures and Times on Microstructure, Hardness and Tensile Properties of Cast Aluminium Alloy A319, vol. 143-144,pp. 306-310, 2003.

[43] H.K. Kang, M. Kida and H. Miyahara, Age hardening characteristics of Al-Si-Cu-Base cast alloys, AFS Trans, Vol. 107, 507-515, 1999.

[44] M. Abdulwahaba, I.A. Madugua, S.A. Yaroa, S.B. Hassana and A.P.I. Popoola, Effects of multiple-step thermal ageing treatment on the hardness characteristics of A356.0-type Al–Si–Mg alloy, Materials and Design, Vol. 32,pp. 1159–1166, 2011.

[45] E. Sjölander and S. Seifeddine, The heat treatment of Al–Si–Cu–Mg casting alloys, Journal of Materials Processing Technology, Vol.210, 1249–1259, 2010.

[46] H.B. Aaron, On the kinetics of precipitate dissolution, Metal science journal, Vol. 2, pp. 192-193, 1968.

[47] M. J. Whelan, On the kinetics of precipitate dissolution Metal Science Journal, Vol. 3, pp. 95-97, 1969.

[48] H. B. Aaron and G. R. Kotler, Second phase dissolution, Metallurgical transactions, Vol. 2, pp. 393-408, 1971.

[49] U. H. Tundal and N. Ryum, Dissolution of particles in binary alloys: Part 1: computer simulation, Metallurgical transactions A, Volume 23A, pp. 433-444, 1992.

[50] G. Thomas and M. J. Whelan, Observation of precipitation in thin foils of Aluminum +4% copper alloy, Philosophical Magazine, Vol. 6, 1103-1114, 1961.

[51] F. V. Nolfi, P. G. Shewmon, and J. S. Foster, The dissolution and growth kinetics of spherical precipitates, Transactions of the metallurgical society of AIME, Vol. 245, pp. 1427-1433, 1969.

[52] L. C. Brown, Diffusion-controlled dissolution of planar, cylindrical, and spherical precipitates, Journal of Applied Physics, Vol. 47, No. 2, 1976.

[53] V. V. Teleshov and V. S. Zolotorevsky, Tsvetnaya Met., Vol. 5, pp. 136-141, 1967.

[54] P.A. Rometsch, L. Arnberg and D. L. Zhang, Modelling dissolution of Mg_2Si and homogenisation in Al-Si-Mg alloys, International Journal of Cast Metals, Vol. 12, pp. 1-8, 1999.

[55] E. Javierre, C. Vuik, F.J. Vermolen and S. van der Zwaag, A comparison of numerical models for one-dimensional Stefan problems, Journal of Computational and Applied Mathematics, Vol. 192, pp 445–459, 2006.

[56] C. Vuik, A. Segal and F.J. Vermolen, A conserving discretization for a Stefan problem with an interface reaction at the free boundary, Computer Visual Science, Vol. 3, pp. 109–114, 2000.

[57] G. Segal, K.Vuik, and F. J. Vermolen, A Conserving Discretization for the Free Boundary in a Two-Dimensional Stefan Problem, JOURNAL OF COMPUTATIONAL PHYSICS, Vol. 141, pp. 1–21, 1998.

[58] E. Javierre, C. Vuik, F.J. Vermolen and A. Segal, A level set method for three dimensional vector Stefan problems: Dissolution of stoichiometric particles in multi-component alloys, Journal of Computational Physics, Vol. 224, pp. 222–240, 2007.

[59] F. Vermolen, K. Vuik and S. van der Zwaag, A mathematical model for the dissolution kinetics of Mg_2Si-phases in Al–Mg–Si alloys during homogenisation under industrial conditions, Materials Science and Engineering A, Vol. 254,pp.13–32, 1998.

[60] F.J. Vermolen and C. Vuik, A mathematical model for the dissolution of particles in multi-component alloys, Journal of Computational and Applied Mathematics, Vol. 126, pp. 233-254, 2000.

[61] F.J. Vermolen, C. Vuik and S. van der Zwaag, A mathematical model for the dissolution of stoichiometric particles in multi-component alloys, Materials Science and Engineering A, Vol. 328, pp. 14–25, 2002.

[62] F. J.Vermolen, K. Vuik and S. van der Zwaag, A numerical analysis for the dissolution of second phase particles in ternary alloys, Moving boundaries IV - Computational modelling of free and moving boundary problems, pp. 153-162, (1997).

[63] F. J.Vermolen, K. Vuik and S.van der Zwaag, The dissolution of a stoichiometric second phase in ternary alloys: a numerical analysis, Materials Science and Engineering A, Vol. 246, pp. 93–103, 1998.

[64] F. J.Vermolen and K.Vuik, A numerical method to compute the dissolution of second phases in ternary alloys, Journal of computational and applied mathematics, Vol. 93, pp. 123-143, 1998.

[65] F.J. Vermolen, P. Pinson, C. Vuik and S. van der Zwaag, A suite of sharp interface models for solid-state transformations in alloys, European Conference on Computational Fluid Dynamics ECCOMAS CFD, 2006.

[66] F.J. Vermolen, E. Javierre, C. Vuik, L. Zhao and S. van der Zwaag, A three-dimensional model for particle dissolution in binary alloys Computational Materials Science, Vol. 39, pp. 767–774, 2007.

[67] F.J. Vermolen, C. Vuik and S. van der Zwaag, Cross-diffusion controlled particle dissolution in metallic alloys, Comput Visual Sci, Vol. 8, pp. 27–33, 2005.

[68] F.J. Vermolen, C. Vuik and S. van der Zwaag, Particle dissolution and cross-diffusion in multi-component alloys, Materials Science and Engineering A, Vol. 347, 265-279, 2003.

[69] F. J. Vermolen and S. van der Zwaag, A numerical model for the dissolution of spherical particles in binary alloys under mixed mode control, Materials Science and Engineering A, Vol. 220, pp. 140-146, 1996.

[70] F. J. Vermolen, P. van Mourik and S. van der Zwaag, Analytical approach to particle dissolution in a finite medium, Materials Science and Technology, Vol. 13, 308-312, 1997.

[71] F. J. Vermolen, H. M. Slabbekoorn and S. van der Zwaag, The apparent activation energy for the dissolution of spherical Si-particles in AlSi-alloys, Materials Science and Engineering A, Vol. 231, pp 80-89, 1997.

[72] E. Sjölander and S. Seifeddine, Optimisation of solution treatment of cast Al–Si–Cu alloys, Materials and Design, Vol. 31, pp. 44–S49, 2010.

[73] E. Sjölander, Heat treatment of Al-Si-Cu-Mg casting alloys, P.hD. thesis, 2011.

[74] L. J. Colley, Microstructure-property models for T6 heat treatment of Al-Si-Mg alloys, P.hD. thesis, 2010.

[75] M. Mantina, Y. Wang, R. Arroyave, C. Wolverton, L. Q. Chen and Z. K. Liu, Phys Rev Lett., Vol. 100, 215901, 2008.

[76] N.A. Belov, D. G. Eskin and A.A. Aksenov, Multicomponent phase diagrams: applications for commercial aluminum alloys, Elsevier,1st edition, 2005.

[77] N.A. Belov, A.A. Aksenov and D. G. Eskin, Iron in Aluminium Alloys: Impurity and Alloying Element, Taylor and Francis 2002.

[78] L. Arnberg and B. Aurivillius, The Crystal Structure of $Al_xCu_2Mg_{12-x}Si_7$, (h-AlCuMgSi), Acta Chemica Scandinavica A, Vol. 34, pp. 1-5, 1980.

[79] S. Seifeddine, E. Sjölander and T. Bogdanoff, On the Role of Copper and Cooling Rates on the Microstructure, Defect Formations and Mechanical Properties of Al-Si-Mg Alloys, Materials Sciences and Applications, Vol. 4, pp. 171-178, 2013.

[80] S. P. Nikanorov, M. P. Volkov, V.N. Gurin, Yu. A. Burenkov, L. I. Derkachenka, B.K. Kardashev, L. L. Regel and W.R. Wilcox, Structural and mechanical properties of Al–Si alloys obtained by fast cooling of a levitated melt, Materials Science and Engineering A, Vol. 390, pp. 63-69, 2005.

[81] M. Gupta and S. Ling, Microstructure and mechanical properties of hypo/hypereutectic Al–Si alloys synthesized using a near-net shape forming technique, Journal of Alloys and Compounds, Vol. 287, pp. 284-294, 1999.

[82] J. Zhang, Y. N. Huang, C. Mao nad P. Peng, Structural, elastic and electronic properties of y (Al_2Cu) and S(Al_2CuMg) strengthening precipitates in Al–Cu–Mg series alloys: First-principles calculations, Solid State Communications, Vol. 152, pp. 2100–2104, 2012.

[83] M. Voncina, J. Medved, T. Boncina and F. Zupanic, Effect of Ce on morphology of α(Al)−Al2Cu eutectic in Al−Si−Cu alloy, Trans. Nonferrous Met.Soc. China, Vol. 24, pp. 36−41, 2014.

[84] X. M. Pan, C. Lin, J. E. Morral and H.D. Brody, An Assessment of Thermodynamic Data for the Liquid Phase in the Al-Rich Corner of the Al-Cu-Si System and Its Application to the Solidification of a 319 Alloy, Journal of Phase Equilibria and Diffusion, Vol. 26, No. 3, 2005.

[85] C. Wolverton, Crystal structure and stability of complex precipitate phases in Al-Cu-Mg-(Si) and Al-Zn-Mg alloys, Acta Materialia, Vol. 49, pp. 3129–3142, 2001.

[86] C. Ravi, C. Wolverton, First-principles study of crystal structure and stability of Al–Mg–Si–(Cu) precipitates, Acta Materialia, Vol. 52, 4213–4227, 2004.

[87] H. Fredriksson, U. Åkerlind, Solidification and Crystallization Processing in Metals and Alloys, Wiley, 2012.

[88] L. Liu, A.M.A. Mohamed, A.M. Samuel, F.H. Samuel, H.W. Doty, and S. Valtierra, Precipitation of β-Al5FeSi Phase Platelets in Al-Si Based Casting Alloys, METALLURGICAL AND MATERIALS TRANSACTIONS A, Vol. 40A, pp. 2457-2469, 2009.

[89] R. I. Mackay, J. H. Sokolowski, Effect of Si and Cu concentrations and solidification rate on soundness in casting structure in Al–Si–Cu alloys, International Journal of Cast Metals Research, Vol. 23 No. 1, pp. 7-22, 2010.

[90] N. C. W. Kuijpers, F. J. Vermolen, K. Vuik, S. van der Zwaag, A Model of the β-AlFeSi to α-Al(FeMn)Si Transformation During Homogenization in 6xxx Alloys, Materials Transactions, Vol. 44, No. 7, pp. 1448-1456, 2003.

Appendices

A: Numerical discretization

Stationary interface

Discretization of the equations 4.8 and 4.9 is as follows:

$$m_{in} = D\frac{(c_{i-1} - c_i)\rho}{dr} 4\pi {r_{i-1}}^2 t$$

$$m_{out} = D\frac{(c_i - c_{i+1})\rho}{dr} 4\pi {r_i}^2 t$$

And the solute concentration added to each shell after each time step can be obtained as follow;

$$c_i = \frac{mass\ added\ to\ shell}{volume\ of\ the\ shell} = \frac{\left(m_{in}^i - m_{out}^i\right)/\rho}{4\pi/3\,(r_i^3 - r_{i-1}^3)} \qquad (A.1)$$

Concentration after each time step can then be calculated as follow;

$$c_i^{t+1} = c_i^t + c_i$$

$$c_i^{t+1} = c_i^t + 3\frac{r_{i-1}^2(c_{i-1} - c_i) - {r_i}^2(c_i - c_{i+1})}{(r_i^3 - r_{i-1}^3)} \qquad (A.2)$$

Moving boundary

Discretization of the interior region

An implicit finite difference method is used to solve the diffusion equation. Since the magnitude of the gradient is maximal near the moving interface we use a geometrically distributed grid such that the discretization near the interface is fine and coarse farther away from the moving interface. Furthermore, a virtual grid-point near the moving boundary is used. The distance between the virtual node and the interface is chosen equal to the distance between the interface and the first grid-node.

Discrete boundary conditions at the interface

The discrete approximation of the concentration is defined as$c_{i,k}^{j}$, where j, i and k respectivelydenote the time-step, the index of the chemical (alloying) element and grid-node. The virtual grid-node behind the moving interface and the grid-node at the interface respectively have indices k = -1 and k = 0. At the moving interface, it is obtained from discretization of Equation (4.21)

$$\frac{D_{Cu}}{c_{Cu}^{p}-c_{Cu}^{sol}}\frac{c_{Cu,1}^{j+1}-c_{Cu,-1}^{j+1}}{2\Delta r}=\frac{D_{Si}}{c_{Si}^{p}-c_{Si}^{sol}}\frac{c_{Si,1}^{j+1}-c_{Si,-1}^{j+1}}{2\Delta r}$$

$$\frac{D_{Cu}}{c_{Cu}^{p}-c_{Cu}^{sol}}\frac{c_{Cu,1}^{j+1}-c_{Cu,-1}^{j+1}}{2\Delta r}=\frac{D_{Mg}}{c_{Mg}^{p}-c_{Mg}^{sol}}\frac{c_{Mg,1}^{j+1}-c_{Mg,-1}^{j+1}}{2\Delta r}$$

The concentration profile of each element is determined by the value of the interfacial concentration. Above equations can be re-arranged into a zero-point equations for all chemical elements. All interfacial concentrations satisfy the hyperbolic equation (4.13). Combination of all equations give:

$$D_{Cu}\left(c_{Cu,1}^{j+1}-c_{Cu,-1}^{j+1}\right)\left(c_{Si}^{p}-c_{Si}^{sol}\right)-D_{Si}\left(c_{Si,1}^{j+1}-c_{Si,-1}^{j+1}\right)\left(c_{Cu}^{p}-c_{Cu}^{sol}\right)=0$$

$$D_{Cu}\left(c_{Cu,1}^{j+1}-c_{Cu,-1}^{j+1}\right)\left(c_{Mg}^{p}-c_{Mg}^{sol}\right)-D_{Si}\left(c_{Mg,1}^{j+1}-c_{Mg,-1}^{j+1}\right)\left(c_{Cu}^{p}-c_{Cu}^{sol}\right)=0$$

$$\left(c_1^{sol}\right)^{m_1}\left(c_2^{sol}\right)^{m_n}(\ldots)(c_n^{sol})^{m_n} - K_{sol} = 0$$

Diffusion equation needs to be solved for every component in the system. In the case of a moving boundary we do not know the value of c_i^{sol}. We need equations (4.13) and (4.17) to determine this value. Because this is a nonlinear problem we proceed as follows.

1. Take a good first guess for$c_{i,sol}^{j+1}$.
2. Using the current estimate for $c_{i,sol}^{j+1}$and R_k^{j+1}, and the c_i^j and R_k^j from the previous time step, we can calculate the new concentration profiles of each component, as well as the concentration gradient at the boundaries.
3. Now we have enough information to do a Newton-Raphson step to obtain a better approximation for $c_{i,sol}^{j+1}$.
4. Continue with step 1 until the desired accuracy is reached.

B: Phase diagram of the B319 alloy

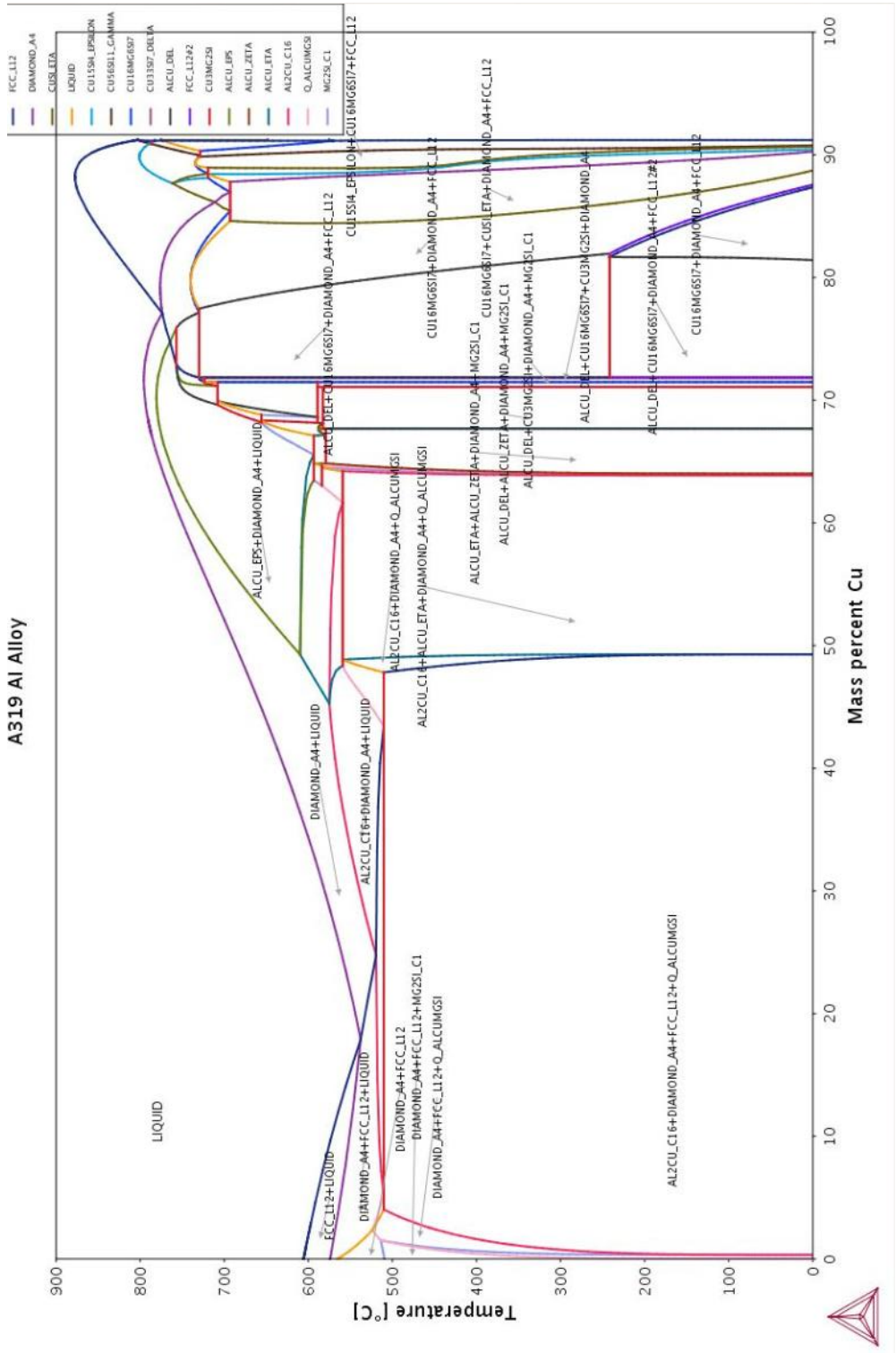

Figure B.1: Thermocalc predictions for AlB319 phase diagram.

C: FactSage result

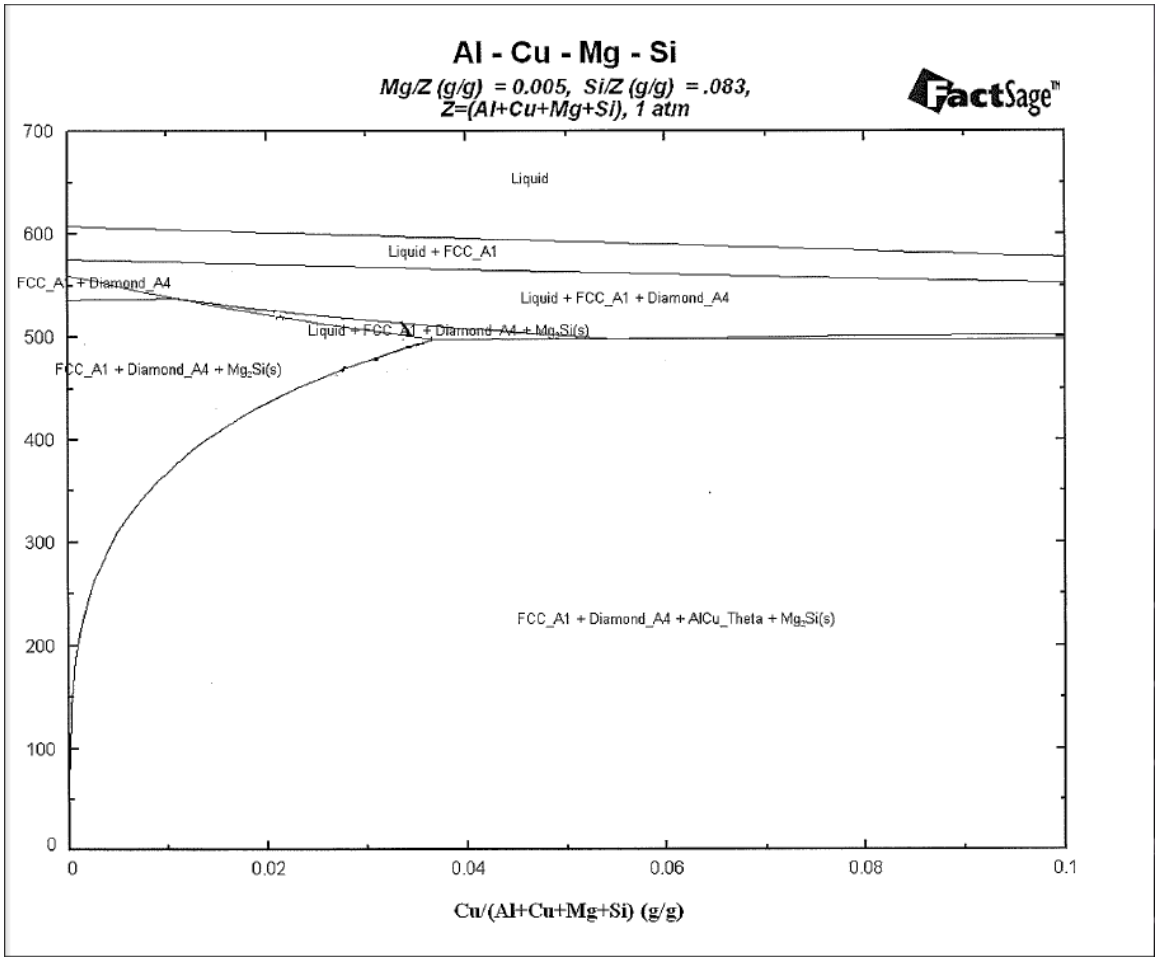

Figure C.1: FactSage prediction for phase diagram of AlB319.

D: Analytical validation of the model via Vermolen model

The model predictions were validated using Vermolen results [61].

Table D.1: Input data.

Physical quantity	Value	SI-unit
D_1	10^{-13}	$m^2\ s^{-1}$
D_2	2×10^{-13}	$m^2\ s^{-1}$
K	1	–
c_1^{part}	33	–
c_2^{part}	33	–
c_1^0	0	–
c_2^0	0	–
c_3^0	0	–
m_1	1	–
m_2	2	–
S_0	10^{-6}	M
M	10^{-4}	M

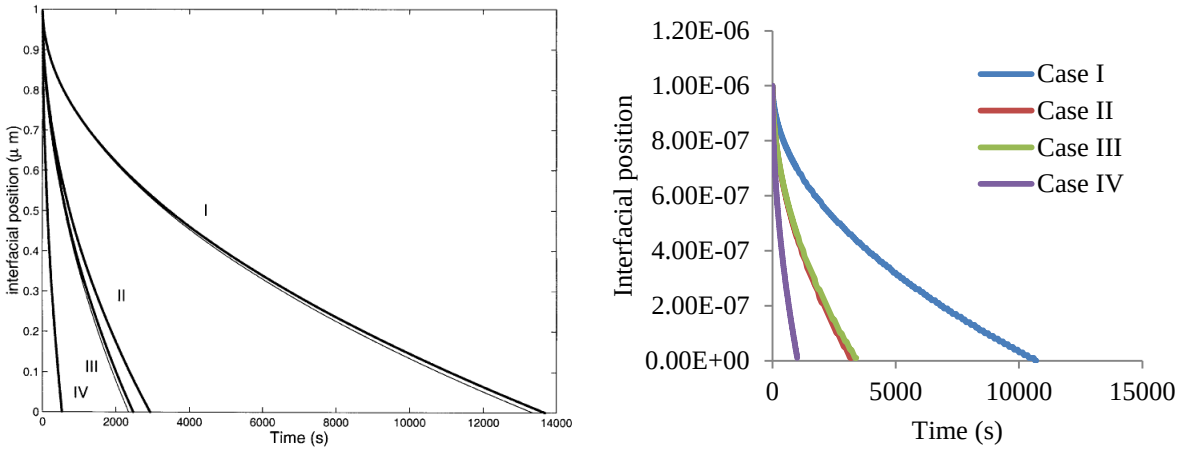

Figure D.1: The interfacial position as a function of time for a planar dissolving particle; a) Vermolen model and b) model of this study.

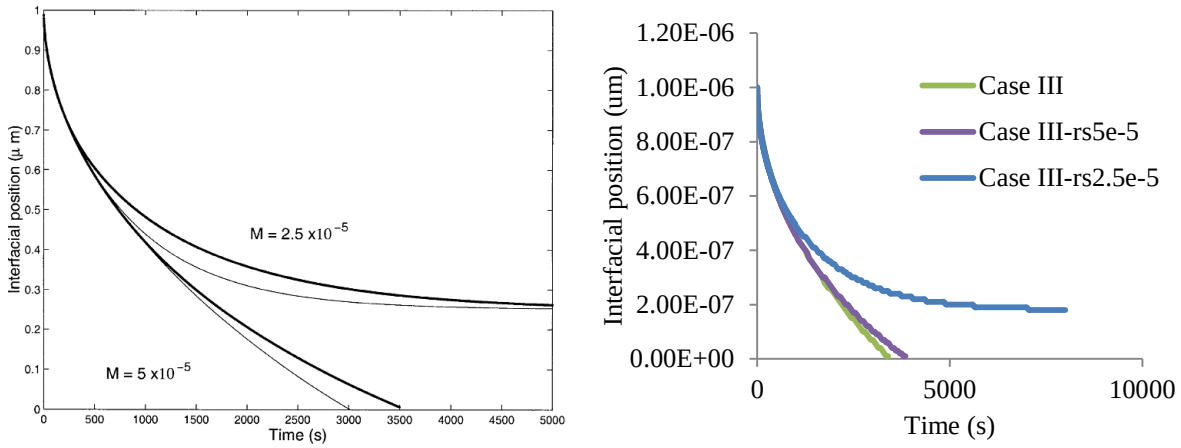

Figure D.2: The interfacial position as a function of time for a planar dissolving particle; a) Vermolen model and b) model of this study.

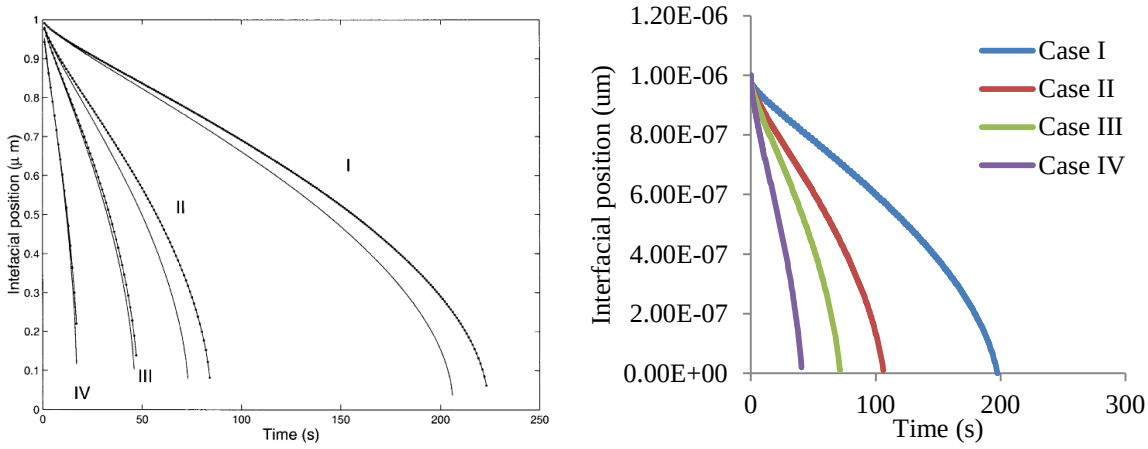

Figure D.3: The interfacial position as a function of time for a spherical dissolving particle; a) Vermolen model and b) model of this study.

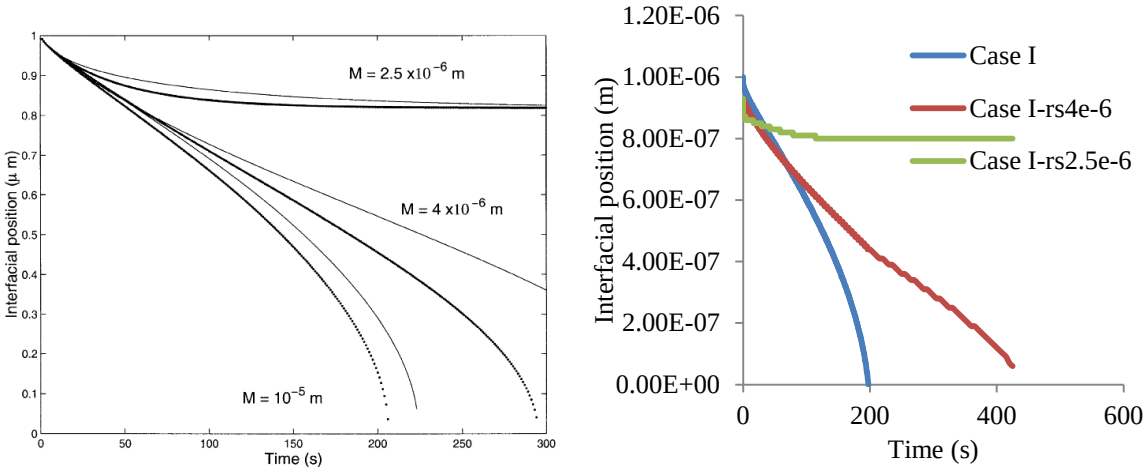

Figure D.4: The interfacial posision as a function of time for a spherical dissolving particle; a) Vermolen model and b) model of this study.